Structure-Processing-Property Interrelationships of Vapor Grown Carbon Nanofiber, Single-Walled Carbon Nanotube and Functionalized Single-Walled Carbon Nanotube – Polypropylene Nanocomposites

by

Vinod Karumathil Radhakrishnan

A dissertation submitted to the Graduate Faculty of
Auburn University
in partial fulfillment of the
requirements for the degree of
Doctor of Philosophy

Auburn, Alabama
December 13, 2010

Approved by

Virginia Davis, Chair, Associate Professor of Chemical Engineering
Ram Gupta, Distinguished Professor of Chemical Engineering
Mark Byrne, Associate Professor of Chemical Engineering
Satish Kumar, Professor of Polymer, Textile, and Fiber Engineering

Abstract

This dissertation describes the first use of a design of experiments approach to investigate the interrelationships between structure, processing, and properties of melt extruded polypropylene (PP) carbon nanomaterial composites. The effect of nanomaterial structure was evaluated by exploring the incorporation of vapor grown carbon nanofibers (VGCFs), or pristine or functionalized single-walled carbon nanotubes (SWNTs or C12SWNTs) in polypropylene, while the effect of processing was investigated by studying the influence of melt extrusion temperature, speed, and time. The nanomaterials and PP were combined by an initial mixing method prior to melt extrusion. The nanocomposite properties were characterized by a combination of morphological, rheological, and thermal methods. Preliminary investigations into the effects of the initial mixing method revealed that the distribution of nanomaterials obtained after the mixing had a considerable influence on the properties of the final melt extruded nanocomposite. Dry mixing (DM) resulted in minimal adhesion between nanomaterials and PP during initial mixing; the majority of nanomaterials descended to the bottom. Hot coagulation (HC) mixing resulted in extremely high degrees of interaction between the nanomaterials and PP chains. Rotary evaporation (RE) mixing resulted in nanomaterial distribution uniformity between that obtained from DM and HC. Employing design of experiments to investigate the effects of structure and processing conditions on melt extruded PP nanocomposite properties revealed several interesting

effects. The effect of processing conditions varied depending on the degree of nanomaterial distribution in PP attained prior to melt processing. Increasing melt extrusion temperature increased the decomposition temperature (T_d) of PP/C12SWNT obtained from HC mixing but decreased T_d of PP/C12SWNT obtained from RE mixing. Higher melt extrusion screw speed, on the other hand, significantly improved the nanocomposite crystallization behavior in RE nanocomposites, while not being a major processing factor in HC nanocomposites. The variations in nanocomposite properties with processing conditions were the result of complex interactions between the degree of dispersion, polymer degradation, and stability of the nanocomposite microstructure effected by the nanomaterial structure and processing conditions. Most importantly, this investigation revealed that the optimum melt processing conditions to be employed varied depending on the materials being used and the property of interest.

Acknowledgements

First and foremost, I would like to thank my advisor, Dr. Virginia Davis. She was a constant source of encouragement and her constructive criticism always helped in the progress of this research. Our time spent setting up our research laboratory will forever be cherished.

I am thankful to my committee members Dr. Ram Gupta, Dr. Mark Byrne, and Dr. Satish Kumar, for their support and suggestions. I am also thankful to Dr. Maria Auad for agreeing to take on the role of the university reader, and for her many suggestions and cooperation in sharing her research equipment. I am grateful to Dr. Edward Davis for all his advice regarding thermal analyses and design of experiments.

Many thanks to Matthew Kayatin, Dhriti Nepal, Shanthi Murali, Amogh Karwa, Ben Marshall, Ao Geyou, Teng Xu, Daniel Horn, and many others for all their help and the good times in lab. I would like to thank Ricky Bates, Brian Downs, and Drew Ainscough for all their assistance in this research. I would also like to thank Stephen Howard for his help in accessing some of the equipment crucial for this research.

I am extremely grateful for the constant support and encouragement from my mother and brothers, Manoj and Sunoj. They are the best family I could ask for, and everything I am I owe it to them. Last, but not the least, I would like to thank Shalley (JA/DA) for being an amazing friend who was always there when I needed one the most.

Table of contents

List of Figures

List of Tables

Chapter 1

Introduction

Polymer nanocomposites incorporate the highly desirable mechanical, thermal, or electrical properties of nanomaterials into polymers. They are often fabricated by melt processing nanomaterials with a thermoplastic polymer. The objective of this research was to gain a better understanding of the interrelationships between carbon nanomaterial chemistry, processing conditions, and the properties of the final melt extruded polypropylene (PP) nanocomposites. In particular, the combined effects of the type of nanomaterial incorporated and the melt processing conditions employed on the morphological, rheological, and thermal behavior of the nanocomposite were investigated.

The motivation for this research arises from the fact that, while structure and processing have separate and individual influences on nanocomposite properties, the combined influence of the two is also extremely important. Significant research has focused on either the effects of processing conditions or the effects of chemical modification of the polymer or nanomaterial on nanocomposite properties. However, the results have largely been inconsistent. Due to a lack of a direct comprehensive comparison, it is uncertain if this inconsistency is due to chemical incompatibility between the polymer and nanomaterial, or the processing conditions employed, or a combination of both. Achieving desirable properties in polymer nanocomposites at low

nanotube loadings requires that the nanomaterials be uniformly dispersed as individuals or small bundles. In addition, achieving load transfer requires strong interfacial interactions between the nanomaterials and the surrounding polymer matrix. However, achieving dispersion and interfacial interactions are inhibited by the strong van der Waals attraction between the nanomaterials. This is especially true in the case of single-walled carbon nanotube (SWNT) nanocomposites.

The nanomaterials explored in this research were vapor grown carbon nanofibers (VGCFs), SWNTs, and $C_{12}H_{25}$ functionalized SWNTs (C12SWNTs). Several initial mixing methods, to incorporate the nanomaterials and PP prior to melt extrusion, were evaluated and found to have a significant influence on the resulting nanocomposite properties. Dry mixing (DM), the most commonly used method to combine thermoplastic polymers and nanomaterials prior to melt extrusion, was extremely inefficient in uniformly distributing the nanomaterial through bulk PP. A large fraction of the nanomaterials tended to settle to the bottom, with very little adhering to the polymer surface. Hot coagulation mixing (HC), a significantly more complex procedure, enabled extremely uniform nanomaterial distribution throughout the bulk PP. Rotary evaporator mixing (RE), a comparatively simpler method, achieved a degree of nanomaterial distribution that was better than that obtained in DM but not as superior as in HC. The nanomaterials were observed to completely coat the surface of the polymer in RE. The degree of nanomaterial distribution obtained from the initial mixing methods tended to dictate the nanomaterial dispersion in the final melt extruded nanocomposites.

A design of experiments approach was employed to simultaneously explore and understand the effects of nanomaterial structure (VGCF, SWNT, or C12SWNT) and melt

extrusion processing conditions (extrusion temperature, speed, and time) on the properties of PP nanocomposites. Varying the melt processing conditions did not have any significant effect on the resulting properties of DM nanocomposites due to the fact that the nanomaterials were poorly distributed as large aggregates in the initial mixture. Although melt mixing did improve dispersion, the low shear of the Haake Minilab's converging screws was insufficient to break these aggregates. Melt processing, however, did have a very significant influence on nanocomposite properties in cases where the nanomaterials were evenly distributed through the bulk polymer during initial mixing prior to feeding into the extruder. Melt processing conditions influenced nanocomposite properties by either resulting in the formation of interconnected nanomaterial networks in the polymer, or by completely breaking down any nanomaterial network and degrading the polymer. In addition, depending on the nanomaterial distribution achieved prior to melt extrusion, processing conditions had vastly different effects. Melt extrusion temperature and speed had no effect on nanocomposite crystallization behavior in HC nanocomposites. However, these factors had a very significant effect on the crystallization of RE nanocomposites. Similar variability in the effects of processing factors was observed with other response variables, such as decomposition and melt temperature. The effect of melt processing conditions also depended on the chemistry of the nanomaterial involved. With potentially friable materials, like VGCF, high shear tended to result in breakage of individual fibers, whereas with SWNTs, high shear tended to lead towards better dispersion. Most importantly, this research revealed that the optimum processing conditions to be employed varied depending on the materials being used and the property of interest.

This dissertation is organized in the following manner. Chapter 2 provides background information on VGCF, SWNT, polymer nanocomposites, nanomaterial dispersion, nanomaterial functionalization, interfacial interaction, and nanocomposite characterization. Chapter 3 provides information on materials used, experimental techniques, and sample characterization. Chapter 4 discusses the effect of initial mixing of nanomaterial and PP on the properties of final melt extruded nanocomposite. Chapter 5 describes the effect of melt extrusion conditions on dry mixed nanocomposites. Chapter 6 provides details on the effect of melt extrusion conditions on hot coagulated nanocomposites. Chapter 7 explains the effect of melt extrusion conditions on rotary evaporated nanocomposites. Finally, Chapter 8 summarizes the main conclusions of this research.

Chapter 2

Background

Since nanomaterials exhibit higher surface area to volume ratios, they display drastically different properties than those of the same material on the macro or even micro scale (1). Nanomaterials have current and potential applications in many areas including drug delivery, semiconductors, sporting goods, optical devices, and chemical sensors. Carbon nanomaterials are also often used for applications requiring high strength, light weight and/or flame retardency. Polymer nanocomposites (PNC) are a class of materials fabricated by blending polymers and nanomaterials to alter the properties of the matrix and provide improved properties. An ideal PNC incorporates the outstanding properties of the nanomaterials while retaining the ease of processability of the polymer. Two key issues have to be overcome to achieve this, namely (a) the nanomaterials must be individually dispersed throughout the polymer matrix, and (b) strong interfacial interaction between the nanomaterials and polymer must be achieved.

Nanocomposites fabricated from carbon allotropes are of particular interest due to their extraordinary mechanical, thermal and/or electronic properties. Allotropes of carbon include diamond, graphite, amorphous carbons (including vapor grown carbon nanofiber), fullerenes and nanotubes (2). The discovery of Buckminsterfullerene, the first closed cage structure of carbon discovered, in 1985 by Sir Harry Kroto, Richard Smalley, and Bob Curl, led to their being awarded the Nobel Prize in 1996, and an active

search for other stable and ordered forms of carbon besides graphite and diamond. This resulted in the discovery of carbon nanotubes by Ijima in 1991 (3). However, the spectacular extraordinary mechanical, thermal, and electronic properties of carbon nanotubes are often negated by the difficulty in their dispersion. The extremely large surface area and perfectly smooth cylindrical walls of carbon nanotubes, a part of the reasons for their attractive properties, are also the reason for the difficulty in their dispersion. The high van der Waals forces of roughly 500 eV/μm, owing to the long smooth surfaces of the nanotubes, often lead to the formation of crystalline ropes (4). Nanoclays and nanoparticles have already been incorporated into polymers for over a decade. Knowledge of the extraordinary mechanical, thermal, and electronic properties of carbon nanotubes have led to significant thrust in understanding their potential use in polymer nanocomposites. Traditional fillers like glass fibers and carbon fibers are much larger in size and do not have as high van der Waals attraction between them as nanotubes do, and so are easier to disperse in a polymer matrix. However, they are thin fibers of a few microns in diameter. Due to their lower aspect ratios and chemical strucutre, they have mechanical, thermal, and electrical properties that are not as good as those of carbon nanotubes (5).

2.1 Polypropylene

First polymerized in 1995 by Natta et al. (6) from organo-metallic catalysts based on titanium and aluminum, polypropylene is amongst the most widely used polymers worldwide. The various forms of polypropylene are distinguished by its tacticity; namely isotactic, syndiotactic, and atactic. Isotactic polypropylene, the most common

commercial form is generally abbreviated PP and has all the pendant methyl groups on the same side of the zigzag plane. Syndiotactic polypropylene (sPP) has the pendant methyl group positioned alternatively on either side of the chain, while atactic polypropylene (aPP) is classified by the random positioning of the pendant methyl group on either side of the chain.

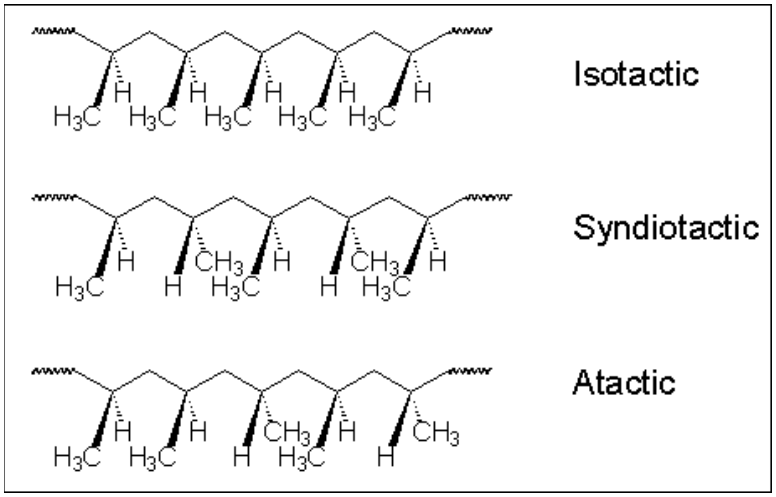

Figure 2.1. Stereo configurations of polypropylene: Isotactic, Syndiotactic, and atactic. Reproduced from J Cowie (7).

Atactic PP is an amorphous polymer due to the irregular placement of the pendant groups. In contrast, the regularity of isotactic PP allows the polymer chains to arrange themselves in an orderly manner during crystallization; thus resulting in increased crystallinity. The crystallinity of isotactic PP results in reasonably good mechanical properties such as a tensile strength of ~ 30 MPa. A less than desirable characteristic of polypropylene is its vulnerability to degradation leading to decreased molecular weight and consequent loss in properties, especially mechanical. PP is particularly susceptible to

oxidation due to the presence of the tertiary hydrogen on the carbon atom bonded to the methyl group (8). PP oxidation occurs through a free radical chain reaction. Stress, heat, or oxygen or the presence of metal catalysts can result in hemolytic cleavage of the carbon-hydrogen or carbon-carbon bond resulting in the formation of free radicals. The degradation chain reaction is propagated through the formation of a hydroperoxide, accompanied by the formation of another free radical. In further reactions, the hydroperoxide decomposes in the presence of heat or metal catalyst to form an alkoxy radical. Oxidative chain scission is believed to occur through the disintegration of this alkoxy radical. Oxidation in PP can be prevented by the incorporation of antioxidants; substances that inhibit oxidation. Antioxidants are generally divided in to two groups: primary antioxidants, which act as free radical scavengers to prevent oxidation reactions; and secondary antioxidants, which react with the hydroperoxide groups to convert them to non radical products (9).

The ease of processability of PP positions them as a widely employed thermoplastic utilized in a wide array of everyday applications such as kitchen appliances, toys, sports equipments, furniture, automobiles and many more. However, their relatively poor mechanical and thermal properties drastically limit their scope of further applications. An approach to improve their mechanical and thermal properties is by incorporating reinforcing materials such as glass fibers, carbon black, carbon nanofibers, carbon nanotubes etc.

2.2 Vapor Grown Carbon Nanofibers

Vapor grown carbon nanofibers (VGCFs), similar to the ordinary carbon fibers widely used in industry, are hollow cored fibers with diameters ~ 100 nm (10,11). The fibers can be of a single layer or double layer and are comprised of graphite planes stacked parallel or at an angle to the axis, as shown in Figures 2.2 and 2.3. VGCFs are produced by the deposition of carbon on a metal catalyst such as Fe or Ni by the pyrolysis of carbon containing gases such as methane or acetylene at ~1050 ^{o}C. Further annealing at higher temperature, ~2500 ^{o}C, causes the layers of tubes to crystallize and form a fiber with tree ring concentric cylinder morphology. VGCFs display a high tensile strength of 12 – 30 GPa and modulus of 100 – 775 GPa (11-13); the exact values are dependent on the fiber diameter. The stated mechanical properties are obtained only if good adhesion is achieved between the graphitic planes of the VGCF fiber. However, if they are weakly adhered to each other, the inner graphitic sheets can slide out leading to one the most

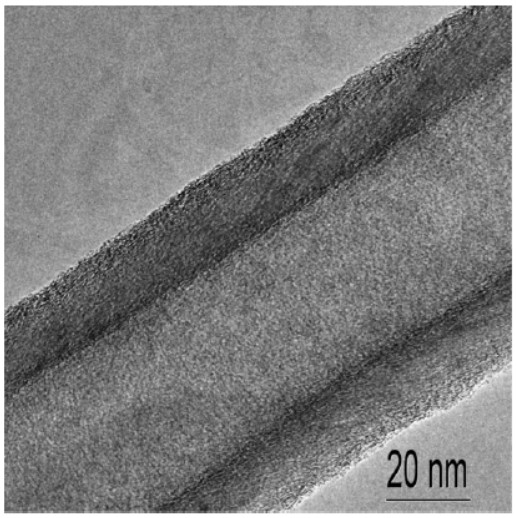

Figure 2.2. TEM showing the structure of VGCF. Image reproduced from Tibbetts et al. (14).

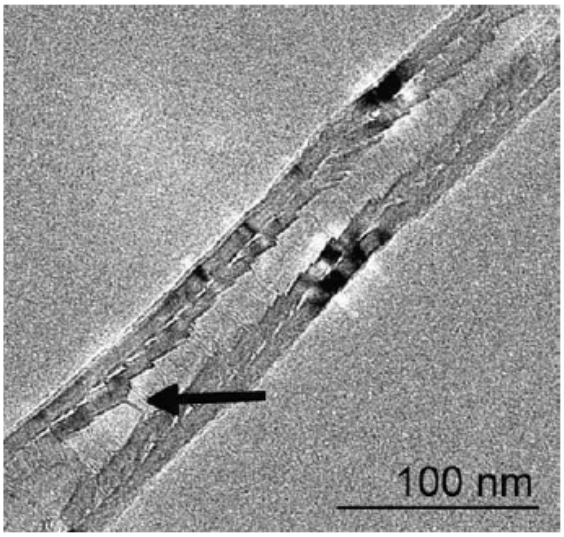

Figure 2.3. TEM of double-layer VGCF (arrow indicates closed graphite sheets in the hollow core region). Image reproduced from Uchida et al. (13).

common failures mechanisms in VGCF. Besides excellent mechanical properties, VGCFs also display high electrical conductivity and corrosion resistance.(11) In addition, the thermal conductivity of VGCFs, at 1950 W/m K, is higher than other carbon fibers (15). The lower costs and micro scale diameters of VGCFs lead to them often being considered as an alternative to traditional carbon fibers and carbon nanotubes.

2.3 Carbon Nanotubes

Carbon nanotubes (CNT) were first discovered in 1991 (3) and the first reports on polymer nanocomposites were published in 1994. CNTs, however, have inadvertently been in use for centuries. It has been claimed that the presence of CNTs in Wootz steel is the reason behind the legendary strength of the famous Damascus swords (16). CNTs are long cylinders, made up of sp^2 hybridized carbon atoms covalently bonded to each other.

They are classified as SWNTs, double-walled carbon nanotubes (DWNTs), or multi-walled carbon nanotubes (MWNTs) depending on if they are made up of one, two, or multiple coaxial cylinders. This section will focus on SWNTs as they are the only type of carbon nanotubes used in this research. A SWNT can be described as a graphene sheet rolled up into a one-dimensional cylinder. SWNTs typically have a diameter of approximately 1 - 2 nm and lengths that range from hundreds of nanomaters to a few microns. Their small size, large surface area, stiffness, and robust carbon-carbon bond lends them extraordinary thermal, mechanical and electronic properties. The thermal conductivity of SWNTs is more than 3000 W/K m and is higher than diamond (17,18). SWNTs possess tensile modulus of 0.6 to 1 TPa and strength of over 37 GPa, or, when density normalized, 60 times the strength of steel at just one-sixth the weight (19-22). Table 2.1 compares the physical properties of SWNTs and MWNTs to traditional fillers. SWNTs also possess excellent electric carrying capacity due to their 1-dimensionality and long lengths. However, electronic conductivity is highly dependent on the diameter and the chiral angle of the nanotubes. Small variations in the diameter and chirality can be the deciding factor between a nanotube being semiconducting or metallic (23,24). The diameter of the nanotube is determined by the chiral vector (25). The chiral vector $\mathbf{C}_h$ is defined in Equation 2.1 and is specified by n and m, a pair of integers with $0 \leq |m| \leq n$, and two unit cell base vectors of the grapheme sheet $\mathbf{a}_1$ and $\mathbf{a}_2$.

$$\mathbf{C}_h = n\mathbf{a}_1 + m\mathbf{a}_2 \tag{2.1}$$

The diameter of the carbon nanotube is given by L/π, where L is the circumferential length.

$$d_t = \frac{L}{\pi} = \frac{|C_h|}{\pi} = \frac{\sqrt{C_h \cdot C_h}}{\pi} = \frac{\sqrt{3} \cdot a \cdot \sqrt{n^2 + m^2 + nm}}{\pi} \tag{2.2}$$

Where, a = 1.44 Å is the lattice constant.

Depending on the wrapping, the nanotube can be classified as zigzag, chiral or armchair as seen in Figures 2.4 and 2.5. Consider two lines drawn along the tube axis (dotted lines T in figure). If the sheet is folded so that the two lines meet then it results in the formation of a seamless cylinder. If m = 0 then the resulting nanotube formed is called zigzag. For example, a zigzag nanotube is formed if the origin (0, 0) is folded to meet another point (11, 0). If n = m then the nanotube is called armchair, which occurs in the figure when the origin (0, 0) is folded along the dotted line labeled armchair to meet a point (11, 11). All other tubes are classified as chiral nanotubes. The line H indicates the

Property	**Carbon Fibers – Pitch** [a]	**VGCF** [b]	**MWNT** [c]	**SWNT** [c]
Diameter (nm)	7k- 10k	50 - 200	10 - 50	1 - 2
Length (μm)	> 1k	10 -100	10 - 50	1 - 5
Surface Area (m^2/g)	~ 1000	20 - 30	300 – 400	1315
Density	2 – 2.2	1.95	2.1	1.45
Tensile Strength (GPa)	0.6 - 0.75	2.92	11 – 63	150 – 180
Tensile Modulus (GPa)	30 - 32	240	270 - 950	600 - 1200
Thermal Conductivity (W/mK)	1000	1950	830	> 3000
Electrical Resistivity (Ω cm)	10^{-5}	10^{-4}	10^{-4}	10^{-4}
Cost ($/g)	0.02	0.5	150	500

a from Refs. (26-28)
b from Refs. (14,29-32)
c from Refs. (17,33-39)

Table 2.1. Estimated or measured physical properties of carbon fibers, VGCF, MWNT, and SWNT.

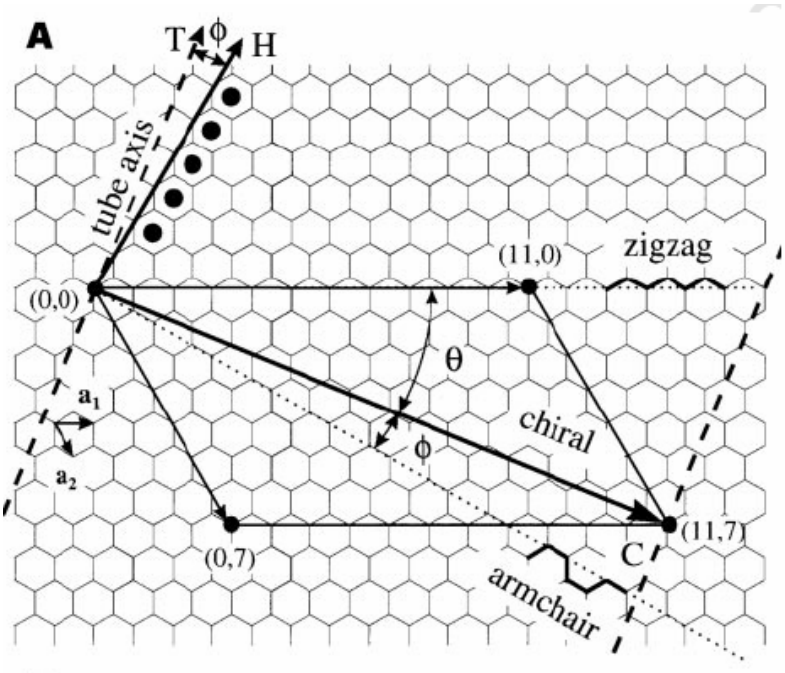

Figure 2.4. Construction of carbon nanotube from single graphene sheet. Image reproduced from Wilder et al. (25).

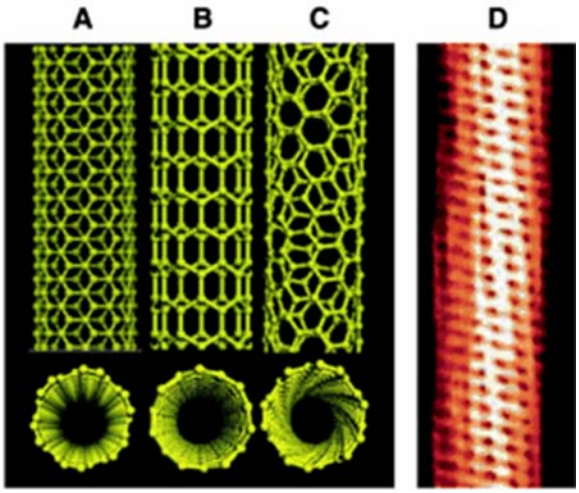

Figure 2.5. Schematic illustrations of the structures of (A) armchair, (B) zigzag, and (c) chiral SWNTs. (D) Tunneling electron microscope image showing the helical structure of a 1.3 nm diameter chiral SWNT. Image reproduced from Baughman et al. (19).

direction of the closest hexagon rows to the tube axis and the angle between the tube axis T and H is called the chiral angle or wrapping angle ϕ. Armchair nanotubes have a chiral angle of 0^o while the zigzag nanotubes have a chiral angles of 30^o. The chiral angle of chiral nanotubes ranges between 0 and 30^o. Figure 4 shows a schematic illustration of the various SWNT classifications. Armchair nanotubes ($n = m$), initially thought to be metallic as they have electronic bands crossing the Fermi level and the conduction and valence band overlap, are ballistic conductors (i.e., no scattering) providing excellent conduction with no heating and are only behind superconductors (40,41). Chiral and zigzag nanotubes, generally considered metallic if they satisfy the condition $(n - m) = 3l$, where l is an integer; in reality they have a very small band gap (42). If they do not satisfy the condition then they are semiconducting with a band gap that is inversely proportional to the nanotube diameter (43).

The aforementioned excellent properties of CNTs make them potential candidates for use in applications such as high strength materials, energy storage and energy conversion devices, sensors, hydrogen storage media, and nano sized semiconductor devices among others (19).

2.4 Carbon Nanotube Synthesis

Carbon nanotubes are mostly produced by arc discharge, laser ablation or chemical vapor decomposition (CVD). The electric arc discharge method was the earliest, and is amongst the easiest, methods of synthesizing CNTs. In this method, carbon nanotubes are generated in a He filled chamber containing two graphite electrodes and a catalyst like Ni-Co, Co-Y, or Ni-Y. An electric arc introduced in the chamber vaporizes the

carbon from one electrode as the cathode and deposits them on the other electrode resulting in the formation of carbon nanotubes (44-46). While the arc discharge method is relatively inexpensive and results in few defects in the nanotubes, it does not produce a homogeneous product and mostly results in a mixture of MWNTs and SWNTs. In addition, the products formed from this method tend to include large amounts of impurities, such as amorphous carbon and metal catalysts. The laser ablation method, developed by the Richard Smalley group (4,47,48), produces a more homogenous product of SWNT. Laser pulses directed on a graphite-metal target causes carbon species to be ejected and deposited on a copper collector. The laser ablation method results in nanotubes of higher yield and quality; while amorphous carbon, graphite particles, catalysts and fullerenes are amongst the major impurities formed in the product. Chemical vapor deposition (CVD) involves carbon in the gaseous phase and uses an energy source at 1100-1200 ^{o}C to impart energy to gaseous carbon molecules. The energy source chemically decomposes the carbon source into reactive carbon species which diffuse on to nanosized metal catalyst substrate below, forming carbon nanotubes (49). Benzene, methane, and acetylene are the most commonly used carbon sources while transition metals are used as catalyst particles to allow the carbon molecules to grow and form the nanotubes. An advantage of the CVD synthesis method is that it produces high yields of carbon nanotubes at relatively low cost compared to arc discharge and laser ablation. An issue with the CVD process, however, is that it typically uses hydrocarbons as a carbon source which tend to pyrolize readily at temperatures around 600-700 ^{o}C resulting in the formation of amorphous carbon on the nanotubes. As described in Nikolaev et al., the Smalley group overcame this issue by using CO as the

carbon source and iron pentacarbonyl ($Fe(CO)_{5)}$ as the catalyst (50). This led to the manufacture of the HiPco® nanotubes, one of the first scaleable methods but no longer believed to be the most promising in terms of cost for performance. The authors demonstrated the fabrication of SWNTs in a continuous flow gas phase process. The conditions employed were a pressure of 1 – 10 atm and temperatures of 800 – 1200 ^{o}C. The feed to the reactor was a mixture of CO at 1 – 2 liters/min with a small amount of $Fe(CO)_5$. $Fe(CO)_5$ thermally decomposes to form iron atoms that aggregate and collide with each other to form larger clusters. Eventually, these clusters grow to a size of the diameter of a SWNT. CO in the feed disproportionate into C and CO_2 (the Boudouard reaction), forming solid carbon leading to the nucleation and growth of SWNTs. The authors found that, depending on the conditions employed, they could result in a wide range of diameters and yield of SWNTs with no amorphous carbon residue coating the nanotubes.

$$2CO \rightarrow C\ (s) + CO_2 \qquad (2.3)$$

The Daniel Resasco group produced SWNTs of very narrow diameter and chirality distribution by developing the CoMoCat method (51-53). This method produces SWNTs by disproportioning CO on a bimetallic Co-Mo catalyst supported on silica. The production of SWNTs can be controlled to produce a majority of a desired chirality by altering the reaction conditions. It has been shown that SWNTs, with (6, 5) being the dominant chirality, can be produced by carrying out the synthesis at 750 ^{o}C and 80 psig.

Synthesis	Discovery	Purity	Yield	Impurities
Arc Discharge	1991 (3)	34 % (54)	40 % SWNT (55)	Amorphous carbon, metal catalysts
Laser Ablation	1995 (4,47,48)	90 % (56)	> 70 % SWNTs (4)	Amorphous carbon, graphite particles, catalysts, and fullerenes
Chemical Vapor Deposition	1999 (50)	> 90 % (57)	~ 95 % (57)	Amorphous carbon, catalyst particles

Table 2.2. Carbon nanotube synthesis methods.

2.5 Polymer Nanocomposites

Polymers that contain nanomaterials, materials with at least one dimension less than 100 nm, are called polymer nanocomposites. Carbon black, alumina and titania nanoparticles have traditionally been used as reinforcing fillers in polymer nanocomposites. The excellent properties of carbon nanotubes make them promising materials for producing polymer nanocomposites. The key to fabricating an ideal polymer nanocomposite is to ensure that the properties of the nanotubes are effectively incorporated into the polymer. In order to do this, the nanotubes must be evenly distributed and individually dispersed throughout the polymer matrix. Carbon nanotubes possess very high aspect (length to diameter) ratios; it is all the more important to maintain their high aspect ratios in the polymer matrix in order to achieve percolation at low nanotube concentrations, thus requiring their individual dispersion. Individual nanotube dispersion also leads to a larger percent of the polymer in the stabilized interphase region. Additionally, the

nanotubes and the polymer should be compatible and must have good interfacial interaction. Any stress applied to the bulk nanocomposite must be effectively and efficiently transferred to the nanotubes which have a higher threshold to withstand high loads. The immense surface area to volume ratio of nanotubes provide large interfaces for stress transfer; however it also increases the total van der Waals forces of attraction between the nanotubes often resulting in the formation of ropes and aggregates. Achieving dispersion and interfacial interactions are inhibited by these strong van der Waals attraction between nanotubes (4) and the molecular perfection of the SWNTs themselves making them amphiphobic (58). Various methods for processing SWNT polymer nanocomposites have been explored including in-situ polymerization, solution mixing, and melt extrusion.

2.5.1 In situ Polymerization

In situ polymerization requires dispersion of nanotubes in a monomer followed by polymerization of the monomers. The nanotubes are usually dispersed in a solvent by the aid of sonication (59,60). The sonicated nanotube suspension is then added to the monomer, where, in some cases, the nanotubes act as an initiator for polymerization. In addition to gaining good interaction between the nanotubes and the polymer matrix, in situ polymerization is also helpful in grafting the polymer chains to the nanotube sidewalls. Hu et al. reported MWNT-polyimide nanocomposites by in situ polymerization of monomers with acylated-MWNTs (61). The acyl groups on the MWNTs formed amide bonds with the polymer, thus resulting in good interfacial interaction between the tubes and the polymer matrix. The authors reported that an

addition of approximately 0.3 vol. % (0.5 wt. %) MWNT resulted in over 10% improvement in mechanical properties of the nanocomposite. Other researchers have also reported that the presence of a chemical group on the sidewalls of the nanotubes can help improve the interfacial interaction between the nanotubes and polymer matrix. Kim et al. reported that the acid chloride groups attached to MWNTs helped graft nylon-6,10 polymer to the MWNT by reaction between the acid chloride group and the terminal amino group of the polymer (62). This resulted in improved interaction and compatibility, and 30% improvement in tensile strength at MWNT concentration of 0.05 vol. % (0.1 wt. %). McIntosh et al. demonstrated a one step in-situ functionalization method, generally referred to as a 'grafting to' method, of fabricating PP/SWNT nanocomposites where they decomposed benzoyl peroxide, using high shear and temperature, to create free radicals that initiated a reaction that linked the SWNTs to the surrounding PP chains by covalent bonds (63). The resulting composite demonstrated mechanical properties improvements ranging from 80 – 170 %. While the 'grafting-to' method ensures controlled polymer molecular weight by using preformed polymers, a disadvantage of this method is that, anytime preformed polymer chains are attached to the nanotube surface, the chains attached to the nanotubes tend to sterically hinder the grafting of more chains on to the same tube, thus decreasing the overall grafting density (64).

A disadvantage of the in situ polymerization method is that as polymerization increases, the viscosity of the blend also increases and this tends to limit the extent of polymerization. Also, the use of solvent to disperse the nanotubes increases cost and makes it environmentally unfriendly. Another drawback of in-situ polymerization is that

it can be difficult to achieve initial nanotube dispersion. In most cases, it requires sonication to disperse the nanotubes which might result in damage to the tubes. Liang et al. reported the use of debundled SWNT-Li salts as anionic initiators for in-situ polymerization of methyl methacrylate onto the surface of SWNTs (65). They effectively showed a simple scalable method of using SWNT salts as initiators to result in exfoliated SWNTs, without the use of sonication, that are covalently attached to the polymer. In general, in situ polymerization method of fabricating nanocomposites is especially attractive for processing thermally unstable and insoluble polymers (64).

2.5.2 Solution Mixing

Solution mixing is a commonly used method of polymer nanocomposite fabrication. It is essentially executed in three steps: the nanotubes are dispersed in a suitable solvent or polymer solution, the nanotube suspension is mixed with the polymer solution, the composite is cast into a sheet and the solvent is allowed to evaporate. Nanotube dispersion in the solvent and polymer solution is achieved with the aid of ultrasonication, magnetic stirring, or high shear mixers. The choice of solvent used is critical in solution mixing. Slobodian et al. fabricated PMMA-MWNT nanocomposites up to 12 vol. % (20 wt. %) by dissolving PMMA in toluene, acetone and chloroform and mixing this solution with a MWNT-HCl suspension (66). The mixture was further sonicated to achieve better dispersion of nanotubes and mixing, followed by solvent casting. The authors studied the electrical conductivity of the nanocomposites and found that the percolation threshold depended on the solvent used to dissolve PMMA. It was observed that using toluene as the solvent resulted in percolation at a lower concentration of MWNT at around 2.3 vol.

% (4 wt. %), while using chloroform and acetone resulted in percolation at 4 vol. % (or 7 wt. %) and 5.8 vol. % (or 10 wt. %) respectively. This indicated that the nanotubes achieved a higher degree of dispersion in toluene, followed by chloroform and acetone. The authors attributed this result to the higher dispersion component and lower polar and hydrogen bonding components of the Hansen solubility parameters of toluene. Khan et al. studied the effect of solvent used in solution mixing on the mechanical properties of double-walled carbon nanotube (DWNT)-polyvinyl alcohol (PVA) nanocomposites (67). Their studies showed that nanocomposites made of water and dimethylsulfoxide systems showed mechanical improvement while those made of N-methyl-2-pyrrolidone did not. The authors attribute this lack of improvement in mechanical properties of the NMP system to the fact that NMP was trapped at the interfaces of the nanotube and polymer resulting in inefficient stress transfer from the polymer matrix to the nanotubes.

Haggenmueller et al. studied the crystallization kinetics of PE-SWNT nanocomposites prepared by a modified solution mixing method, referred to as hot coagulation, using 1, 2-dichlorobenzene (DCB) (68). The method included dispersing the nanotubes in DCB by sonication, dissolving the polymer in DCB by heating, mixing the nanotube-DCB suspension and polymer-DCB solution, and finally removal of DCB to result in the nanocomposite. They found that highly uniform nanocomposites can be fabricated with as high as 20 vol. % (30 wt. %) SWNTs. Similar to the method employed by Haggenmueller et al., Kearns et al. demonstrated up to 40 % increase in tensile strength and 55 % increase in modulus of fibers of 1 wt. % PP/SWNT fabricated by solution mixing employing decalin as a solvent (69). The authors mentioned that, at higher loadings, fiber spinning was difficult; this led to strength and modulus values

lower than that of pure PP. The authors also investigated the effect of sonication-mixing time and estimated an optimal sonication-mixing time of 2 h. Mixing time below the optimal time was found to result in poor dispersion of nanotubes, while higher than optimal mixing times resulted in nanotube breakage and damage. In addition, the authors also found that solvent choice played an important role in the final nanocomposite properties. A comparison between decalin and toluene solvents for dispersing nanotubes before mixing with a solution of PP/decalin showed that toluene significantly decreased the nanocomposite strength and modulus, even though toluene has been acknowledged as a relatively good solvent for nanotube dispersion (70).

It is clear that while solution mixing can provide intimate mixing of the nanotubes and polymer, the method has some drawbacks that render it unfavorable. First, as in most in situ polymerization cases, high power ultrasonication or agitated mixing needs to be employed for good dispersion of nanotubes in solvent leading to possible damage or breakage. Second, the properties of the resulting nanocomposite are strongly dependent on the choice of solvent. In addition, the large volumes of solvents required, besides being environmentally unfriendly, can drastically increase costs. These limitations with respect to nanotube dispersion and solvent choices significantly limit the applicability of this method to industrial scales.

2.5.3 Melt Processing

The most commonly used melt processing techniques include melt extrusion (71,72), blow molding (73), and injection molding (74,75). Melt processing is used to mix molten polymers and nanomaterials and can be used to form nanocomposite fibers,

pellets, rods or solids of any other shape and size. Typical melt processing methods involve melting the polymers at elevated temperatures followed by the incorporation of the nanomaterials, and any other additives, with the aid of high shear.

Kumar et al. manufactured polypropylene - carbon nanofiber nanocomposite by melt extruding in a Haake twin screw extruder at a ratio of 19:1 at an extrusion temperature ranging from 150 to 240 ^{o}C and speed of 20 rpm (76). This resulted in evenly distributed nanofibers in the polymer matrix; the composite fiber moduli increased by 50%. Zhang et al. achieved electrical percolation at 2.7 vol. % (4 wt. %) and rheological percolation at 1 vol. % (1.5 wt. %) in SWNT - high density polyethylene (HDPE) nanocomposites by spraying a suspension of SWNTs on the surface of the polymer powder, followed by melt extrusion in a DACA micro compounder co-rotating twin screw at 160 ^{o}C and 50 rpm for 20 min (77). They found that the tensile strength of the composite increased by 65% at a loading of 1.75 vol. % (2.6 wt %). Dondero and Gorga (71) reported up to 32% increase in toughness of polypropylene-MWNT (0.1 vol. % or 0.25 wt. %) melt extruded at 100 rpm and 200 ^{o}C for 10 min in a Haake minilab twin screw extruder. They also reported up to 138% increase in modulus due to efficient load transfer from the polymer to the nanotubes. Manchado et al. observed an increase of up to 40% in tensile modulus, reported value of 1187 MPa, for a loading of up to 0.5 vol. % (0.75 wt. %) SWNT in polypropylene processed by melt extrusion at 190 ^{o}C, 60 rpm and 15 min (78). Upon further increasing SWNT content to 0.67 vol. % (1 wt. %), they found that the modulus decreased to 1087 MPa. This decrease was attributed to the fact that more SWNTs were packed into the same volume, and this probably resulted in aggregation. In general, the tensile modulus and strength of a polymer nanocomposite

increases with nanotube loading up to a certain point beyond which high viscosity and close proximity of nanotubes facilitates aggregation and negatively affects the properties (71,76,78-81). This is critical since many studies only explore high concentrations and thus, inadvertently, investigate aggregated systems. In addition to concentration, the time of shearing employed is a critical factor in melt processing. If mixing time is less than the critical time, the resulting nanocomposite will contain nanotube aggregates and lead to nanocomposites with poor properties (82). The critical time of mixing is a function of nanotube concentration and total shear applied. Higher concentrations typically require longer processing time to allow for effective nanotube dispersion while higher applied shear generally decreases the processing time required. However, applying very high shears can also result in breakage of the nanomaterials, especially carbon nanofibers and MWNTs, and thus decrease their effectiveness and increase the concentration required for percolation. Andrews et al. studied the effect of total shear energy on the length and dispersion of 0.5% vol. MWNTs in polystyrene (83). Their observations, shown in Figure 2.6, highlight that while high shear energy tend to result in better dispersion of nanotubes in the polymer, this is achieved at the expense of decreased nanotube length. Thus, many factors need to be considered and controlled in fabricating polymer nanocomposites.

Melt extrusion is one of the most common processing methods employed and most materials undergo some form of melt processing during manufacture. However, there is still a lot to be learned about the effect of processing conditions on nanotube dispersion and polymer degradation in polymer nanocomposites (83). In general, melt extrusion results in a well reinforced nanocomposite only if the process can achieve

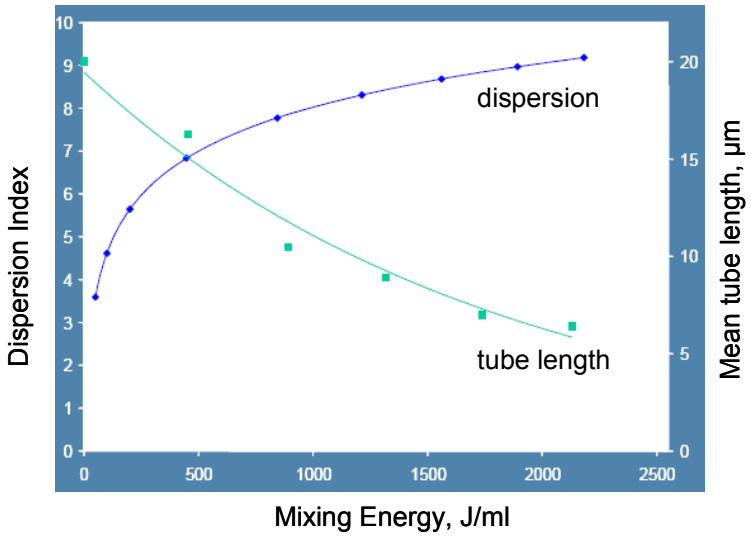

Figure 2.6. MWNT dispersion and length and a function of mixing energy. Image reproduced from Rodney et al. (83).

dispersive and distributive mixing without damage to polymer or nanomaterial. Dispersive mixing reduces the length scale of the agglomerates by the application of high stress while distributive mixing rearranges the materials to achieve homogeneity through the entire nanocomposite. Either type of mixing by itself will not produce a good polymer nanocomposite. Dispersive mixing by itself will result in domains of reduced size agglomerates while distributive mixing will only result in an even distribution of large agglomerates in the matrix. The advantages of melt processing include its ability to process large volumes, ease in execution, and conformity to present industrial techniques and infrastructure etc. In addition, the fact that melt processing techniques are free of solvents and environmentally friendly makes them particularly desirable in fabricating polymer nanocomposites. A disadvantage of melt processing is that it cannot be used to process nanocomposites of high molecular weight polymers as the resulting high viscosity in the melt state does not permit good mixing.

The work presented here employs a Haake Minilab twin-screw counter-rotating extruder. The advantages of the Minilab is that it requires a small volume of materials (~ 5 cm^3) and a backchannel allows for the material recirculation through the barrel until the desired level of mixing is achieved. A disadvantage is its low shear design with limited mixing.

2.6 Dispersion

Achieving a stable dispersion of nanotubes is one of the main challenges in realizing the amazing potential of polymer nanotube composites. Familiarity with the pair potential, the total potential energy of interaction between components, is key to realizing and achieving stable nanotube dispersions (84). The work done by Derjaguin and Landau (85), and Vervwey and Overbeek (86), known as the DLVO theory, provides a comprehensive framework to understanding the stability of carbon nanotube dispersions. The DLVO theory summarizes the total interaction potential between two components as the net effect of the attractive and repulsive interaction. The intermolecular attractive interaction is a result of the dispersion interaction (or London interaction), dipole-dipole Keesom interaction, and the dipole-induced dipole Debye interaction. The London dispersion interaction comprises molecular interaction leading to attraction between non-polar entities. The large surface areas of the long and perfectly smooth nanotubes result in strong van der Waals attractions of 500 eV/μm (0.08 nJ/m) (4). Such high attractive forces cause the nanotubes to stick together and form crystalline ropes and bundles (87). A theory to estimate the attractive interaction was provided by Hamaker (88), which summarizes the interaction as a function of the material property (expressed as the

Hamaker constant, A) and geometry, and assumes that the attractive interaction are pair wise additive (84). As shown in the figure 2.7, each atom on one component has an attractive interaction with each of the atoms on the other component. This results in significantly large attractive forces, especially in the case of SWNTs, owing to their larger surface area to volume ratio, where all the atoms are essentially on the surface of the tube.

The Hamaker constant is a function of the electronic polarizability, ionization frequency, and the number density of molecules in the material. Equation 2.3 gives the expression for A.

$$A_{12} = \pi^2 C \ \rho_{N1}\rho_{N2} \qquad \text{(Eqn 2.3)}$$

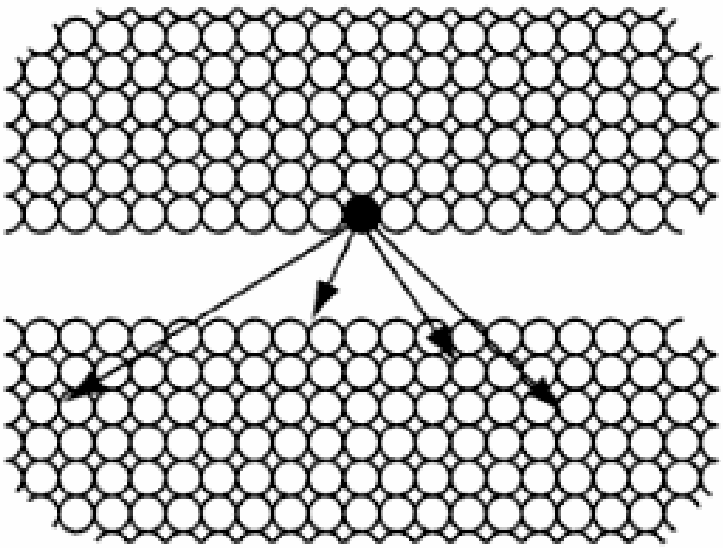

Figure 2.7. The summation of the atomic dipolar interactions between two slabs of material. Image reproduced from Goodwin (84).

C is the interaction parameter and is a function of the ionization energy of the outer electrons and the polarizability, ρ_N is the number density of molecules in the material, and the subscripts 1 and 2 represent the two materials 1 and 2. The Hamaker constant is typically estimated to be on the order of 10^{-19} to 10^{-20} J (88,89). Interactions between carbon nanotubes can be estimated using the attractive potential of two parallel cylinders given below in Equation 2.4.

$$W = -\frac{AL}{12\sqrt{2}D^{\frac{3}{2}}}\left(\frac{R_1 R_2}{R_1 + R_2}\right)^{\frac{1}{2}} \quad \text{(Eqn 2.4)}$$

In order to maintain a stable dispersion, as predicted by the DLVO theory, the attractive interactions have to be offset by repulsive interactions. Repulsive interactions are mostly electrostatic in nature; like charges repel each other. The total interaction energy, summed up as only dependent on van der Waals (vdW) attractive interaction and electrostatic (es) repulsive interaction, can be summed up as in Equation 2.5.

$$W_T = W_A + W_R \quad \text{(Eqn 2.5)}$$

A representation of the net interaction energy as a function of interparticle distance is reproduced in Figure 2.8.

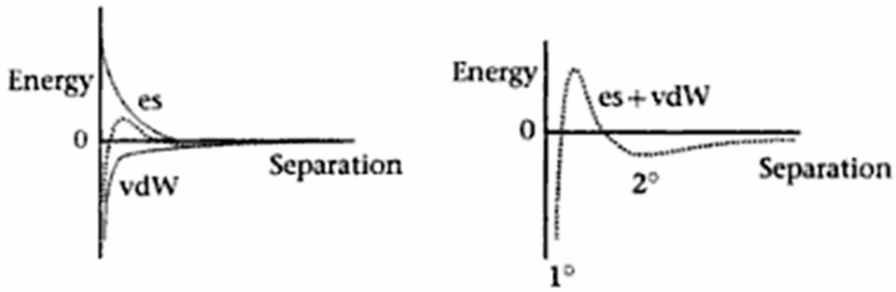

Figure 2.8. A representation of the total interaction potential as a function of separation distance. Image reproduced from Parsegian (90).

The attractive forces tend to work over longer ranges of distance, thus creating a secondary minimum (2^o). For parallel cylinders the forces scale with distance$^{-1.5}$ (89). The secondary minimum results in a metastable flocculation of particles, and can be easily overcome by shear or other forces to result in a dispersed state. The maximum peak in the schematic represents the energy, due to electrostatic repulsion, that must be overcome to result in an irreversible aggregation of particles, represented by the primary minimum (1^o). It has also been established that when nanotubes are stacked against each other in bundles, tubes of diameter d > 3 nm tend to form honeycomb structures, which is all the more reason to maintain them in a dispersed state (91,92). Coffin et al. studied the force required to break up ropes of nanotubes and found that it takes much lower forces to peel the nanotubes apart rather than dilation where the nanotubes are pulled apart transversely (93).

A widely used method to break apart the CNT bundles and aid dispersion is the application of high energy ultrasound, also known as sonication or ultrasonication. Sonication works by generating alternate low and high pressure waves in the solvent containing the nanotubes, leading to cavitations. The vapor bubbles implode aggressively, resulting in exceptionally strong shear forces that break apart nanotube bundles. Sonicators are usually classified as either bath sonicators or probe sonicators. A bath sonicator generates low energy that is transferred through the solvent from the transducer in the bath; while a probe sonicator generates much higher energy by dipping a probe, which is the source of energy, in the solvent. Due to the higher energy applied, a probe sonicator runs a much higher risk of mechanically damaging the nanotube than the bath sonicator. Lu et al. observed buckling, bending, and stripping of outer layers of

MWNTs when probe sonicated in methylene chloride (94). Lucas et al. investigated nanotube scission under sonication, and found that the average MWNT length scales with sonication time as t^{-n}, where $n \sim 0.2$ (95). Cheng et al. investigated the effects of sonication parameters and solvent properties on sonicated SWNTs dispersions (96). Their investigation revealed that the effect of sonication is largely dependent on the solvent (solvent viscosity, surface tension, gas solubility, and molecular weight), ambient temperature and pressure, sonication intensity, sonication frequency, and sonication time. They found that the dispersion limit, defined as the concentration at which aggregates cease to govern the dispersion, while significantly dependent on the sonication process, was, however, largely unaffected by the degree of sonication (sonication time and energy); demonstrating that the dispersion limit is possibly affected by solvent parameters and not just sonication conditions. The solvent parameters of chief importance are the solvent solubility parameters. It has been widely acknowledged that "like seeks like"; materials with similar solubility parameters are compatible (97). Solubility parameters can be obtained from the vaporization energy of a material since they are an estimate of the energy that is holding the molecules together. An approach towards estimating solubility parameters proposed by Charles Hansen, referred to as the Hansen solubility parameters, is widely used for predicting polymer solubility (97). The Hansen approach estimates that the vaporization energy depends on three components: dispersion, polar, and hydrogen bonding. Thus the Hansen solubility parameter is divided in to the Hansen D (or dispersion) parameter δ_D, Hansen P (or polar) parameter δ_P, and the Hansen H (or hydrogen bonding) parameter δ_H. The Hansen solubility parameter relates to the Hildebrand solubility parameter, δ_T, as shown in Equation 2.6;

$$\delta_T{}^2 = \delta_D^2 + \delta_P^2 + \delta_H^2 \qquad \text{(Eqn 2.6)}$$

To achieve a thermodynamically stable solution, the free energy of mixing must be zero or negative. The free energy of mixing is estimated by the relation

$$\Delta G_m = \Delta H_m - T\Delta S_m \qquad \text{(Eqn 2.7)}$$

Where, ΔH_m is the enthalpy of mixing, ΔS_m is the entropy of mixing, and T is the temperature. It is desirable to have as low a value for enthalpy of mixing as possible in order for the free energy to be lower than zero. An estimate of the enthalpy of mixing is obtained by the relation (98)

$$\Delta H_m = \chi\phi(1-\phi)\frac{kT}{v_o} \qquad \text{Eqn (2.8)}$$

Where χ is the Flory-Huggins interaction parameter, Φ is the volume fraction of the solute, v_o is the solvent molecular volume, and k is the Boltzmann constant. The Hansen solubility parameters can be used to estimate the Flory-Huggins interaction parameter, χ, as

$$\chi \approx \frac{v_o}{kT}\left[\left(\delta_{D,A} - \delta_{D,B}\right)^2 + \left(\delta_{P,A} - \delta_{P,B}\right)^2 + \left(\delta_{H,A} - \delta_{H,B}\right)^2\right] \qquad \text{(Eqn. 2.9)}$$

where, the subscripts A and B refer to the solute and solvent respectively. To obtain as low a value for the enthalpy of mixing as possible, it is necessary that the interaction parameter have a value close to zero. This is achieved if all three solubility parameters of the solvent and solute are equal or close to each other. Thus, it is imperative that the solubility parameters match in order to result in a stable solution. While it is important that the enthalpy of mixing is low, a negative free energy of mixing can also be achieved if the entropy of mixing is large. This is possible in the case of solvents with small

molecules, such as methanol or acetone, which have more flexibility in their possible conformations as opposed to larger molecules, resulting in higher entropy. This allows small solvents to dissolve materials with wider difference in the solubility parameters. However, polymers and nanotubes are much bigger; resulting in smaller entropies of mixing (99). Thus, in the case of nanotubes and polymers, it is all the more important that the solubility parameters match that of the solvents. While the solubility parameters of nanotubes are not yet firmly established, many researchers have estimated it by measuring nanotube dispersability in a range of solvents of known solubility parameters. Bergin et al. estimated optimal Hansen solubility parameters for SWNTs to be δ_D = 17.8 $MPa^{1/2}$, δ_P = 7.5 $MPa^{1/2}$, and δ_H = 7.6 $MPa^{1/2}$ (99), while Detriche et al. estimated optimal solubility parameters of δ_D = 19.4 $MPa^{1/2}$, δ_P = 6.0 $MPa^{1/2}$, and δ_H = 4.5 $MPa^{1/2}$ (100). It should be noted, however, that these estimates do not agree with experimental observations (39).

Even when successful dispersion of nanotubes in polymers has been achieved, the interfacial interaction obtained has sometimes been poor due to incompatibility between the nanotubes and the polymer. For a polymer nanocomposite to serve its purpose, any stress applied to the bulk composite has to be transferred to the nanotubes. Poor interfacial interactions result in ineffective stress transfer and, more often than not, results in the failure of the nanocomposite. Enhanced nanotube dispersion and polymer-nanotube interaction can be achieved by attaching chemical species to nanotubes or polymer to help make them compatible.

2.7 Nanotube Functionalization

High energy dispersion of carbon nanotubes does not necessarily prevent reaggregation of the tubes once the energy source is removed, especially in low viscosity fluids. Reaggregation can be prevented by attaching chemical species to the nanotubes, thus creating steric hindrance and/or increasing compatibility with polymers. Alternatively, the polymer can be modified to improve compatibility. For effective steric hindrance, a large portion of the nanotube surface must be modified. Figure 2.9 depicts a schematic of the various conformations available to functional groups attached to a surface. Under low degrees of functionalization, the functional groups tend to coil with a non-uniform concentration profile that peaks at a distance from the particle surface, shown in Figure 2.9a. As the degree of functionalization increases, as shown in Figure 2.9b, each of the functional groups has lesser space available, and thus tend to stretch out. An optimal degree of functionalization will result in uniform functional group concentration profile at all distance from the particle surface before reducing due to the length of the groups. As shown in Figure 2.9c, no steric interaction is experienced until the outer part of the functional groups on one particle is in close contact with a neighboring particle. As the particles get closer, the functional groups on their surface get in to closer proximity and begin interacting, resulting in a higher concentration of functional groups in the interacting region. The higher functional group concentration in the interacting region compared to the non-interacting regions immediately adjacent to the particles result in an osmotic pressure that acts to separate the particles.

Functionalization methods can be classified into two types; non-covalent and covalent functionalization. The interaction of the π-bonds on the carbon nanotubes with

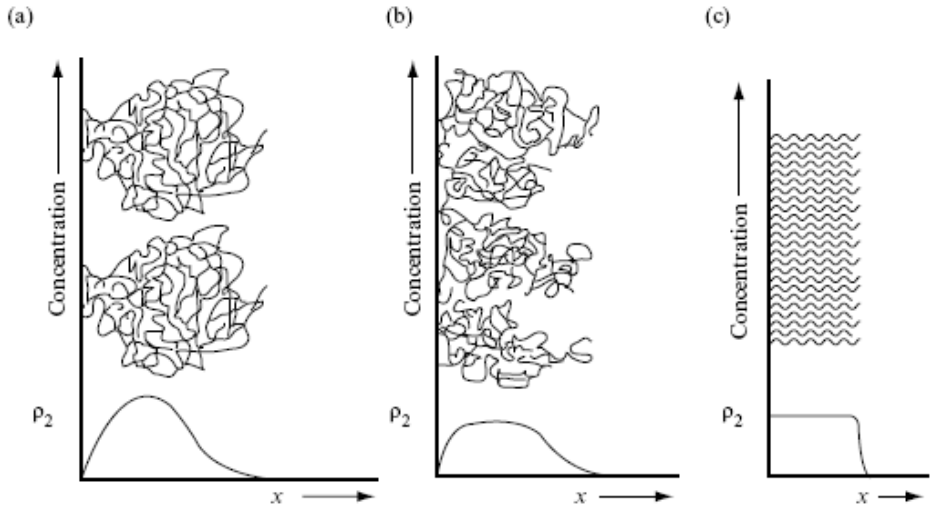

Figure 2.9. Schematics of concentration profiles of adsorbed layers. Image reproduced from Goodwin (84).

those on the polymers, surfactants, or biomolecules can result in non-covalent functionalization. O'Connell et al. non-covalently functionalized SWNTs to make them water soluble by tightly wrapping their sides with water soluble polymers such as polyvinyl pyrrolidone and polystyrene sulfonate (101). This method of functionalization can be used for purification and separation of nanotubes, and has also been applied to fractionate SWNTs, modified with the aid of nucleic acids such as DNA or RNA, based on their lengths by gel electrophoresis (102). Zheng et al. non-covalently wrapped nanotubes with DNA to separate metallic and semiconducting CNTs by studying the variability of the effective linear charge density of the negatively charged DNA-CNT hybrid in the presence of a positively charged anion exchange resin (103). Non-covalent functionalization is attractive because it does not affect the structure, and hence the mechanical properties, of the nanotube. However, non-covalent interactions between CNTs and the functional groups are not very strong and can result in ineffective load

transfer from the polymer to the nanotubes (104). In contrast, covalent functionalization is more stable and is further classified into end and defect site functionalization, and sidewall functionalization.

2.7.1 End and Defect Site Functionalization

End and defect site covalent functionalizations take advantage of the fact that nanotubes are more reactive at the ends where they are under a higher strain than at the sides, and at defect sites; π-orbital misalignment between carbon atoms is one of the main causes of high strains in CNTs. Since π-orbital misalignments are inversely proportions to the nanotube diameter, an increase in reactivity is seen as the nanotube diameter decreases (105). End and defect site covalent functionalizations are usually carried out under oxidizing acid media, typically mixtures of nitric and sulfuric acids, which open up the end caps of the nanotube and attach the acidic functionalities to the defect sites (106). The oxidized nanotubes can then be activated further to attach chemical groups by noncovalent esterification or amidation (107,108). However, the significant use of acids in these methods leads to considerable decrease in the nanotube length depending on reaction time (109). Liu et al. found that the length of SWNTs, at 70 ^{o}C in a mixture of 3:1 concentrated sulfuric acid and nitric acid, shortened at a rate of 130 nm/hour (106). Research by Forrest et al. shows that nanotube breaking occurs due to defect creation by oxidation followed by tube cleavage (110). Their work also resulted in a model relating oxidation time and nanotube length, and demonstrated that oxidation time is an easily tunable factor to control nanotube length. It should be noted that sulfuric acid or other

sulfonic acids alone are not oxidizing and do not functionalize the CNTs even after prolonged mixing at elevated temperatures (111).

2.7.2 Sidewall Functionalization

An option to reduce the effect of functionalization process on the nanotube length is covalent sidewall functionalization, which was the type of functionalization used in this research. A schematic, developed by Banerjee et al., depicting the various covalent sidewall functionalizations possible is shown in Figure 2.10 (112). Some of the more common sidewall functionalizations include fluorination, ozonolysis, and alkylation.

Liang et al. (113) studied the reductive alkylation of SWNTs by lithium in liquid ammonia wherein the reduced nanotube salts are reacted with alkyl halide groups to functionalize the nanotubes. The functionalization resulted in one alkyl group attached to the sidewalls of the nanotube for every 17 to 35 carbon atoms. Microscopy characterization of the alkyl functionalized SWNTs revealed significant debundling of the SWNT ropes due to intercalation of the alkali metal (114). It was observed that the alkyl functional groups burned out between 180 to 330 ^{o}C to result in pristine SWNTs. The authors also studied the impact of the reducing agent used in the functionalization process and found that nanotube salts produced using Na/NH_3, K/NH_3 and Li/NH_3 results in materials that exhibit vastly different properties. The use of Na as the reducing agent resulted in more thermally stable nanotubes and a higher degree of functionalization than Li or K (114). A study by Rai et al. revealed that covalent functionalization of SWNTs with alkyl groups improved their solubility in strong acids (115). While covalent functionalization can create ways to customize the polymer-nanocomposite interface so

as to harness the best properties, it does result in the disruption of π conjugation in nanotubes by formation of sp^3 hybridized carbon. This disruption does not significantly affect the mechanical and thermal properties, but its effect on the electronic properties of the nanotube is considerable. The disruption of π conjugation results in a decrease in electrical conductivity of the nanotube due to scattering of electrons by the covalent functionalization site. The functionalization route selected should therefore consider the final properties that are required of the nanotubes and the balance between improved composite properties resulting from better dispersion and the decrease in intrinsic nanotube properties.

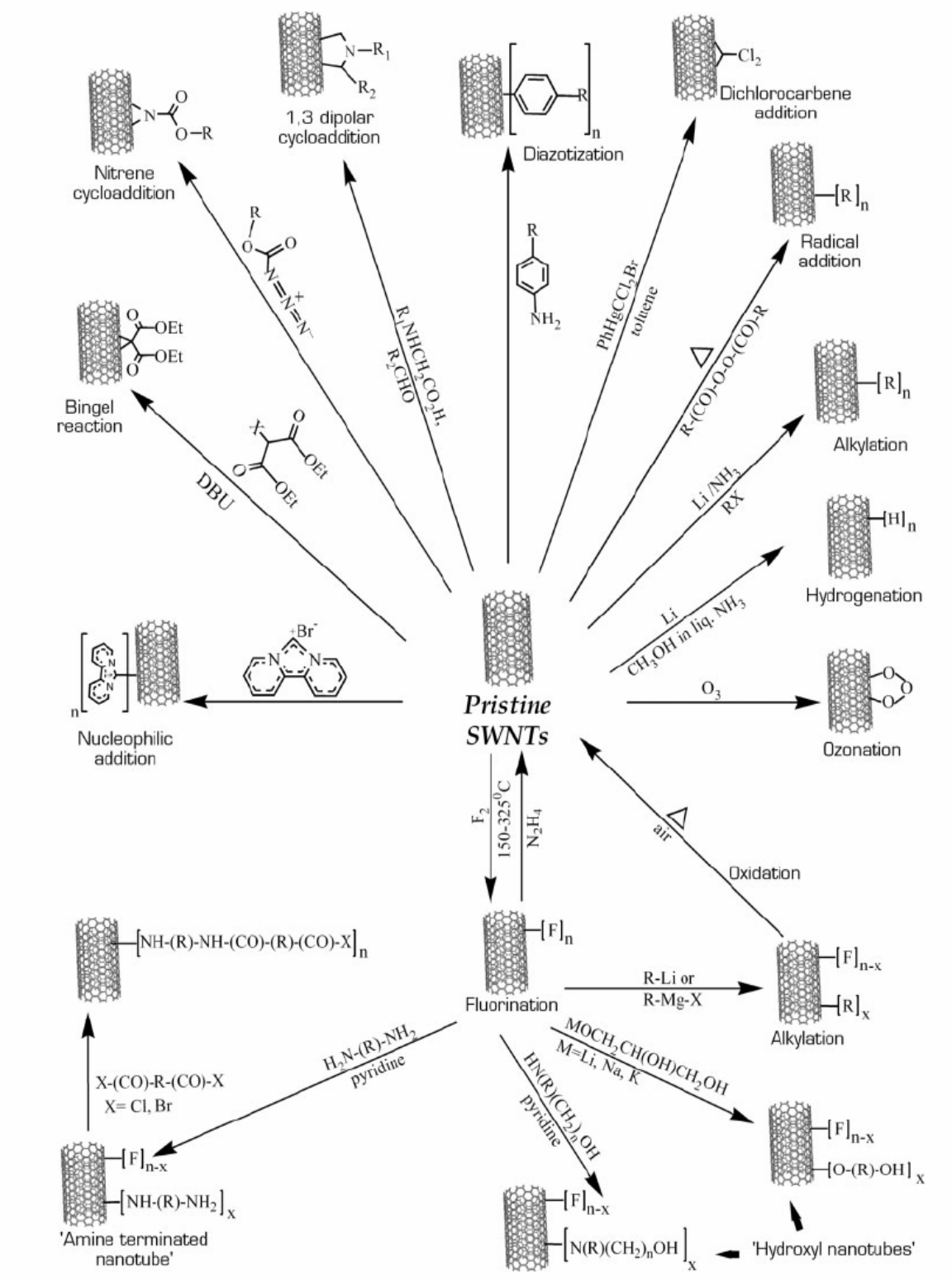

Figure 2.10. Covalent sidewall functionalization of SWNTs. Image reproduced from Banerjee et al. (112).

2.8 Interfacial Interaction and Load Transfer

In order for a PNC to serve its purpose as a strong structural material it has to ensure that any stress applied on it must be transferred to the nanomaterial which has a higher threshold for withstanding the load. This is achieved by ensuring effective interfacial interaction between the nanomaterials and polymer matrix. The very high interfacial areas of nanomaterials provide them with large interfaces for stress transfer. However, slight changes in nanomaterial-polymer chemistry can make the PNC susceptible to failure. Increasing the concentration of nanotubes in polymer can increase the interfacial area, but can also increase the probability of having variability in the nanomaterial-polymer microstructure that makes it vulnerable to failure due to closer contact between materials and therefore increased likelihood of aggregation (116). Stress transfers in PNCs are mainly achieved by three mechanisms; mechanical interlock or adhesion, chemical bonding, and weak van der Waals interaction (117). Mechanical interlock of the polymer chains with the CNTs is not easy when the nanotubes are perfectly smooth and defect free but can be improved by creating defects in the nanotubes. This, however, requires a trade off between maintaining the mechanical properties of the CNT and improving interfacial interaction between the CNT and polymer. Attaching chemical species to the nanomaterials or polymer can lead to a covalent bond between the nanotube and polymer and probably results in the strongest interfacial interactions. Barber et al. estimated interfacial interaction resulting from adhesion by measuring the force required to pull out a single MWNT from polymer (118). They attached the MWNT to an AFM tip, lowered it into polyethylene-butene melt and allowed the polymer to cool and adhere to the nanotube. The nanotube was then pulled out by retracting the z-piezo

and the forces acting on the nanotube were recorded based on the deflection of the AFM cantilever during the process. They found that a stress of approximately 47 MPa was required to pull out the nanotube from the polymer matrix. Computer simulations have estimated the interfacial strength due to van der Waals interaction of a CNT-polyethylene system to be close to 3 MPa, while it is closer to 100 MPa when the CNT and polyethylene are covalently bonded and as high as 160 MPa for CNT-polystyrene system (119,120).

2.9 Characterization

2.9.1 Morphology

Polymer nanocomposite morphology is widely characterized with the aid of microscopy techniques; mainly optical microscopy, scanning electron microscopy (SEM), and transmission electron microscopy (TEM). The presence of nanotubes in a polymer matrix enhances crystallization by providing heterogeneous sites for polymer chain nucleation. Polarized optical microscopy is widely used to observe crystallization. Lee et al. studied crystallization of PP/SWNT nanocomposites using optical microscopy, reproduced in Figure 2.11, and found that the diameter of the polymer spherulites decreased from 400 μm to approximately 20 μm due to the addition of nanotubes (121). Higher concentration of SWNTs was found to further decrease the size of the spherulites owing to the presence of more nucleation sites.

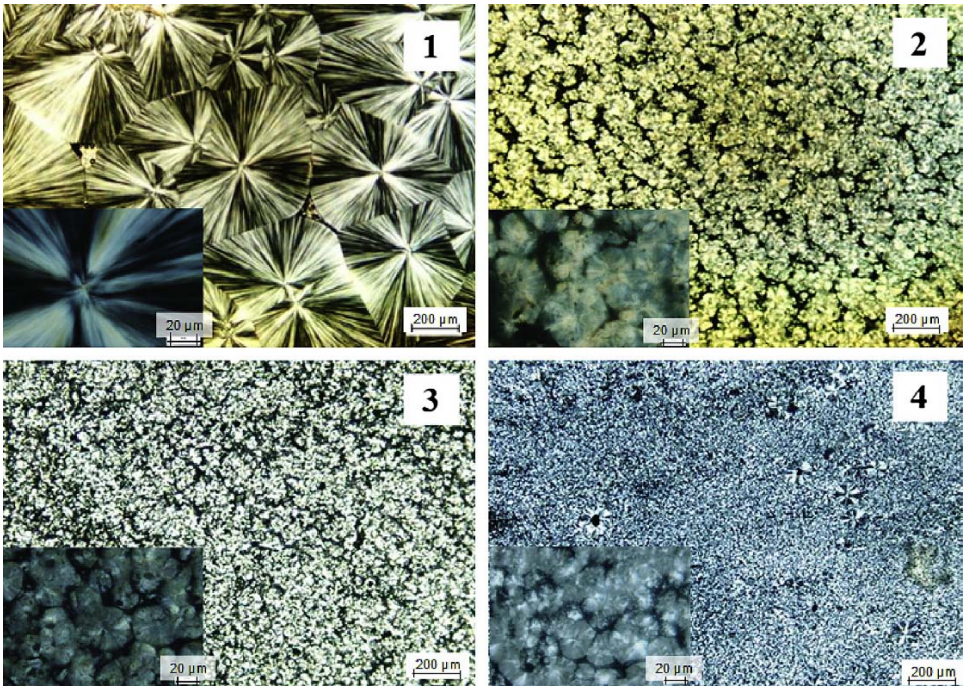

Figure 2.11. Optical micrographs with cross-polarizers (1) PP, (2) PP/SWNT (0.1 % wt.), (3) PP/SWNT (1 % wt.), and (4) PP/MWNT (1 % wt.). Image reproduced from Lee et al. (121).

However, optical microscopy methods are generally incapable of imaging length scales below 0.2 – 0.5 µm, thus significantly limiting their applicability to morphological studies of polymer nanocomposites (122). Consequently, optical microscopy is generally employed to gain insight in to the spherulitic size and geometry during crystallization, and microscale distribution of nanotube aggregates in the polymer matrix. SEM and TEM are more suitable towards investigating nanotube dispersion in polymers as they are not limited by the wavelength of visible light. SEM employs an electron gun to shoot electrons into an evacuated container. A condensing lens focuses the electrons in to a taut beam. A scan coil then directs the electron beam on the surface of the target, and is helped by an objective lens in focusing on a desired location on the specimen. As the

electron beam moves across the specimen, secondary electrons are disengaged from the specimen surface. The secondary electrons are collected and counted by a detector, and the information gained is used to reproduce an image of the specimen surface. SEM is attractive due to the high magnifications (~200kX) and high resolutions ~ 5-10 nm it achieves which can image MWNTs or SWNT bundles. TEM is a more attractive option to image individual nanotubes in a polymer matrix, and has the ability to distinguish between SWNTs and MWNTs, and individuals and bundles. Figure 2.12 shows TEM and SEM images of SWNTs dispersed in polystyrene, and provides a clear depiction of the presence of SWNT bundles in the polymer matrix.

While microscopy techniques are useful for providing direct visualization of the nanocomposite microstructure, a severe limitation is the very limited area they scan particularly at high magnifications. Raman spectroscopy is a technique that can be employed to overcome this limitation in understanding the degree of nanotube dispersion. Raman spectroscopy takes advantage of Raman scattering, also known as inelastic scattering, of photons. When light is shined on a material to achieve excitation, the photons are either elastically or inelastically scattered. In elastic scattering, the scattered photons have the same frequency and wavelength as that of the incident photons, while in inelastic scattering the scattered photons have a frequency that is different from the incident. The variation in the frequency and energy of the inelastically scattered photons give information regarding the structure of the material. SWNTs have several characteristic peaks in their Raman spectra; Figure 2.13 shows a Raman spectrum of SWNTs and identifies the main peaks.

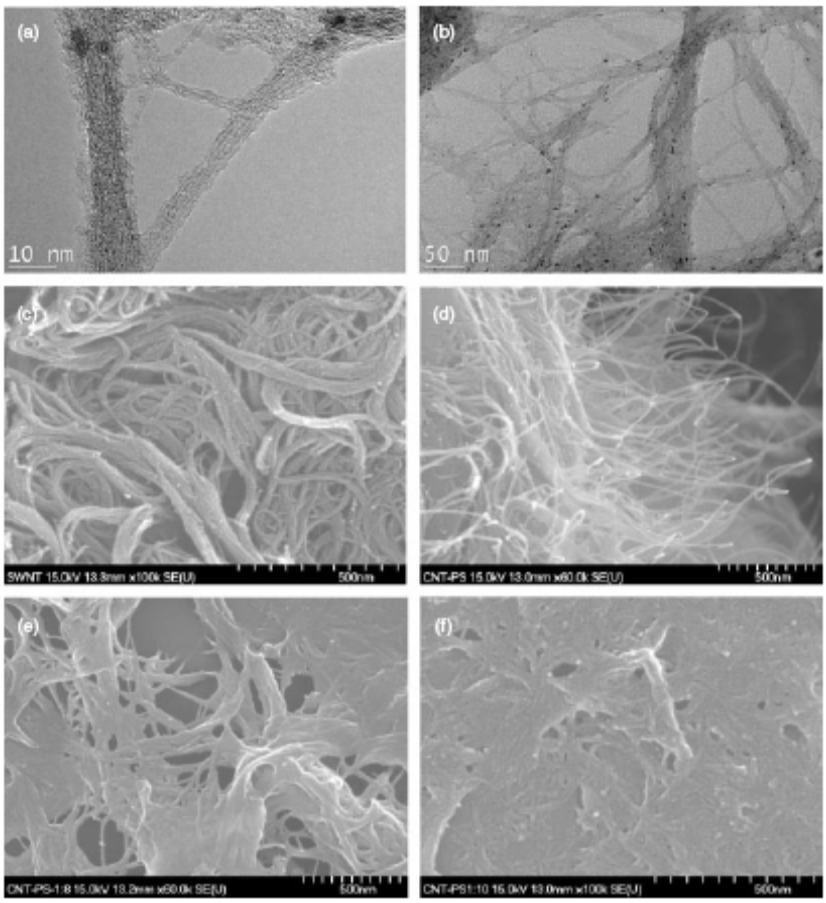

Figure 2.12. (a) and (b) TEM image of polystyrene/SWNT nanocomposite, (c) SEM image of pristine SWNT, (d) SEM image of polystyrene/SWNT powder, (e) and (f) SEM image of PS/SWNT in chloroform. Image reproduced from Shin et al. (123).

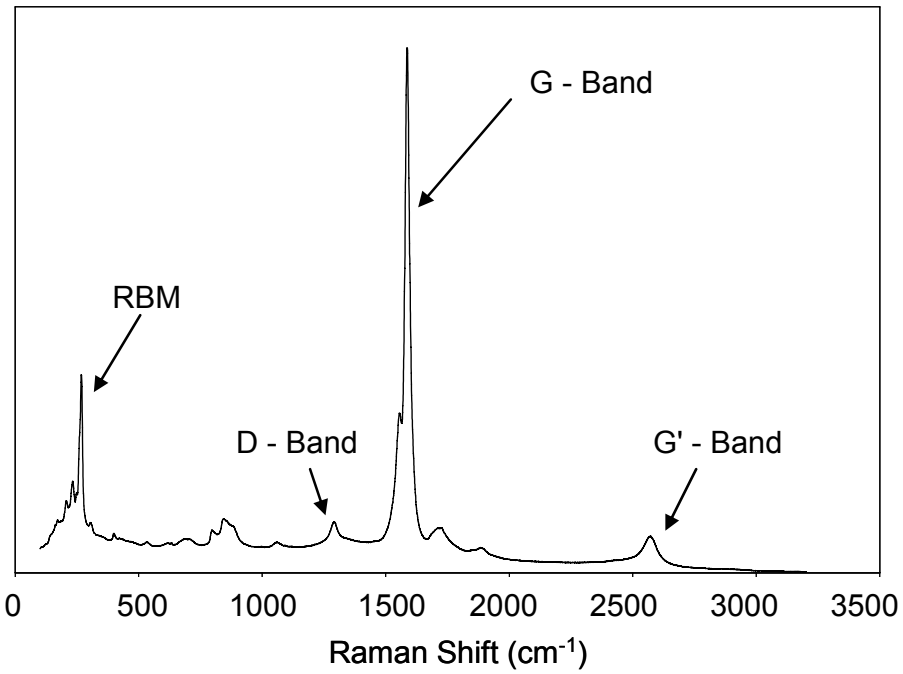

Figure 2.13. Raman spectra of SWNTs.

An important aspect in the Raman spectra of nanotubes are the radial breathing modes (RBMs) as they are unique to carbon nanotubes and are not seen in other carbon materials (124). RBMs are observed in low frequency range, usually 100 – 250 cm^{-1}, and are a result of the radial vibrations as shown in Figure 2.14. The specific RBM frequency provides insight into the diameter of the nanotube according to the relation below:

$$\omega_r = \frac{224}{d} \tag{2.10}$$

where d is the nanotube diameter and ω_r is the frequency (in cm^{-1}) of the RBM. It has been shown that the RBM can be used to estimate the diameter within 1 Å for d = 5.0 nm, and the accuracy increases with decreasing diameter (124).

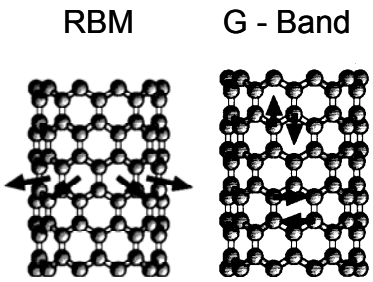

Figure 2.14. The atomic displacements associated with the RBM and G-band normal mode vibrations. Figure reproduced from Dresselhaus et al. (125).

The G-band, also called the tangential modes band, appears around 1585 cm^{-1} and is essentially composed of two stronger peaks owing to the circumferential and axial atomic vibrations (stretching of the carbon atoms), as shown in Figure 2.14. The two peaks are useful in differentiating between metallic and semiconducting nanotubes; the circumferential mode appears at a lower frequency than the axial mode in semiconducting nanotubes while the reverse occurs in metallic nanotubes (124). In addition to depending on the chiral angle, the intensity of the G-band also depends on the concentration of the nanotubes in the scan area, with higher intensity resulting from a higher concentration. The D-band (or disorder induced band) appears at around 1350 cm^{-1} and occurs due to defects in the nanotube wall that break the symmetry of the sp^2 bonded hexagonal lattices of the carbon nanotubes. These defects may show up as the presence of pentagons and heptagons instead of hexagonal lattices in the nanotube structure (Stone-Wales defect), vacancies, presence of functional groups etc. The presence of impurities, such as amorphous carbon, can also result in the D-band. Thus, the more defects, or changes to structure, present in a nanotube, the higher will be its D-band intensity. Since the presence of functional groups that are covalently bonded to the

nanotube increases the D-band intensity, the ratio of the D-band to G-band is widely accepted as a measure of functionalization of nanotubes. Another prominent peak observed in the Raman spectra of carbon nanotubes is the G'-band, occurring at around 2600 cm^{-1}. The G'-band is the second order of the D-band and is understood to depend on the electronic structure of the carbon nanotube. It is used in evaluating interfacial interactions.

As stated above, the G-band intensity is significantly influenced by the concentration of nanotubes in the scan area. Thus, a map of the G-band intensities throughout a large area (length scales of tens of microns) on the nanocomposite surface will provide a direct relation to the nanotube concentration throughout the scan area, thus estimating of the degree of nanotube dispersion. Du et al. probed poly (methyl methacrylate) (PMMA)/SWNT nanocomposites using Raman mapping (Figure 2.15) and found it to be a very effective tool to estimate the degree of nanotube distribution (126). The Raman map of the nanocomposite fabricated using wet SWNTs (Figure 2.15a) was flat; the nanotubes were uniformly distributed throughout the bulk composite. The standard deviation in the G-band intensities was also low. The Raman map of the nanocomposite fabricated using dry SWNTs contained many peaks (Figure 2.15c), indicating that certain parts of the scanned area contained higher concentrations of SWNTs and therefore the SWNT dispersion was not uniform throughout the nanocomposite. The standard deviation in the G-band intensities was calculated to be significantly larger than that obtained in the better distributed nanocomposites. Thus, Raman mapping can be used as an efficient and effective tool to characterize nanotube distribution through large volumes of nanocomposites.

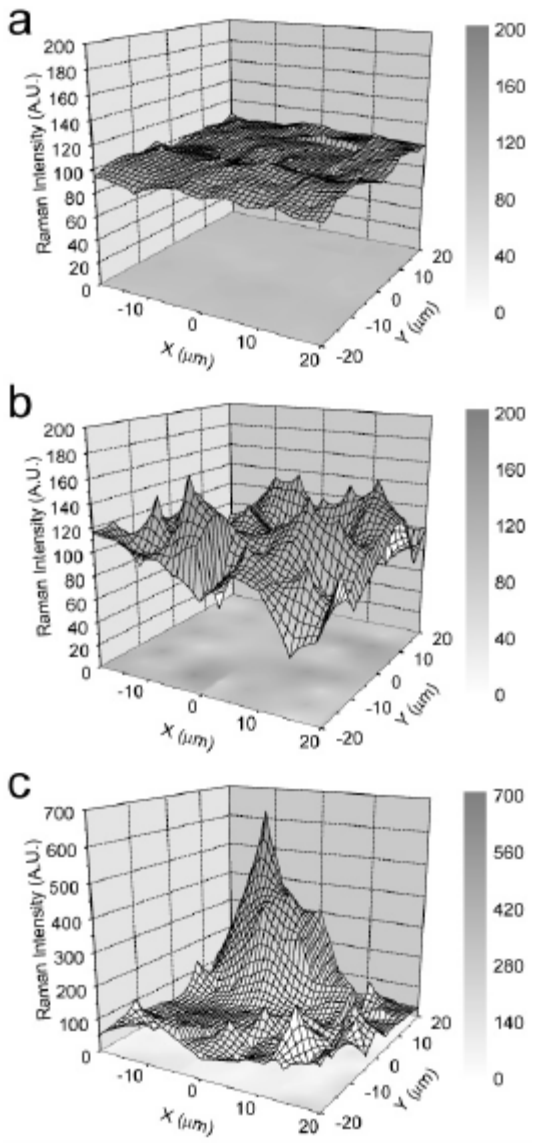

Figure 2.15. Raman maps (40 x 40 μm^2) of (a) wet SWNT 1 % wt., (b) equal parts dry and wet SWNT 1% Wt., and (c) dry SWNT 1% wt. in PMMA nanocomposite. Image reproduced from Du et al. (126).

2.9.2 Rheology

Microscopy methods to characterize nanocomposites are useful in visualizing the dispersion of nanotubes in a polymer matrix. However, as previously mentioned, a severe limitation of these methods is that they only scan very limited areas of the nanocomposite. Raman mapping, while providing insight into the dispersion status of a larger volume, is only capable of probing a volume thickness that can be penetrated by the laser. Thus, the aforementioned techniques of characterizing nanocomposite dispersion, while providing a vast amount of information, are quite limited in their range. Rheology is a technique that can be employed to gain significant knowledge into the microstructure of bulk nanocomposites, while also providing information regarding the flow behavior of the samples. Rheometers are widely used to study the microstructure and flow behaviors of many materials including polymers, suspensions, and lubricants.

A rotational rheometer typically consists of a bottom plate and a top plate or cone measuring system. The attached fixture is referred to as a parallel plate or a cone and plate depending on whether the top attachment is a plate or a cone. The sample is loaded between the two plates and any excess is trimmed to form a flat edge. One fixture is rotated at a desired rate to apply the necessary steady or dynamic shear on the sample, and the torque and normal forces generated are measured. Rheological properties can be calculated from the knowledge of the shear applied, torque generated, gap between fixtures, and fixture geometry. Rheological characterization on the polymer nanocomposites in this research were conducted on an Anton Paar MCR 301 rotational rheometer under strain control using a 25 mm parallel plate geometry. A schematic of

the parallel plate fixture is shown in Figure 2.16. The shear stress and shear rate on a parallel plate are calculated as:

$$\tau(R) = \frac{2M}{\pi R^3} \tag{2.11}$$

$$\dot{\gamma}(R) = \frac{\omega R}{h} \tag{2.12}$$

Where

$\dot{\gamma}$ = Shear rate (1/s)

τ = Shear stress (Pa)

M = Torque (N.m)

R = Radius of measuring plate (m)

h = gap between plates (m)

ω = Rotational speed (s^{-1})

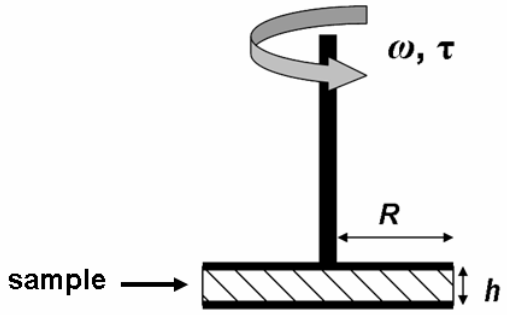

Figure 2.16. Parallel plate geometry.

The microstructure of the polymer nanocomposites are typically probed by running dynamic tests on samples wherein they are subjected to an oscillatory shear of

constant amplitude within the linear viscoelastic region. The response of the sample obtained at high frequencies relates to the behavior of the sample at short time intervals while that obtained at low frequencies corresponds to the sample behavior at long time intervals. When an oscillating strain (sinusoidal wave) is applied on the sample, the resulting stress will also oscillate at the same frequency but with a phase lag of angle δ with respect to strain. Such data can be resolved into two components; a solid-like component (storage modulus G′) that is in phase with the input and a liquid-like component (loss modulus G″) that is out of phase with the input. Any time a shear is applied on a material, a portion of the shear energy applied is stored within the sample, allowing the material to regain its structure when the shear is removed, while the rest of the energy is lost as heat. The energy that is stored within the sample is known as storage or elastic modulus, and the energy that is lost is known as loss or viscous modulus. The constitutive equations for G′ and G″ are given below:

$$G' = \left(\frac{\tau}{\gamma}\right)\cos(\delta) \tag{2.13}$$

$$G'' = \left(\frac{\tau}{\gamma}\right)\sin(\delta) \tag{2.14}$$

Where,

γ = Shear strain (%)

δ = Phase angle

Some other important frequency dependent rheological functions are

$$\text{Complex modulus, } G^* = \frac{\tau(t)}{\gamma(t)} = \sqrt{G'^2 + G''^2} \tag{2.15}$$

$$\text{Complex viscosity, } \eta^* = \frac{\tau(t)}{\dot{\gamma}(t)} = \left[(\eta') + \left(\frac{G'}{\omega^2} \right) \right]^{\frac{1}{2}} \tag{2.16}$$

Complex modulus G^* defines the total resistance to deformation of a material under the applied shear strain. Alternatively complex viscosity η^* can be used to define the total resistance to a dynamic shear rate. Besides applying rheology to study the behavior of the material with respect to time and shear, it can also be applied to predict the formation of an interconnected nanotube network within the polymer matrix. Rheological percolation is identified by the formation of a plateau in G′ at low frequencies in dynamic tests resulting from an apparent yield stress (122,127). Theoretical calculations, using Equation 2.17, predict rheological percolation in PNCs containing SWNTs of aspect ratio 700 (assuming diameter of 1 nm and length of 700 nm) is achieved at a critical volume fraction ϕ_c between 0.001 and 0.002 (128).

$$1 - \exp\left(-\frac{1.4V}{\langle V_e \rangle} \right) \leq \phi_c \leq 1 - \exp\left(-\frac{2.8V}{\langle V_e \rangle} \right) \tag{2.17}$$

Where,

V = volume of capped cylinder

V_e = average excluded volume

It should be noted that aggregation into larger bundle sizes can significantly decrease the aspect ratio and therefore result in percolation being observed at concentrations markedly higher than that predicted for individually dispersed nanotubes.

Figure 2.17 shows a typical G′, G″, and η^* response of polypropylene as a function of angular frequency. PP displays typical polymer low frequency terminal region behavior with a slope of G′ ~ 2 and G″ ~ 1, and significantly higher G″ values

compared to G′, thus indicating viscous behavior domination. The addition of nanotubes tends to drastically alter the rheological behavior of polymers.

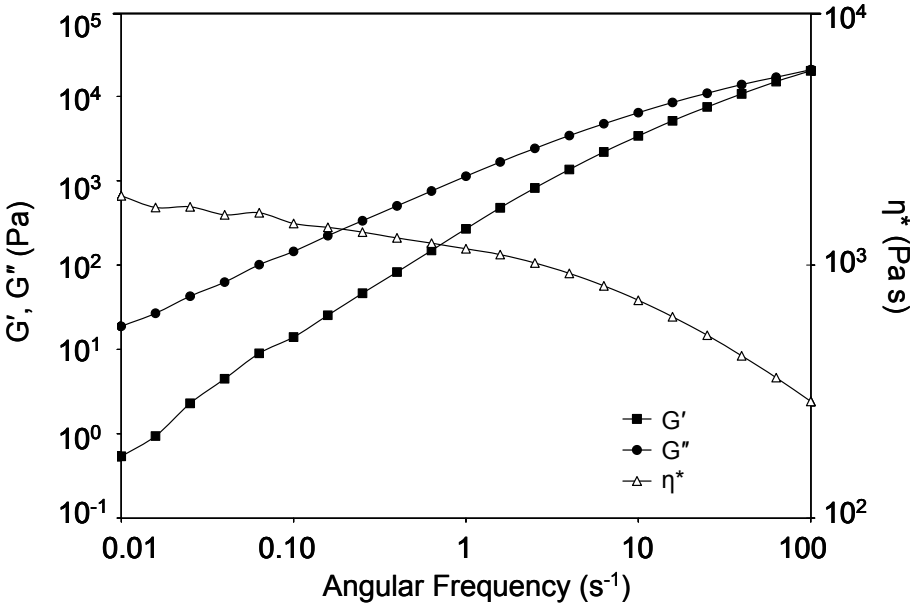

Figure 2.17. Storage modulus, loss modulus, and complex viscosity of polypropylene as a function of angular frequency at temperature T = 200 ^{o}C and strain of 5 %.

Figure 2.18 shows the variation in G′ and G″ behavior of PP incorporated with MWNTs. A large increase in G′ was observed with the addition of a small amount (~ 2-3 wt %) of MWNTs; a relatively smaller increase was observed in G″. On further increasing the concentration of MWNTs, the nanotube-nanotube interaction began to increase, and G′ was less dependent on frequency and tends to plateau. As stated earlier, this is a result of the interconnected MWNT network in the polymer composite that prevents the polymer chains from relaxing, and appears due to an apparent yield stress. The deviation in the terminal region behavior of the polymer is also attributed to the inability of the polymer chain relaxation due to the interconnected network. The increase

in G′ translates to a corresponding increase in complex viscosity, η^*, as shown in Figure 2.19.

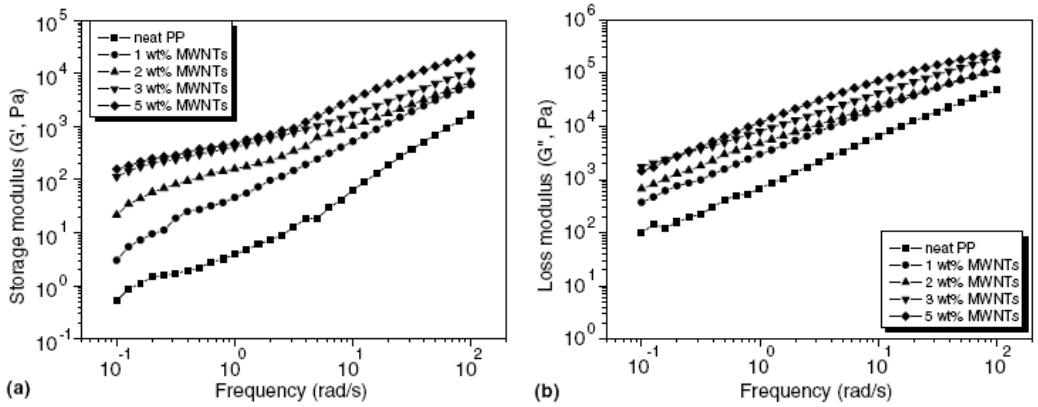

Figure 2.18. Storage modulus (a) and loss modulus (b) of PP/MWNTs. Image reproduced from Seo et al. (129).

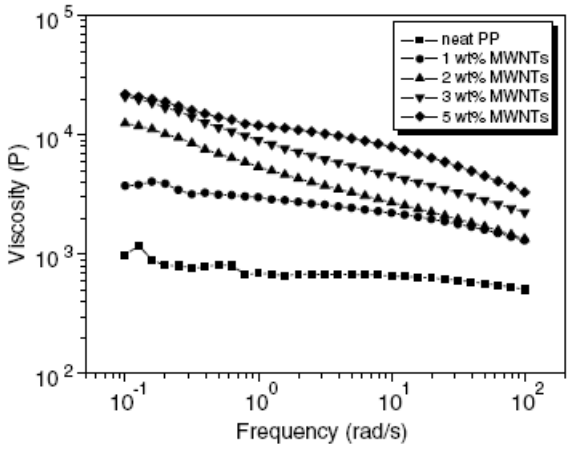

Figure 2.19. Complex viscosity of PP/MWNT as a function of frequency. Image reproduced from Seo et al. (129).

Zhang et al. achieved rheological percolation at 1 vol. % (1.5 wt. %) in SWNT - high density polyethylene (HDPE) nanocomposites by spraying a suspension of SWNTs

on the surface of the polymer powder, followed by melt extrusion at 160 ^{o}C and 50 rpm for 20 min (77). They also investigated the electrical percolation of their nanocomposites and estimated the electrical percolation threshold at 2.7 vol. % (4 wt. %). The difference in the electrical and rheological percolation is attributed to the fact that electrical conductivity in the nanocomposite is due to the mechanism of electron hopping, thus the required tube-tube distance has to be ~ 5 nm or lower for the composite to be electrically conductive. Rheological percolation can be achieved as long as the tube-tube distance is small enough to prevent polymer chain motion. If the polymer has a high molar mass then the diameter of the random coiled polymer chain will be larger than that of a polymer of low molar mass; hence requiring a lower concentration of nanotubes to reach rheological percolation. In the study by Zhang et al. the diameter of the HDPE polymer random chain coil was more than 10 nm, and therefore reached rheological percolation before reaching electrical percolation.

McNally et al. employed rheology to investigate the interfacial interactions and nanotube network complexities in polyethylene/MWNT nanocomposites (130). They investigated the damping behavior of nanocomposites by studying the relationship between tan δ (the ratio of loss modulus to storage modulus) and frequency, as shown in Figure 2.20. They observed a decrease in tan δ and progressively flatter curves at lower frequencies with increased addition of MWNTs; indicating the presence of interfacial interactions between PE and the nanotubes. Further evidence of the complexity of the nanotube networks in the polymer matrix was obtained by studying the Cole-Cole plot; a plot G′ against G″ as shown in Figure 2.21. For any given loss modulus value, the plot showed an increase in the storage modulus values and a decrease in the slope of the curve as the nanotube

concentration increased, indicating a change in the structure of the nanocomposite owing to the complex nanotube network attained at higher concentration.

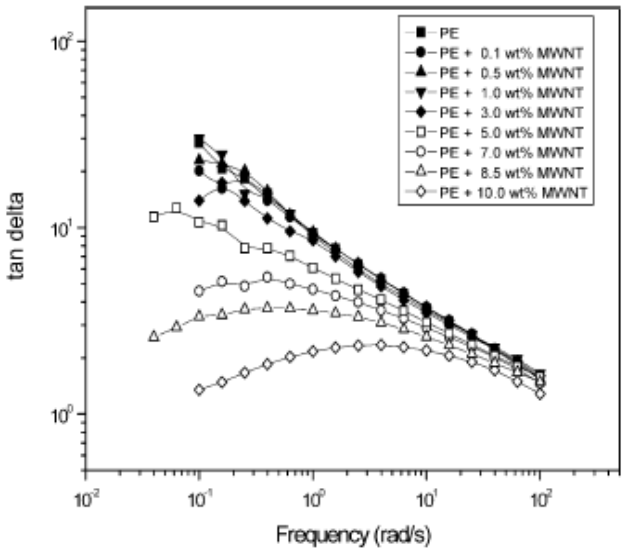

Figure 2.20. The value of tan δ as a function of frequency in PE/MWNT nanocomposites. Image reproduced from McNally et al. (130).

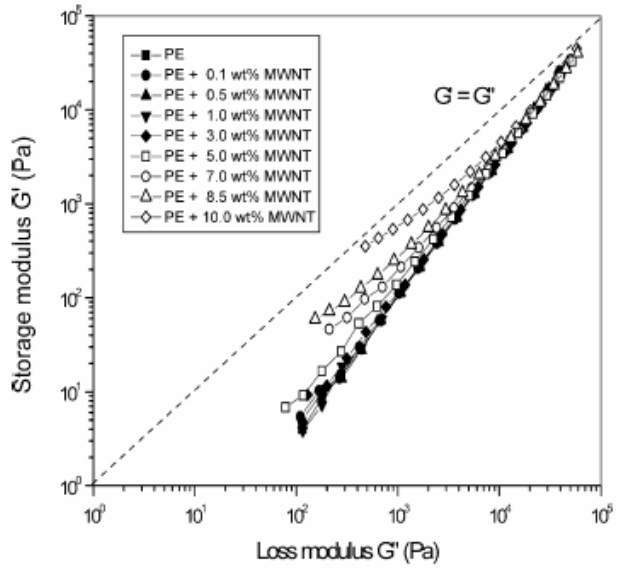

Figure 2.21. Storage modulus (G′) as a function of Loss modulus (G″) in PE/MWNT nanocomposites. Image reproduced from McNally et al. (130).

Kharchenko et al. investigated the normal forces and found negative normal stress differences in PP/MWNT nanocomposites, a rarity in soft condensed matter (127). Normal forces, arise from the stretching and alignment of nanotubes in the matrix, and are an estimate of the stored elastic energy during flow. These forces are most noticeable in examples such as rod climbing (where the fluid climbs up a rotating stir rod) and die swell (expansion of the polymer on exiting a die). Typically, under shear, polymer chains tend to align and stretch. On the removal of shear and allowing to relax (such as when exiting a die) the polymer chains tend to vent the shear stresses stored within as a means to achieve their relaxed coiled state. This is usually manifested as an outward push; and in a two plate model where the top plate rotates, this is observed as a thrust acting to push the two plates apart and corresponds to a positive normal force. In polymer nanocomposites, a positive normal force is usually observed at nanotube concentrations below the percolation threshold where the polymer matrix dictates the composites' rheological behavior. However, on further increase in the nanotube concentration to values greater than the percolation threshold, large and negative normal forces are observed. Figure 2.22 shows effect of MWNTs on the normal forces in PP/MWNT nanocomposites. The authors attributed the large negative normal forces to the large scale deformation of the nanotube network and nanotube deformation on a local scale resulting from a rotational deformation of the CNT network. A qualitative model explaining the large negative normal forces were proposed by the authors where high aspect ratio nanotubes, in the nanotube network in the polymer matrix, bend rather than extend. The authors proposed that the fibrous 'struts' of the interconnected nanotubes networks rotate about their junction points rather than extend, such as the links of a

deformed chain link fence; a cartoon depicting the behavior is shown in Figure 2.23 (131). Since the CNTs are much stiffer than the polymer chains, the deformed interpenetrating CNT network within the viscous polymer matrix dominates the low-frequency viscoelastic response of the nanocomposite. At low nanotube concentrations, the lack of a nanotube network implies an absence of negative normal stresses.

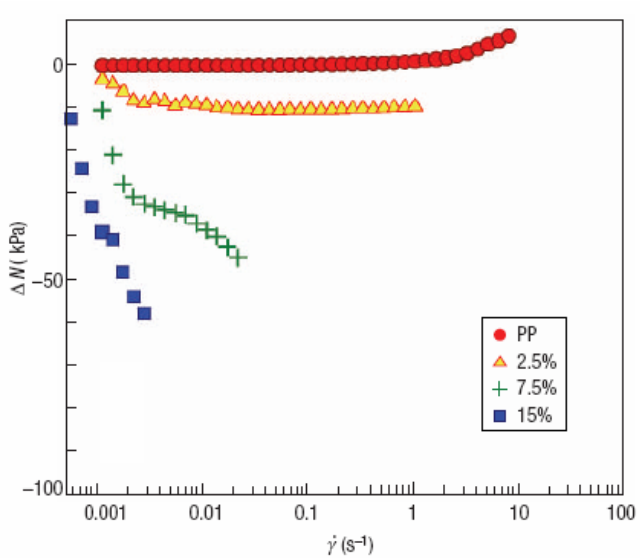

Figure 2.22. Effect of MWNT content on the normal force measurement. Image reproduced from Kharchenko et al. (127).

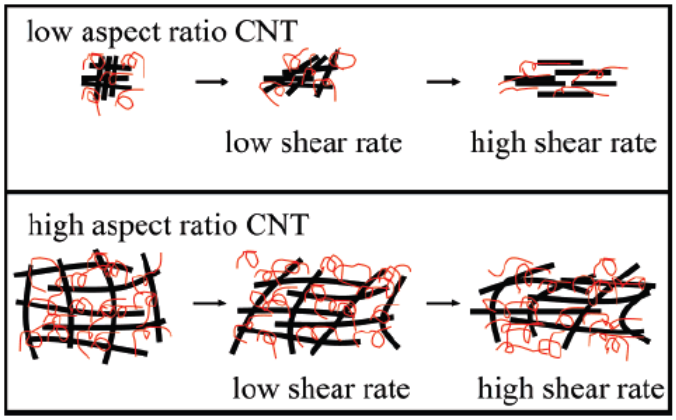

Figure 2.23. Models about deformation of low aspect ratio PP/CNT and high aspect ratio PP/CNT networks under steady shear. Image reproduced from Xu et al. (131).

2.9.3 Thermal Analysis

The excellent thermal properties of carbon nanotubes, including their high thermal conductivity and high temperature stability, render them as ideal reinforcement materials to improve the thermal properties of polymers. In general, the incorporation of carbon nanotubes in polymer matrices is expected to result in an increase in glass transition temperature, crystallization temperature, melt temperature, and decomposition temperature. Differential scanning calorimetry (DSC) is widely used tool to study phase transitions, including crystallization and melting of materials. The device consists of two heaters which are loaded with sealed pans (a sample pan containing the polymer and an empty reference pan). The two pans are heated at the same rate, usually 10 ^{o}C/min, with high precision. A computer records the heat input to the pans required to maintain the specified heat rate. The melting temperature is observed as in sharp increase in the heat flow to the sample pan owing to the latent heat of melting of the polymer. On the contrary, energy is released during crystallization, thus the crystallization temperature is marked by a sharp decrease in the heat flow to the sample pan.

Polymer crystallization occurs by a process referred to as nucleation. Nucleation can be thought of as the birth and growth of the crystals. In fact, nucleation is sub-divided in to primary and secondary nucleation. The crystallite nuclei are formed, due to variations in the solution order or density, during primary nucleation; and they grow in size by further induction of polymer chains during secondary nucleation. Primary nucleation can occur in two ways. If there is no surface for the polymer chains to form nuclei on, then the only option for nucleation is super-cooling the solution to enable spontaneous nucleation of the polymer crystals; referred to as homogeneous nucleation.

In most cases, referred to as heterogeneous nucleation, the polymer solution is added with some seed polymer thus providing it with some surface to allow primary nucleation. The addition of carbon nanotubes to a polymer melt results in the presence of numerous polymer crystallite nucleation sites, consequently influencing the crystalline structure, crystallization temperature and kinetics of the composite. The better the dispersion of the nanotubes in the polymer matrix, the greater the number of available nucleation sites and the more significant the influence a given loading of nanotubes has on polymer crystallization. Bhattacharya et al. found that SWNTs, even with poor dispersion, act as nucleating agents for PP crystallization and influence the kinetics (132). It was reported that the PP crystallization rate with 0.8 wt. % SWNT was much faster than for neat PP. The nanocomposite also displayed over 10 ^{o}C increase in the crystallization temperature. In addition, the authors noted that the crystallization peak of the PP nanocomposite was narrower compared to that of neat PP indicating a narrow size distribution of the crystallites. Valentini et al. observed a considerable influence of SWNTs on PP crystallization kinetics (133), demonstrated by a marked decrease in the crystallization half-time of PP as well as a noticeable increase in the general crystallization rate. The crystallization half-time of PP was estimated to decrease from 840 s to 115 s by the addition of 5 wt. % SWNTs. The Avrami analysis is generally employed to understand the bulk crystallization kinetics of polymer using the Avrami equation reproduced below (134).

$$1 - X_t = \exp\left[-k(t)^n\right] \tag{2.18}$$

which can be rewritten as

$$\ln\left[-\ln(1 - X_t)\right] = n \ln t + \ln k \tag{2.19}$$

where X_t is the relative crystallinity at time t, k is the bulk crystallization constant which depends on the shape, amount, and type of the crystallites, and n is the Avrami exponent which depends on the nucleation type and the growth geometry but not on the amount of nucleation. The Avrami exponent and the bulk crystallization constants are obtained as the slope and intercept by plotting $\ln[-\ln(1-X_t)]$ versus $\ln(t)$. The crystallization half time $t_{1/2}$, or time to attain 50 % relative crystallinity, can be obtained by reducing Equation 2 to $t_{1/2} = (0.693k)^{1/n}$. The information obtained from the Avrami analysis can be further used in the Arrhenius equation to estimate the activation energy required for crystallization:

$$\frac{1}{n}(\ln k) = \ln k_o - \frac{\Delta E_{ac}}{RT_c} \tag{2.20}$$

where, k_o is the pre-exponential factor, ΔE_{ac} is the activation energy for crystallization, and R is the universal gas constant. Kim et al. observed that the ΔE_{ac} of poly(ethylene 2,6-naphthalate) (PEN) decreased by the addition of MWNT nanocomposites, and attributed this decrease to the ability of MWNTs to act as PEN crystal nucleation sites leading to improved kinetics (135). The investigations by Yuan et al. showed similar decrease in the crystallization activation energy of PP with the addition of carbon black (136). In contrast to the results obtained by Kim et al. and Yuan et al., Leelapornpisit et al. observed marked increase in the crystallization activation energy PP, from 208 kJ/mol to 243 kJ/mol with the addition of 0.25 wt % SWNTs (137). This is surprising considering that the presence of nanotubes in polymers tend to increase the crystallization rates and decrease the activation energy for crystallization. The authors attributed the increase in activation energy with the addition of SWNTs to PP to the increased viscosity

of the nanocomposite. It was argued that the presence of the SWNTs in PP resulted in an increased viscosity that hindered the rearrangement of the PP macromolecule segments and thus required higher energies to enable crystallization. However, the authors also noted that the activation energy decreases as the degree of crystallization increases, indicating that the activation energy is more strongly related to the beginning of the nucleation process (primary nucleation) than the growth process (secondary nucleation). If this holds true, the activation energy of crystallization should decrease with the addition of the nanotubes since the presence of nanotubes in the matrix enhances the polymer crystallite nucleation process. It has to be understood that the crystallization activation energy is a result of a complex interplay between factors favoring crystallization, such as the presence of nucleation sites, and factors inhibiting crystallization, such as high matrix viscosities.

In summary, there has always been demand for high performance-low cost polymer composites. CNTs and VGCFs should, theoretically, offer good reinforcement to the polymer backbone when added to the composites because of their large surface areas and high mechanical strength. However, the nanocomposites fabricated to date have mostly displayed poor or inconsistent properties. The properties of polymer nanocomposites depend on many factors including the type of nanomaterial used, purity of the nanomaterial, aspect ratios, interfacial adhesion between the nanomaterials and the polymer matrix, and most importantly the dispersion of the nanomaterials in the matrix. As the research stands now, dispersion and interfacial interaction are still major obstacles in fabricating good polymer nanocomposites. The attractive forces between carbon nanotubes are difficult overcome without harming the polymer or the nanotubes

themselves. Functionalization of nanotubes may provide a reasonably good solution to this issue but at the cost of compromising on some properties of the nanotubes. Many methods that employ mechanical force, solvent intercalation and chemical functionalization to process nanocomposites have been generated; however the resulting nanocomposite properties have failed to meet expectations in the majority of cases. It is uncertain if this is due to the processing conditions employed or the chemical incompatibility between the polymers and the nanomaterials. To date, researchers have mostly focused on either the effects of chemical modifications of the nanotubes or polymer alone, or processing conditions on the properties of the resulting nanocomposites while largely overlooking the interrelationships between structures, processing, and properties. Consequently, an understanding of the structure-processing-properties interrelationships of polymer nanocomposites is very important is deciding the future course of action in building these amazing materials with incredible potential. This research will employ statistical design of experiments (DOE) to study the effects of processing conditions and structure of nanomaterials on the properties of melt extruded polypropylene (PP) containing VGCFs, SWNTs, and SWNTs covalently functionalized with alkyl groups.

Chapter 3

Experimental Section

3.1 Materials

Three batches of SWNTs (density = 1.45 g/cm^3) were used in this research; (i) SWNTs produced by HiPco (50) process, having a purity of approximately 95 % and a rheology average aspect ratio (length to diameter ratio) of approximately 700, were obtained from the Richard E. Smalley Institute for Nanoscale Science and Nanotechnology (Houston, TX), (ii) SWNTs produced by HiPco process, having a purity of approximately 90 % and an aspect ratio of approximately 600 were obtained from Unidym, Inc. (Menlo Park, CA), and (iii) SWNTs produced by the CoMoCat process (51), having a purity of 90 % and aspect ratio of 1000 were obtained from SouthWest NanoTechnologies (Norman, OK). Pyrograf III PR-19 VGCF (density = 1.95 g/cm^3) having diameters of 100 - 200 nm and aspect ratios of 300 - 500 was obtained from Applied Sciences Inc (Cedarville, OH). Polypropylene (PP) (density = 0.9 g/cm^3) used in this research was obtained as pellets (Melt Flow Index = 12, M_n = 63000) from Sigma Aldrich (St. Louis, MO) or as flakes (Melt Flow Index = 12) from Total Petrochemicals (Houston, TX). Initial investigations showed that the as received PP had a relatively low degree of thermal and oxidative stability. Therefore, 2500 ppm of Irganox HP 22155 FF stabilizer, obtained from Ciba Specialty Chemicals (Tarrytown, NY) was dry blended with PP to produce composites with enhanced thermal stability. HP 2215 FF contained both the primary and

secondary antioxidant. The primary antioxidant was a phenolic OH group that worked as a free radical scavenger and prevented oxidation. The secondary antioxidant reacted with any hydroperoxides formed during oxidation and converted them to non radical products. All reference information for pure PP was based on measurements of the resulting stabilized blends.

To study the effect of surface chemistry on properties, a portion of the SWNTS were functionalized with dodecyl ($C_{12}H_{25}$) groups using the reductive alkylation method (113) and chemicals obtained from Sigma Aldrich. The experimental setup, shown in Figure 3.1, consisted of a three-necked round bottom flask with a condenser attached on top. One arm of the three-necked flask was connected to argon gas and the other was

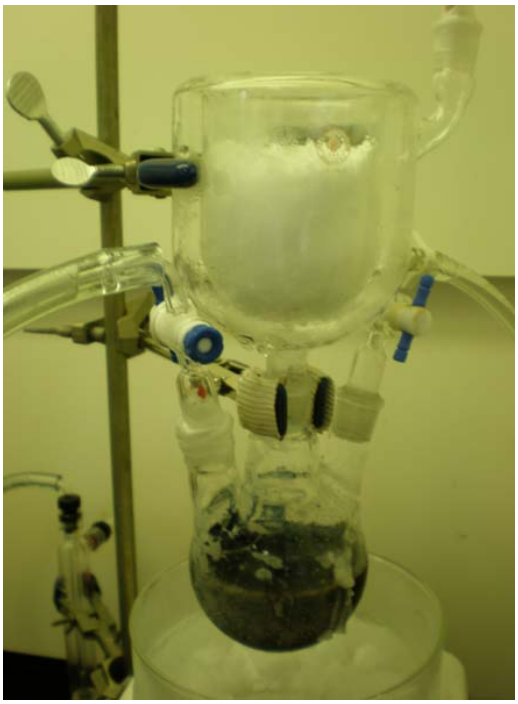

Figure 3.1. Functionalization experimental setup.

connected to a bubbler. The experimental setup was cleaned in a base bath and deionized water, dried in a vacuum oven at 100 ^{o}C, flame dried after set up, and allowed to cool under vacuum. The round bottom flask was purged with argon to create an inert blanket, filled with 20 mg of dry SWNTs (vacuum dried overnight at 100 ^{o}C), and purged again with argon. Dry ice was added to the top condenser and the bottom bath, and wetted with acetone to promote good heat transfer. Argon flow to the round bottom flask was turned off and ammonia gas was allowed to pass through the condenser till about 60 ml of ammonia condensed into the round bottom flask. Ammonia was then turned off and argon was allowed to flow though the flask again. 231 mg lithium was added to the flask through the argon arm and the contents stirred for 10-15 minutes. Lithium, in liquid ammonia, donated its valence electron which is solvated by a part of ammonia, while the other part of ammonia formed a ligand with the lithium ion. The intercalation of the nanotubes by the ligated lithium led to the debundling of the nanotubes. Next, 1.58 ml of 1-iodododecane was added to the solution and argon gas was turned off. The alkyl halide immediately dissociated into halide anion and alkyl radicals. The alkyl group readily attached to the nanotube while the halide group reacted with lithium to form lithium iodide as shown in Figure 3.2.

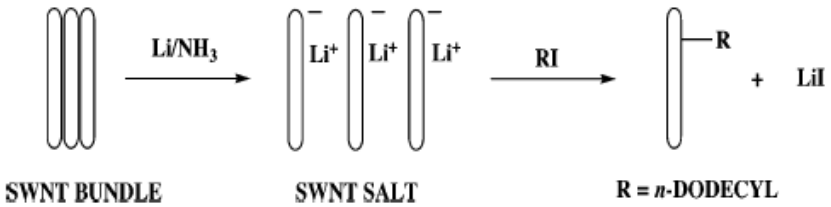

Figure 3.2. Reductive alkylation functionalization mechanism. Image reproduced from Liang et al. (113).

The mixture was allowed to react for 4-5 hours, followed by the addition of 10 ml methanol to terminate the reaction. This was followed by the addition of 20 ml deionized water and 3-4 ml of 10 vol. % HCl. The contents were transferred to a separation funnel and washed with DI water and hexane. The aqueous layer was drained, and the funnel replenished with DI water and washed again. This process was repeated four times and the contents filtered through 0.2 μm PTFE filter paper. The nanotubes were collected from the filter paper and suspended into a vial containing ethanol. The vial was bath sonicated for 10 seconds and its contents transferred to a separating funnel. The nanotubes were washed with ethanol and water four times, vacuum filtered and the above steps were repeated with hexane and then ethanol to ensure complete removal of ammonia and any trace metals. The washed and filtered nanotubes were allowed to dry overnight under ambient conditions, followed by drying in a vacuum oven at 100 ^{o}C for 24 h.

3.2 Design of Experiments

Stat-Ease Design-Expert 7.0 was used to generate the sequence of experimental runs and to analyze the results. The factors examined are elaborated in the following chapters. A randomized cubic D-Optimal design including centre points and replicates was used in order to detect interactions while minimizing the number of runs required. A cubic D-Optimal design has advantages over a full factorial design in that it requires fewer experimental runs and thus saves resources and time. The upper and lower levels of the factors studied were specified; the actual numbers used in the experiments are listed in later chapters. The experimental runs were randomized to isolate any effects that might

creep in due to environmental instabilities or any other factors beyond user control and some of the runs were repeated to differentiate real effect from noise. The measured response variables studied are specified in later chapters.

3.3 Processing

The nanocomposites were produced in a two step process. The first step was an initial mixing process where the polymer pellets and nanomaterials were combined together; the mixing processes will be further explained in the sections below. In the second step, the product from initial mixing was melt extruded in a Haake Minilab counter rotating twin screw extruder at extrusion conditions determined by the experimental design. The layout of the twin screw extruder is shown in Figure 3.3 below.

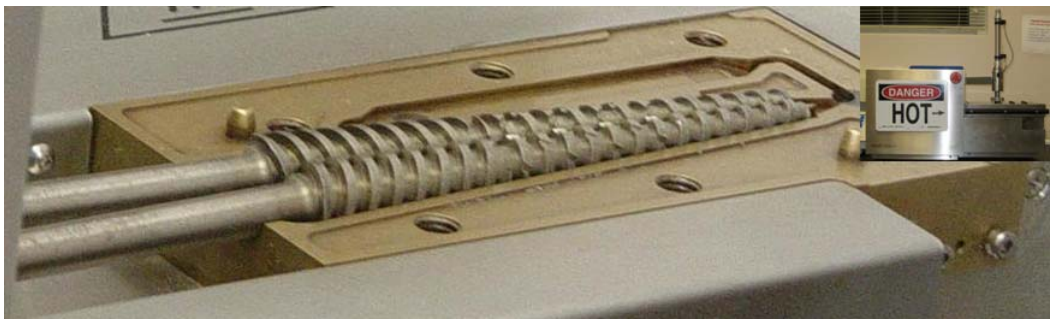

Figure 3.3. Haake Minilab twin screw extruder.

The extruder contains a barrel encasing the counter-rotating screws. The barrel is heated to the desired temperature and the screws are set to rotate at a predetermined speed. The combined action of the high temperature and the shear produced by the rotating screws melts the polymer, breaks apart the nanomaterial aggregates, and distributes the nanomaterials in the polymer matrix as the materials flow down the barrel.

As stated earlier, the advantage of using the Minilab extruder is that it requires a very low volume of materials (~ 5 cm^3) and the availability of a backchannel allows for the material recirculation through the barrel until the desired level of mixing is achieved.

3.3.1 Influence of Initial Mixing Methods on Melt Extruded Single-Walled Carbon Nanotube – Polypropylene Nanocomposites

The materials used in this investigation were Total Polymers isotactic polypropylene flakes, Irganox HP 22155 FF, and HiPco SWNTs from Unidym, Inc. The SWNTs were reacted with 1-iododododecane to result in SWNTs sidewall functionalized with dodecyl chains (C12SWNTs). The functionalization was performed in 60 mg batches; these batches were blended together to eliminate the chances of variations in functionalization batches influencing composite properties.

All composites were prepared at a concentration of 0.5 vol. % (0.8 wt. %). This value was chosen based on the anticipated ability to achieve percolation for composites in which the SWNTs existed as small bundles. Post-processing SWNT aspect ratios, as established from AFM analysis, were in the range of 200 – 400; for this range of aspect ratios the critical volume fraction for percolation is achieved at a $0.0035 < \phi_c < 0.007$ (128). A concentration of 0.5 vol. % was therefore considered high enough to allow for some bundle formation and non-uniformities without being such a high concentration that the SWNTs bundles would be too closely packed as to facilitate reaggregation. The SWNTs were blended with PP by the dry mixing, rotary evaporation or hot coagulation methods described below. The resulting mixture was then blended with the antioxidant and extruded in a Haake Minilab counter-rotating twin screw extruder at 190 ^oC, and 10

rpm, for 10 minutes. PP with antioxidant was processed using each of the initial mixing methods below without nanotube addition and then extruded at the same extrusion conditions to provide reference data.

Dry Mixing (DM): The nanotubes were vacuum dried overnight at 120 ^{o}C. Then, 0.5 vol. % SWNTs or C12SWNTs was mixed with PP by placing PP and the nanotubes in a vial and shaking for one minute prior to feeding into the extruder.

Rotary Evaporation (RE): SWNTs or C12SWNTs were dispersed in ~99 % isopropanol (IPA) at a concentration of 2 mg/ml with the aid of bath sonication. AFM was used to determine the sonication time required to result in similar average aspect ratios for the dispersed SWNTs and C12SWNTs. Due to increased solvent compatibility and steric hindrance, the C12SWNTs were dispersed in the IPA to an average bundle diameter of 2.0 nm, standard deviation of 1.3 nm, and an aspect ratio of 200 - 400 after 1 hour of bath sonication at room temperature. For SWNTs, bath sonication for 6 hours at room temperature resulted in an average bundle diameter of 2.7 nm, standard deviation of 2.4, and aspect ratio of 200 - 400. After sonication, the nanotube dispersion was mixed with PP using magnetic stirring for 10 minutes. The solvent was extracted using a rotary evaporator over 30 minutes at a temperature of 60 ^{o}C and a pressure of 0.4 bar. This method is similar to that of Zhang et al (2006) but provides the advantage that the continuous tumbling of the materials in the rotary evaporator enables what qualitatively appears to be very even nanotube coating on the entire polymer surface (138). To further assure complete solvent removal, the nanotube coated PP was vacuum dried overnight at 120 ^{o}C to result in an initial mixture of 0.5 vol. % PP/SWNT or PP/C12SWNT.

Hot coagulation (HC): The method developed by the Winey group, (68,139) was used with slight modifications to the concentrations used. PP was dissolved in DCB at 120 ^{o}C at a concentration of 30 mg/ml, and the nanotubes were sonicated in DCB at a concentration of 2 mg/ml at room temperature. AFM analysis of 100 nanotubes/bundles per sample showed that a sonication time of 1 hour for C12SWNTs and 6 hours for SWNTs resulted in aspect ratios between 200 – 400. The average bundle diameters were 1.9 nm and 2.5 nm, with standard deviations of 1.5 nm and 2.4 nm for the C12SWNTs and SWNTs respectively. After sonication, the temperature of the nanotube/DCB suspension was increased to 120 ^{o}C and the PP/DCB solution was added to it. This suspension was further sonicated for 5 minutes and then cooled to let the polymer crystallize. The cooled product was then vacuum filtered through a 0.2 μm Millipore PTFE filter and vacuum dried overnight at 120 ^{o}C to obtain the 0.5 vol. % PP/SWNT or PP/C12SWNT.

3.3.2 The Effect of Melt Extrusion Process Parameters on Dry Mixed Polypropylene Nanocomposites

0.5 % vol. SWNTs, obtained from Richard E. Smalley Institute for Nanoscale Science and Nanotechnology, or VGCF was initially mixed with PP pellets by manually shaking in a vial for 1 min. 2500 ppm HP 2215FF antioxidant was added prior to extrusion.

The extruder temperature, speed, and recirculation time was specified as dictated by the design. Stat-Ease Design-Expert 6.0 was used to generate the sequence of experimental runs and to analyze the results. For each of the nanomaterials employed, the factors examined were A-extrusion temperature, B-screw speed, and C-extrusion

time. Separate randomized 2-factorial designs consisting of 12 runs, including centre points and replicates, was carried out for each nanomaterial used in order to detect interactions while minimizing the number of runs required. The upper and lower levels of extrusion temperature, screw speed and extrusion time were 190 and 230 ^{o}C, 30 and 80 rpm and, 8 and 20 min respectively. The measured response variables studied were storage modulus, loss modulus, complex viscosity, damping factor, melting point, and crystallization temperature.

3.3.3 The Effect of Melt Extrusion Process Parameters on Hot Coagulated Polypropylene Nanocomposites

The materials used in this investigation were isotactic polypropylene pellets, Irganox HP 2215 FF stabilizer, Pyrograf III PR-19 vapor grown carbon fibers (VGCFs), and HiPco SWNTs obtained from Richard E. Smalley Institute for Nanoscale Science and Nanotechnology. The SWNTs were functionalized with dodecyl groups to produce C12SWNTs.

PP and 1% vol. nanomaterial were combined using the hot coagulation method explained in Section 3.3.1. The nanomaterials were sonicated in 1,2-dicholorbenzene (DCB), used as received from Sigma Aldrich, at a concentration of 2 mg/ml and room temperature. Atomic force microscopy (AFM) was used to determine the sonication time required for each material. While it is preferred to achieve dispersions of individuals where all three nanomaterials had the same length to diameter (aspect) ratios, the VGCFs' initial dimensions were much larger than those of the other materials. Therefore, the goal was to achieve similar aspect ratios for the SWNTs and C12SWNTs,

and a dispersion of primarily individual VGCFs. A sonication time of 30 min was selected for VGCF because this gave a dispersion of primarily individual VGCFs. However, the friable nature of VGCF, compared to SWNTs and C12SWNTs, resulted in a significant length reduction and an aspect ratio of only 50. A sonication time of 6 h was chosen for C12SWNTs because this resulted in dispersion of predominantly individual C12SWNTs. Sonication of SWNTs for 24 hours resulted in an equivalent average length to the C12SWNTs; however, even this lengthy sonication time only resulted in small bundles averaging 4 nm in diameter.

The vacuum dried product obtained from the hot coagulation mixing process was melt extruded in a Haake Minilab counter rotating twin screw extruder (at extrusion conditions determined by the DOE) with the addition of 2500 ppm of Irganox HP 2215 FF stabilizer. DCB coagulated and melt extruded blends of pure PP and stabilizer was fabricated for comparison to the nanomaterials; these samples are referred to simply as PP.

3.3.4 The Effect of Melt Extrusion Process Parameters on Rotary Evaporated Polypropylene Nanocomposites

The nanotubes used in this investigation were CoMoCat single-walled carbon nanotubes. SWNTs or C12SWNTs were dispersed in ~99 % isopropanol (IPA) at a concentration of 2 mg/ml with the aid of bath sonication. AFM was used to determine the sonication time required to result in similar average aspect ratios for the dispersed SWNTs and C12SWNTs. C12SWNTs were dispersed in the IPA with the aid of bath sonication for 1 h. For SWNTs, bath sonication for 6 hours at room temperature was employed. The

aspect ratios of SWNTs and C1SWNTs were between 200 – 300. While many individual nanotubes resulted from sonication, the majority of the nanotubes were dispersed as bundles of ~ 4 nm in diameter. After sonication, the nanotube dispersion was mixed with PP flakes using magnetic stirring for 10 minutes. The solvent was extracted using a rotary evaporator over 30 minutes at a temperature of 60 ^{o}C and a pressure of 0.4 bar. To further assure complete solvent removal, the nanotube coated PP was vacuum dried overnight at 120 ^{o}C to result in an initial mixture of 0.5 vol. % PP/SWNT or PP/C12SWNT.

The vacuum dried product obtained from the rotary evaporated mixing process was melt extruded in a Haake Minilab counter rotating twin screw extruder (at extrusion conditions determined by the DOE) with the addition of 2500 ppm of Irganox HP 2215 FF stabilizer.

Design of Experiments (DOE)

The factors examined were extrusion temperature (T), screw speed (n), extrusion time (t), nanomaterial type (M), and nanomaterial concentration (x) (in the design of experiments related to rotary evaporated nanocomposites). A randomized D-Optimal reduced cubic design, including center points and replicates, was used to minimize runs while retaining the ability to detect first order interactions. The lower and upper levels of extrusion temperature, screw speed, extrusion time, and nanomaterial concentration (only for the rotary evaporated nanocomposites) were 190 and 250 ^{o}C, 10 and 100 rpm,10 and 240 min, and 0.25 and 0.75 % vol. respectively. The upper level of 240 min for extrusion time, though seemingly high, was chosen based on the relatively low shear in the MiniLab and Huang et al.'s finding that it can take over 200 min to have a completely

dispersed state of nanotubes in the polymer by shear mixing (122). The experimental runs were randomized to mitigate potential effects from changes in environmental conditions and other unaccounted for factors. Several runs were repeated in order to ascertain experimental error and differentiate real effects from noise. The measured response variables included rheological responses, thermal decomposition temperature (T_d), melting point (T_m), and crystallization temperature (T_c).

3.4 Characterization

A Pacific Nanotechnologies (Santa Clara, CA) Nano-R Atomic Force Microscope (AFM) was used in tapping mode to determine the length to diameter ratios of SWNTs and C12SWNTs. Samples for AFM were prepared by dipping a very uniform piece of mica in the sample dispersion, followed by drying the piece overnight at 100 ^{o}C. The mica piece was then adhered to an AFM disc using double sided tape. A Nikon (Melville, NY) Eclipse 80I optical microscope under reflected light was used to image micro-scale distribution of nanotubes. The samples, as shown in Figure 3.4, were prepared by pressing the nanocomposite melt between two microscope slides heated on a hot plate at 180 ^{o}C. A 20x objective (0.45 NA) and a 2x magnification before the camera, translating into an effective magnification of 40x, was used to image the samples. The images obtained were processed in Nikon ImagePro and Microsoft PowerPoint software. SEM images were obtained using a JEOL (Tokyo, Japan) 7000-F Field Emission Scanning Electron Microscope; the specimens were sliced from the bulk nanocomposite and sputter coated with gold before imaging.

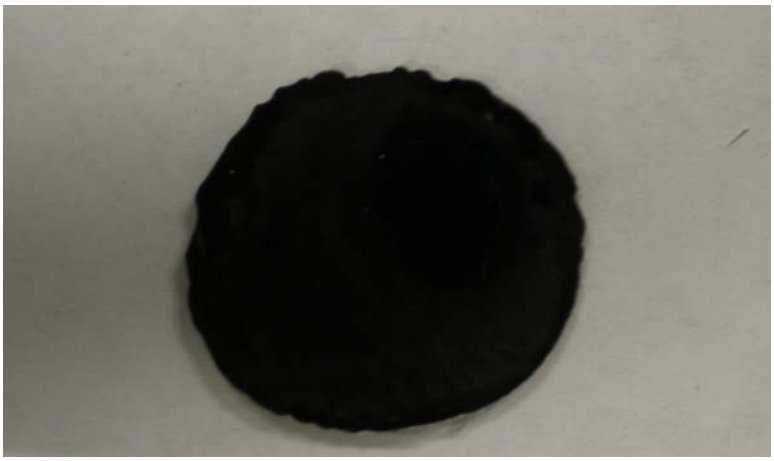

Figure 3.4. Nanocomposite sample for optical microscopy.

Raman spectra were obtained using a Renishaw (Hoffman Estates, IL) InVia Raman Spectrometer, with 514 nm or 785 nm laser and a Prior (Rockland, MA) scanning stage. Samples for Raman spectroscopy were prepared by fixing the nanotubes to microscope slides using double sided tape. A Leica 50x N-Plan objective (NA 0.75) was used to image the samples and the resulting laser spot size was 0.84 μm and 1.28 μm for the 514 nm and 785 nm lasers respectively. Raman maps were performed on samples, prepared in similar manner as for optical microscopy, by scanning an area of 10*10 μm^2. Data obtained from Raman spectroscopy was processed using Wire 2.0, Microsoft Excel, and/or Origin 8.0 software.

Melt and crystallization temperatures were measured on a TA Instruments (New Castle, DE) Q2000 Modulated Differential Scanning Calorimeter (DSC) at a scan rate of 10 ^{o}C/min over a temperature range of 50 to 200 ^{o}C, using Tzero aluminum hermetic pans/lids. The sample was first heated at 10 ^{o}C/min to 200 ^{o}C and held for 5 min, then cooled at 10 ^{o}C/min to 50 ^{o}C with a hold of 5 min before heating again at 10 ^{o}C/min to 200 ^{o}C. The heat-cool-heat cycle was performed to ensure the melting of all crystallites

and to remove thermal history. Isothermal crystallization studies were performed by heating the sample to 200 ^{o}C at 10 ^{o}C/min with an isothermal hold for 5 min to ensure the melting of all crystallites, followed by rapid cooling at 80 ^{o}C/min to the desired crystallization temperature and a consequent isothermal hold for 30 mins.

Thermal decomposition was studied using a TA Instruments (New Castle, DE) Q500 Thermal Gravimetric Analyzer (TGA). SWNTs and C12SWNTs were heated at 10 ^{o}C/min to 800 ^{o}C with an isothermal hold at 800 ^{o}C for 30 minutes under a constant nitrogen balance protection flow rate of 40 cm^3/min and a sample gas flow rate of 60 cm^3/min. In the case of nanocomposites, the samples were heated at 10 ^{o}C/min to 600 ^{o}C under a constant nitrogen flow. Thermal decomposition kinetics were studied using TA Instruments Modulated TGA^{TM} feature wherein the rate of weight loss, in response to temperature modulations, is used to estimate the activation energy of decomposition (140). The samples used for melt, crystallization, and decomposition studies were obtained by slicing off a piece from the bulk nanocomposite; typical samples are shown in Figure 3.5.

Figure 3.5. Nanocomposite samples for melt, crystallization, and decomposition studies.

Rheological characterization was performed on an Anton Paar (Ashland, VA) MCR 301 rotational rheometer, equipped with a CTD 450 convection temperature control device, using 25 mm parallel plates at a temperature of 200 ^{o}C. Frequency sweeps between 0.1 – 100 s^{-1} were performed at 5 % strain, which was well within the linear viscoelastic region for all composites. The samples used for rheological characterization were prepared by coiling molten nanocomposite on a brass wire when exiting from the extruder. A representation of the sample is shown below in Figure 3.6.

Figure 3.6. Nanocomposite sample for rheological characterization.

Nanocomposite tensile strength and Young's modulus were measured on a TA Instruments RSA III Dynamic Mechanical Analyzer. The fibers extruded for tensile tests ranged between 90 – 120 μm in diameter, and were extremely difficult to handle and introduce between the clamps of the test device. Thus, paper tabs, obtained from Miami Valley Gasket Co., Inc (Dayton, OH), were used to ensure easier handling. Samples for tensile testing were prepared by sticking the nanocomposite fibers to the paper tabs using Loctite brand super glue. A representation of the tensile test sample is shown in Figure 3.7. The sides of the tabs were cut after introducing it between the clamps of the

mechanical testing device. A guage length of 7.9 mm was used along with a strain rate of 0.033 mm/s for 120 s followed by 0.133 mm/s until break. At least 15 specimens were tested and averaged for each nanocomposite sample.

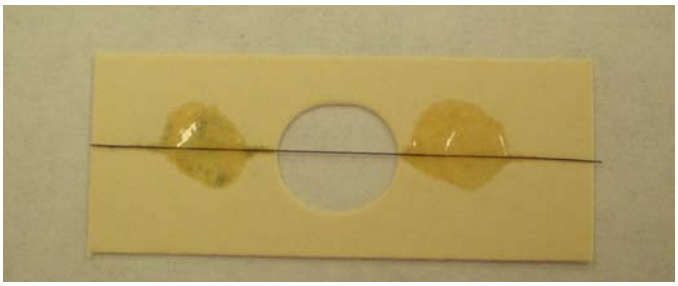

Figure 3.7. Nanocomposite fiber, sample adhered to a paper tab, for tensile testing.

Chapter 4

Influence of Initial Mixing Methods on Melt Extruded Single-Walled Carbon Nanotube – Polypropylene Nanocomposites

This chapter explores the effect of initial mixing of PP and nanotubes on the properties of the final melt extruded nanocomposites. Nanotubes and polymers are typically dry mixed prior to extrusion. However, investigations using this method (78,141,142) have generally resulted in large nanotube agglomerates, nonuniform nanotube distribution, and poor nanocomposite properties. This is largely attributed to the uneven nanotube distribution in the polymer prior to melt mixing. Another nanocomposite fabrication approach is to use solvents to facilitate carbon nanotube-polymer mixing; however even these methods are complicated by the limited solubility of pristine SWNTs in most solvents. Zhang et al. (2006) sprayed a dispersion of 1 wt. % SWNTs in aqueous sodium dodecyl sulfate onto high density polyethylene powder prior to extrusion in a Daca twin screw mini-compounder for 20 minutes at a screw speed of 50 rpm (77). Spray methods are industrially attractive because standard polyolefin additives are often added to polymer powder in tumbler driers just prior to extrusion. However, Zhang et al. found that a loading of approximately 1.5 wt. % SWNTs was required to achieve percolation. While this result is significantly better than results obtained using many other methods, it suggests that the SWNTs, while well distributed in the polymer matrix, were dispersed as large diameter bundles. The percolation threshold should be at least an order of magnitude lower for individually dispersed SWNTs. On the other hand, the hot

coagulation method developed by the Winey group (68,139) resulted in exceptionally well distributed, small 3 nm bundles in PE/SWNT composites. This, to the authors' knowledge, is the best degree of SWNT dispersion ever achieved in a polyolefin. Unfortunately, achieving this astounding result required dissolving both the SWNTs and polymer in hot dichlorobenzene (DCB), an expensive and environmentally unfriendly solvent. In addition, the SWNT/DCB dispersion had to be bath sonicated for 48 h; sonication is known to damage and shorten SWNTs thereby reducing the potential for property enhancement and increasing the nanotube loading required for percolation. The polymer is also likely to have degraded as a result of prolonged heating in DCB. Therefore, while this process gives outstanding results, its complexity limits its near term industrial viability.

This chapter describes the first direct comparison of dry-mixing, rotary evaporation (a modification of spray drying), and hot coagulation methods for incorporating SWNTs and sidewall functionalized dodecyl ($C_{12}H_{25}$) SWNTs into PP. The three initial mixing methods investigated resulted in three degrees of nanotube distribution in bulk polymer; thus allowing exploration of the effects of initial polymer and nanotube mixing method. The detailed experimental materials and procedure employed were described in Section 3.3.1. Isopropanol was selected as the solvent of choice in the rotary evaporation mixing because it did not induce significant PP degradation, and its high vapor pressure facilitated rapid and complete removal from the resulting composite. In preliminary studies, aqueous SDS was mixed with the PP based on the findings of Zhang et al (2006). However, in the absence of nanotubes, the PP which had been mixed with SDS and dried became dark yellow after extrusion. This

indicated that the presence of the SDS had resulted in increased polymer degradation. N-methyl-2-pyrrolidinone and 1, 2-dichlorobenzene (DCB) were also tried based on their ability to disperse SWNTs (143). However, they also induced polymer degradation during extrusion. Furthermore, their low vapor pressures and high boiling points made solvent removal challenging.

4.1 Evidence of $C_{12}H_{25}$ Functionalization

The Raman spectra of SWNTs (Figure 4.1a) showed that the D:G ratio was 0.17 prior to functionalization and 0.56 after functionalization; confirming covalent functionalization of the alkyl group to SWNTs. TGA (Figure 4.1b) provides further confirmation; the weight loss between 200 and 500 ^{o}C was much more significant for the C12SWNTs. This weight loss corresponds to the decomposition of $C_{12}H_{25}$ chains on SWNTs (113). Based on the weight loss observed on the TGA, the degree of functionalization was approximately one $C_{12}H_{25}$ for every 25 carbon atoms.

4.2 Morphology

The difference in macroscale distribution of SWNTs in PP after the initial mixing is clearly seen in Figure 4.2; similar results were observed for C12SWNTs. The nanotubes that were dry mixed tended to remain as large agglomerates and possess poor adhesion to the polymer surface. Rotary evaporation, on the other hand, yielded a well distributed initial mixture with a black carbon nanotube coating over the entire polymer surface. The hot coagulation method resulted in a uniformly gray product; the lighter color, compared

to the rotary evaporated materials, was indicative of the nanotubes blending with the entire polymer mass and not just adhering to the polymer surface.

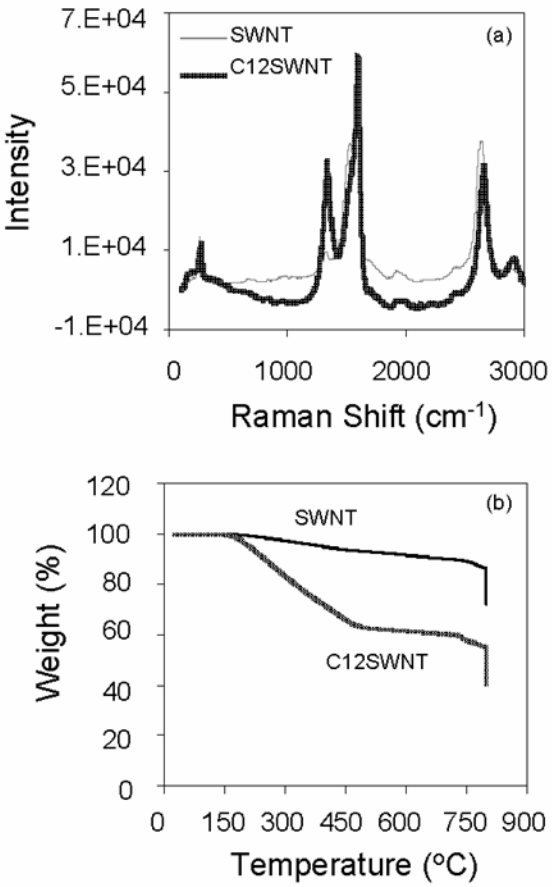

Figure 4.1. a) Raman spectra of SWNTs and C12SWNTs obtained with 514 nm laser. b) TGA weight loss curve of SWNTs and C12SWNTs under nitrogen atmosphere.

SEM, optical microscopy, and Raman mapping were performed on samples that were simply melt pressed (no extrusion) and samples that were extruded at 190 ^{o}C and 10 rpm for 10 minutes. For the melt pressed samples, optical microscopy (Figure 4.3) and Raman mapping (Figure 4.4) reinforced the macroscale observations that could be made from Figure 4.2. The least uniform composites prior to extrusion were prepared by dry mixing while the most uniform composites were prepared by hot coagulation.

Surprisingly, for all three methods the C12SWNT composites were slightly less uniform than SWNT composites prepared by the same method. In spite of the significant differences in aggregate size and distribution, SEM images (Figure 4.5) of the samples showed that in all the samples the smallest building blocks were SWNT bundles with an average diameter of approximately 100 nm. This diameter is very similar to the original rope size found in HiPco SWNTs (144). It is interesting that even though the rotary evaporation and hot coagulation methods resulted in much smaller bundle sizes while dispersed in the solvents, the bundle size of all the melt pressed composites was quite similar to the size of the original ropes.

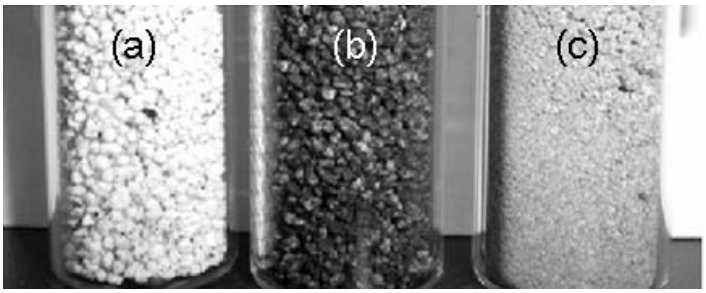

Figure 4.2. Macroscale appearance of PP-SWNT after initial mixing but prior to melt extrusion for (a) dry mixing, (b) rotary evaporation, and (c) hot coagulation.

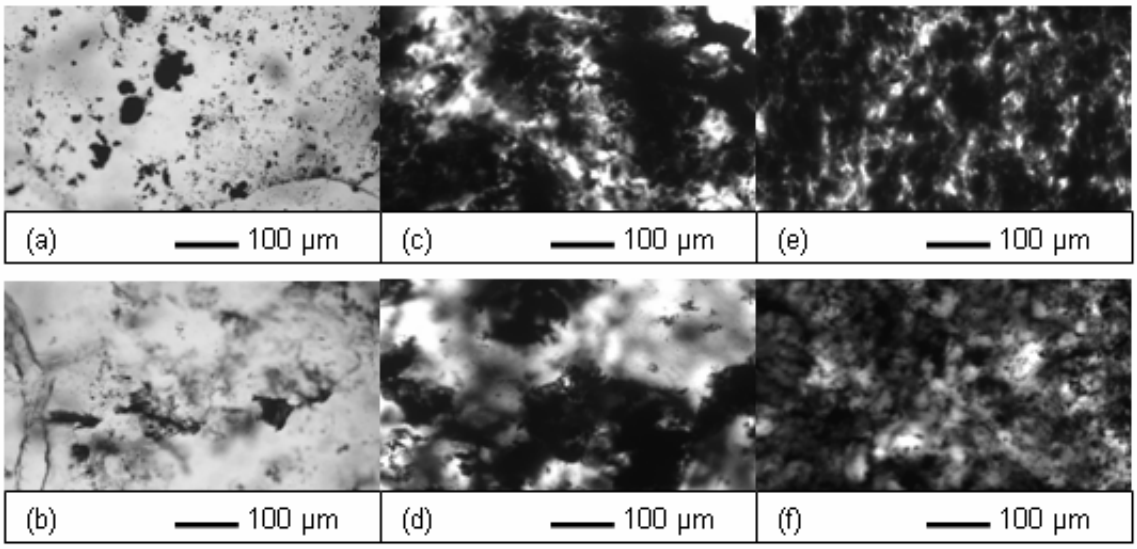

Figure 4.3. Optical microscopy images of melt pressed (unextruded) nanocomposites (a) and (b) PP/SWNT and PP/C12SWNT by dry mixing, (c) and (d) PP/SWNT and PP/C12SWNT by rotary evaporation, and (e) and (f) PP/SWNT and PP/C12SWNT by hot coagulation.

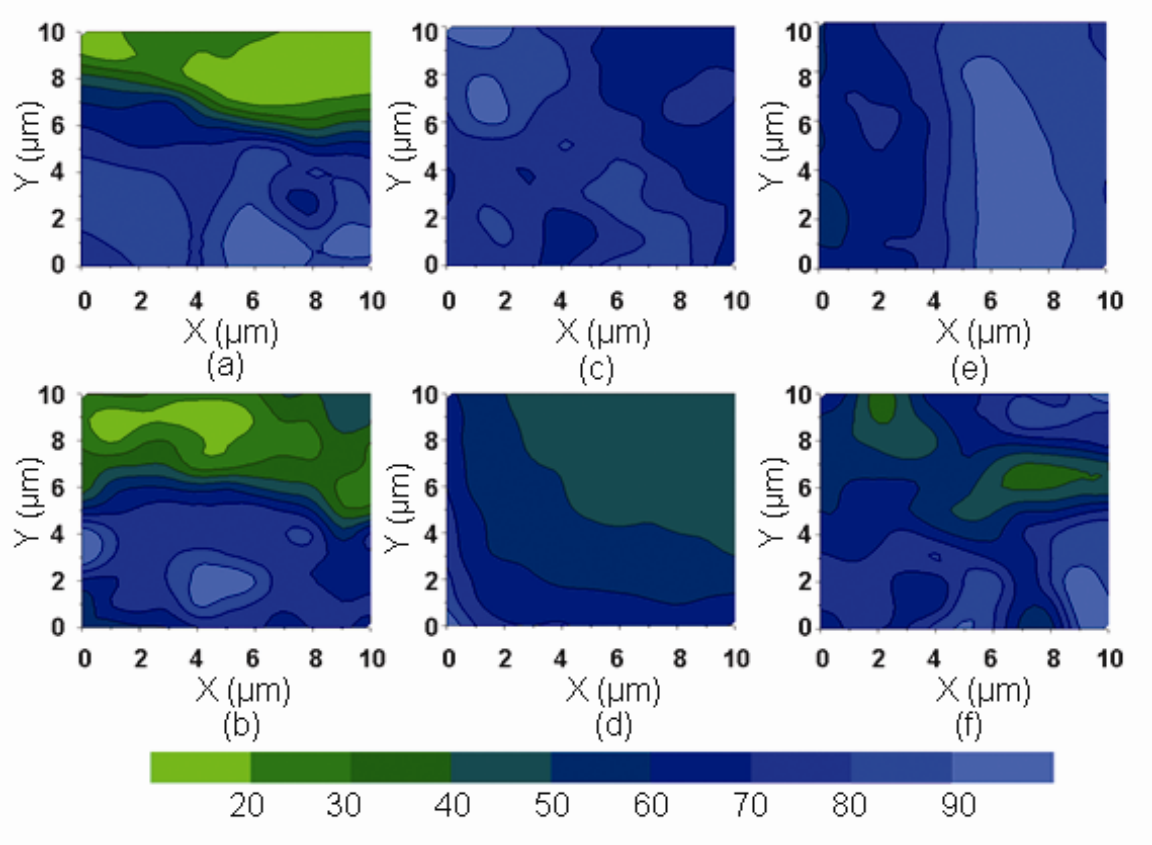

Figure 4.4. Raman maps of melt pressed (unextruded) nanocomposites (a) and (b) PP/SWNT and PP/C12SWNT by dry mixing, (c) and (d) PP/SWNT and PP/C12SWNT by rotary evaporation, and (e) and (f) PP/SWNT and PP/C12SWNT by hot coagulation.

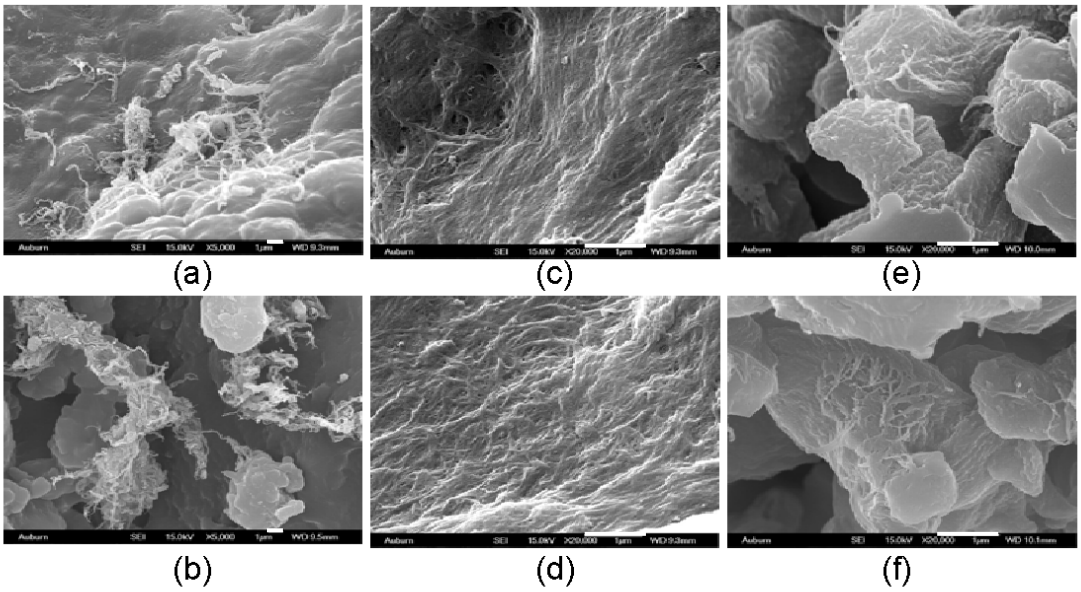

Figure 4.5. SEM images of melt pressed (unextruded) nanocomposites (a) and (b) PP/SWNT and PP/C12SWNT by dry mixing, (c) and (d) PP/SWNT and PP/C12SWNT by rotary evaporation, and (e) and (f) PP/SWNT and PP/C12SWNT by hot coagulation. Scale bars on all images are 1 μm.

After melt extrusion, all of the composites were more uniform. SEM images for all samples were very similar (Figure 4.6) and revealed that average bundle diameter in all composites was approximately 10 nm. Therefore, even though the Haake MiniLab lacks any mixing elements, it did affect the degree of dispersion. Due to the fact that SEM only probes the surface of a small area of sample, optical microscopy was better suited to distinguishing the differences in nanotube distribution between samples (Figure 4.7). Even after extrusion, nanotube aggregates, tens of microns in diameter, were still

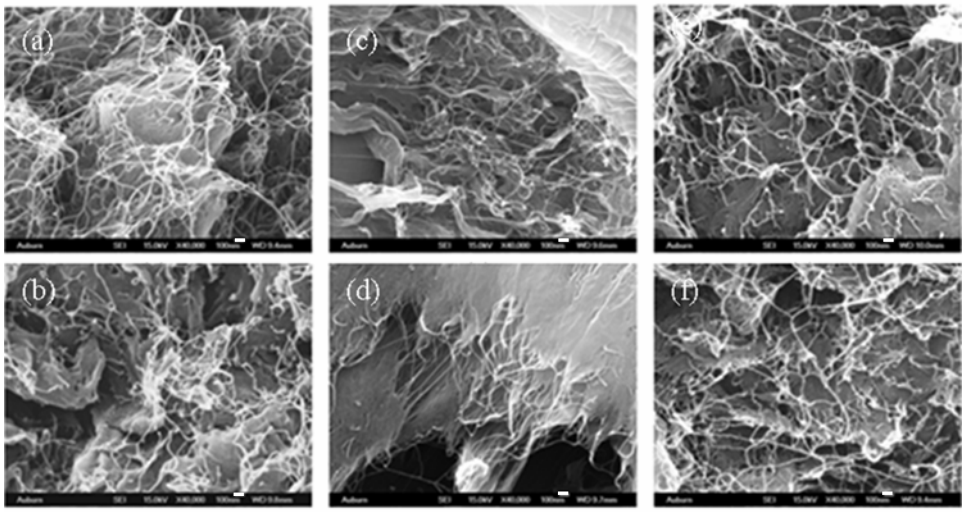

Figure 4.6. SEM images of melt extruded nanocomposites (a) and (b) PP/SWNT and PP/C12SWNT by dry mixing, (c) and (d) PP/SWNT and PP/C12SWNT by rotary evaporation, and (e) and (f) PP/SWNT and PP/C12SWNT by hot coagulation. Scale bars on all images are 100 nm.

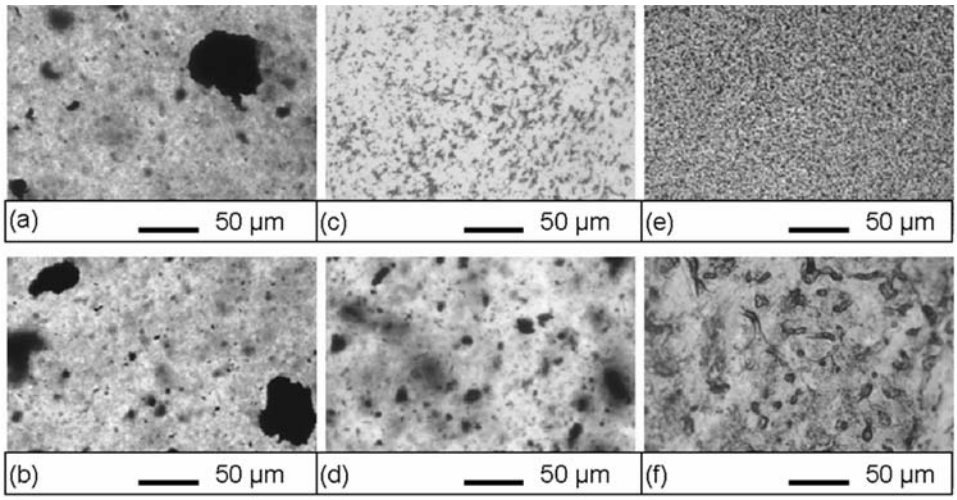

Figure 4.7. Optical microscopy images of melt extruded nanocomposites (a) and (b) PP/SWNT and PP/C12SWNT by dry mixing, (c) and (d) PP/SWNT and PP/C12SWNT by rotary evaporation, and (e) and (f) PP/SWNT and PP/C12SWNT by hot coagulation.

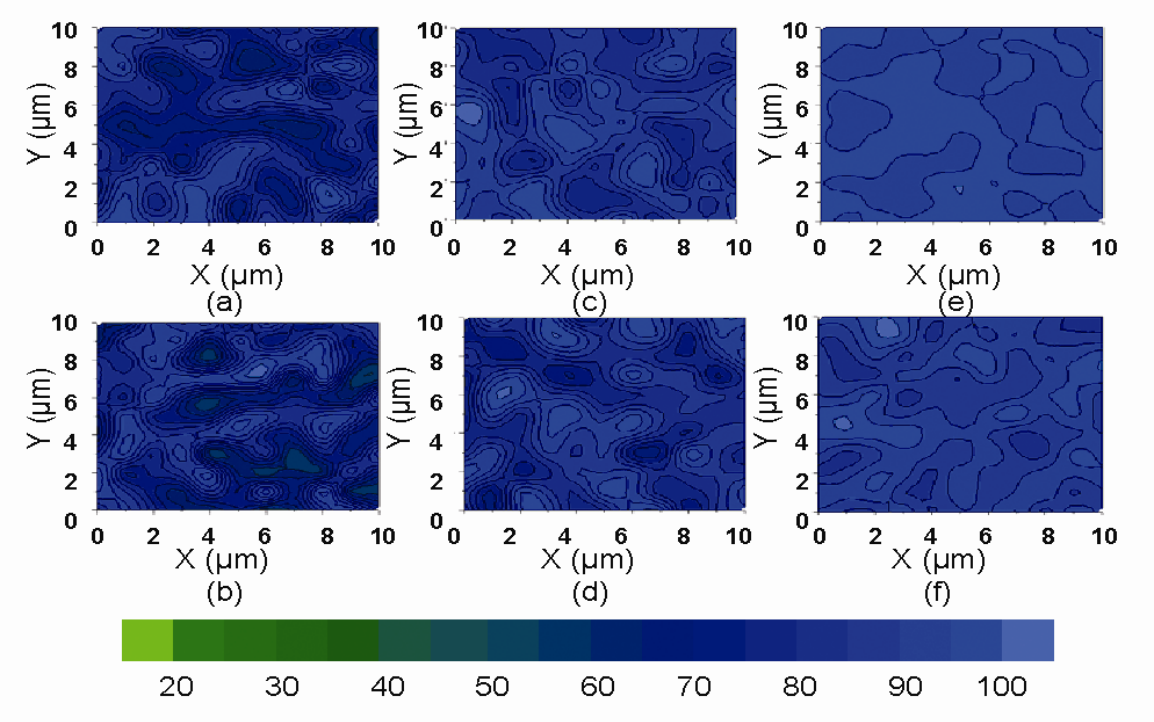

Figure 4.8. Raman maps of melt extruded nanocomposites (a) and (b) PP/SWNT and PP/C12SWNT by dry mixing, (c) and (d) PP/SWNT and PP/C12SWNT by rotary evaporation, and (e) and (f) PP/SWNT and PP/C12SWNT by hot coagulation.

visible in the dry mixed nanocomposites. Nanotube aggregates were also visible in the extruded rotary evaporator mixed nanocomposites, but the aggregate size was much smaller. The hot coagulated SWNT nanocomposites appeared very uniform. However, for this method, as well as the others, the C12SWNT nanocomposites appeared less uniform than the SWNT nanocomposites.

In order to quantify the differences in composite uniformity, Raman mapping was performed (Figure 4.8). Within a given sample, the relative G-band intensity is simply a function of nanotube concentration; higher intensity indicates a higher localized SWNT concentration. Raman intensity maps provide a clear visualization of the differences

between composite dispersion from sample to sample and the data can be quantified in terms of the standard deviation of the intensities (145) in the 100 μm^2 map (Table 4.1).

	Dry Mixed	Rotary Evaporation	Hot Coagulation
SWNT	11.5	7.9	2.7
C12SWNT	13.9	9.5	5.1

Table 4.1. Standard deviation of G band intensities for melt extruded samples obtained by Raman mapping.

Therefore, since Raman mapping is quantitative and not affected by sample opacity it provided a better assessment of uniformity than SEM or optical microscopy. The Raman mapping results confirmed that hot coagulation resulted in the most uniform composites and that in all cases the C12SWNTs were more poorly distributed than SWNTs. The poorer distribution of the C12SWNT composites is contrary to the expectation that surface modification, even below the length required for entanglement with polymer chains, should result in lower aggregation tendencies due to a combination of increased steric hindrance and improved interfacial compatibility. Initially it was thought that this counter-intuitive result was due to the fact that the functionalization process involves a vacuum filtration step, and prolonged vacuum filtration can result in nearly irreversible aggregate formation (146). However, this possibility was eliminated. Aggregate formation should have been observed in AFM images from the solvent dispersed C12SWNTs, but for both the IPA dispersions used in rotary evaporation and DCB dispersions used in hot coagulation, AFM showed more initial aggregates for the SWNT dispersions than for the C12SWNT dispersions. In addition, the C12SWNTs

achieved a smaller bundle size more quickly than the SWNTs. Therefore the poorer dispersion of the C12SWNTs must be related to the C12SWNT/C12SWNT interactions being stronger than PP/C12SWNT interactions. Lee et al (2007) similarly observed that MWNTs functionalized with amine groups were more poorly dispersed than MWNTs that were slightly oxidized by heating in air. They attributed the poor dispersion of the amine functionalized MWNTs to hydrogen bonding (147). However, hydrogen bonding is unlikely to be significant for the alkyl functionalized SWNTs. It is possible that interactions between C12SWNTs and the polymer additives were a factor, and such interactions may be explored in future work.

4.3 Rheology

Rheological behavior is one of the most sensitive probes of nanocomposite microstructure. Figure 4.9a shows the dependence of complex viscosity η^* on frequency within the linear viscoelastic region. The effect of initial mixing on complex viscosity, a measure of the resistance of the sample to oscillatory shear, is significant and most evident at low frequencies. The similarity between the complex viscosity of dry mixed samples and PP is indicative of poor dispersion and consistent with the optical microscopy and Raman mapping results. In contrast, the complex viscosity of the hot coagulated nanocomposites was almost an order of magnitude higher than that of the dry mixed nanocomposites. This was due to the resistance to flow imparted by the well distributed high aspect ratio nanotubes. It should be noted that the PP results shown in Figure 4.9 are representative of PP which had been sprayed with IPA and dried prior to extrusion.

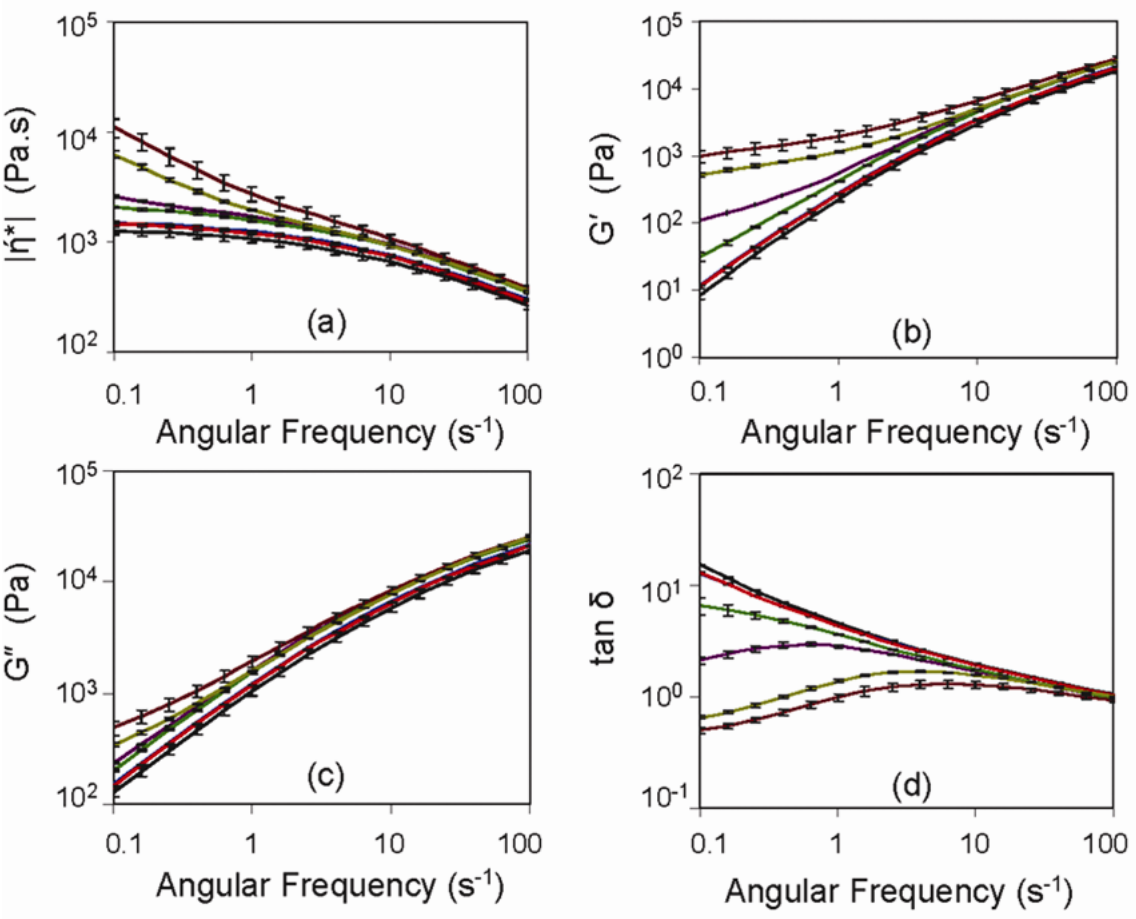

Figure 4.9. Nanocomposite (a) complex viscosity, (b) storage modulus, (c) loss modulus, and (d) tan δ as a function of angular frequency — PP/SWNT DM, — PP/C12SWNT DM, — PP/SWNT RE, — PP/C12SWNT RE, — PP/SWNT HC, — PP/C12SWNT HC, — PP.

However, PP which was subjected to the long heating in DCB characteristic of the hot coagulation process had an approximately 30% lower viscosity indicating that DCB processing resulted in some polymer degradation. The significant difference between the hot coagulated PP/SWNT and PP/C12SWNTs provides still further confirmation of the optical microscopy and Raman mapping results that the C12SWNTs were more poorly

distributed in the matrix. The complex viscosity of the nanocomposites prepared by rotary evaporation was between that of the dry mixed and hot coagulated nanocomposites. This is due to the fact that while mixing and solvent removal in the rotary evaporator leads to good distribution of nanotubes coating the polymer, and thus a much more uniform feed to the extruder than dry mixing, it lacks the uniform intimate interaction between the nanotubes and polymer chains that is achieved by the hot coagulation method.

The storage modulus G′ (Figure 4.9b) provides further insight into nanocomposite viscoelasticity. At low frequencies, representative of long time scales, the PP chains were relaxed and exhibit typical terminal behavior with G′ roughly proportional to ω^2. Surprisingly, even with the addition of 0.5 vol. % SWNTs and C12SWNTs, the dry mixed nanocomposites did not show any deviation in the terminal region indicating that the large nanotube aggregates provided no resistance to polymer relaxation. However, with the rotary evaporated and hot coagulated PP/SWNT and PP/C12SWNT nanocomposites, deviations are observed. The effective surface coating achieved in the initial mixing of the rotary evaporated nanocomposites resulted in a decrease in the frequency dependence of G′ at low frequencies. For the hot coagulated samples this was even more pronounced; G′ was nearly frequency independent at 0.1 s^{-1}. This coupled with the nearly two order of magnitude increase over the storage modulus of PP, suggested that 0.5 vol. % was near, but slightly below, the percolation threshold ϕ_c for the hot coagulated samples (127,130). The fact that 0.5 vol. % was slightly below ϕ_c further supports the SEM finding that the nanotubes are dispersed as small ~ 10 nm diameter bundles. If the nanotubes had been individually dispersed in the composites produced by

hot coagulation, a clear frequency independent plateau indicative of percolation would exist at even an order of magnitude lower concentration. The lower storage moduli for C12SWNTs compared to equivalently processed SWNTs also further highlighted the C12SWNTs' poorer dispersion. For dry mixing, the difference was minimal because in both cases there were numerous large aggregates. For the hot coagulated samples, the difference was statistically significant but fairly small since both the C12SWNTs, and SWNTs were reasonably well distributed. However, for the rotary evaporated samples the difference was so significant that while G′ for the C12SWNT samples was higher than for the dry mixed samples, the level of dispersion and uniformity was inadequate to result in a significant change in slope at low frequencies. The loss modulus G″ (Figure 4.9c) which probes the viscous response of the nanocomposites provided similar information, but as expected the differences were less pronounced.

Plotting the damping factor, $\tan \delta = G''/ G'$ as a function of frequency (Figure 4.9d) provided information on the microstructure as well as interfacial interactions between the nanotubes and PP matrix (131). For all nanocomposites, except those prepared by hot coagulation, $\tan \delta > 1$ at all frequencies, indicating the dominance of the viscous response of the PP matrix. However, for the hot coagulated samples, $\tan \delta < 1$ at low frequencies indicating the dominance of the elastic nanotube network at long time scales. The flatness of the tan δ versus frequency curve for the hot coagulated samples was also indicative of significant interfacial interaction. The fact that the shape is similar for the hot coagulated PP/C12SWNT and PP/SWNT indicated that the functionalization provided no overall benefit. In fact, for the rotary evaporated samples, where there was

an even greater difference in dispersion between the SWNTs and C12SWNTs, the curve was much steeper for the PP/C12SWNTs.

Differences in nanocomposite microstructure are further highlighted in the Cole-Cole plot shown in Figure 4.10. The dry mixed nanocomposites showed the same linear relationship between G′ and G″ as PP. The rotary evaporated PP/C12SWNTs showed a slight deviation from this behavior, while the rotary evaporated PP/SWNTs showed an even greater deviation. Since a higher G′ value for a given G″ value is representative of a significantly more complex structure of the sample (130) this was further evidence of the significant difference between rotary evaporated PP/SWNT and PP/C12SWNT. As expected, the greatest deviation from linearity was seen for the hot coagulated samples indicating the presence of a highly complex microstructure.

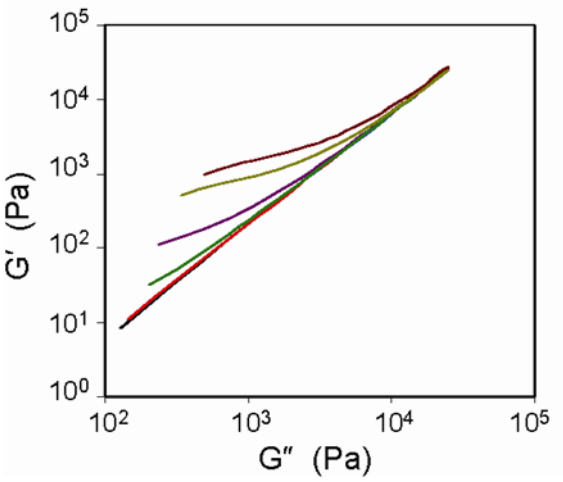

Figure 4.10. Cole-Cole Plot, data markers are identical to those in Figure 4.9.

4.4 Thermal Properties

The thermal properties of thermoplastics are known to be significantly affected by the presence of nanotubes; one of the motivations for including nanotubes in thermoplastics is to improve thermal stability. Measurement of nanocomposite melting temperature T_m using DSC showed that the melting temperature was not affected by the presence of the nanotubes; for both PP and all the nanocomposites $T_m = 164 \pm 1\ ^oC$. In contrast, even for the dry mixed nanocomposites, the crystallization temperature was affected by the nanotubes; T_c increased by 6 ^oC to $T_c = 122\ ^oC$ for both PP/SWNT and PP/C12SWNT (Table 4.2). This increase was due to the nanotubes providing heterogeneous nucleation sites (133); similar results have been obtained by other researchers. For a loading of 1wt. % SWNTs, Bhattacharyya et al. (132) observed an 11 ^oC increase in T_c and Manchado et al. (78) observed a 5 ^oC increase. For a given loading, the number of heterogeneous nucleation sites increases with dispersion uniformity and fewer and/or smaller aggregates. Consistent with the nanocomposite uniformity determined by Raman mapping, T_c increases to 126 ^oC for the more uniform rotary evaporated PP/SWNT. For the even more uniform hot coagulated PP/SWNT, T_c increased by 12 ^oC to 128 ^oC; the rheologically observed polymer degradation was not sufficient to significantly affect the T_c of the hot coagulated PP. For the rotary evaporated and hot coagulated samples T_c was slightly lower for the PP/C12SWNTs than for PP/SWNTs, but the difference was close to the measurement error. To further explore the effects of initial mixing, the half times $t_{1/2}$ and activation energies for crystallization ΔE_{ac} of the nanocomposites were measured (the molecular weight of PP in the nanocomposites was assumed to be constant for all nanocomposites in the calculations). The magnitude of $t_{1/2}$ is a function of both

crystallization kinetics and the total number of nucleation sites, while ΔE_{ac} is a measure of the energy barrier to crystallization. As described in Section 2.9.3, the crystallization kinetics were studied using the Avrami equation (134); the Avrami exponent and the bulk crystallization constants are obtained as the slope and intercept by plotting $\ln\left[-\ln\left(1-X_t\right)\right]$ vs $\ln(t)$ as shown in Figure 4.11.

SAMPLE		T_c (°C)	Crystallization Half-time (at 125 °C) $t_{1/2}$ (s)	Crystallization Activation Energy ΔE_{ac} (kJ/mol)	T_d (°C)	Decomposition Activation Energy ΔE_{ad} (kJ/mol)
	PP	116	93	351	404	185
DRY MIX	**SWNT**	122	34	284	403	193
	C12SWNT	122	40	309	408	200
ROTARY EVAP.	**SWNT**	126	22	260	415	210
	C12SWNT	123	31	288	412	198
HOT COAG.	**SWNT**	128	17	199	418	170
	C12SWNT	126	23	278	418	193

Table 4.2. Crystallization and decomposition temperatures and activation energies, and crystallization half-times of melt extruded PP, PP/SWNT, and PP/C12SWNT nanocomposites. Error in T_c and T_d ~ 1 °C, and in $E_{a,c}$ and $E_{a,d}$ ~ 2 kJ/mol.

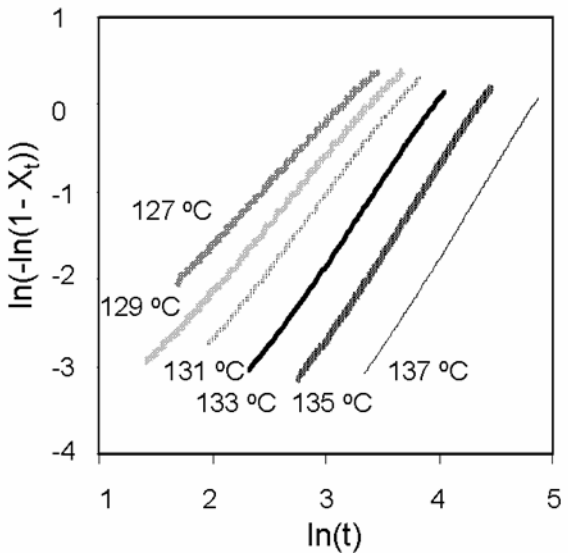

Figure 4.11. Avrami plot of PP/SWNT processed by hot coagulation method.

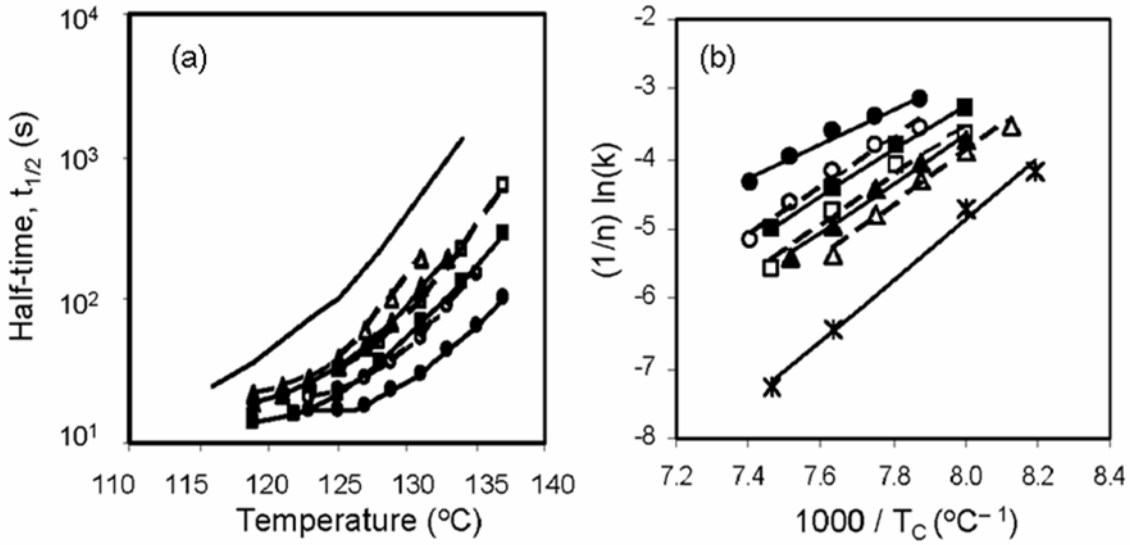

Figure 4.12. (a) Crystallization half-times of the nanocomposites as a function of temperature. Melt extruded pure PP is represented by dark line. (b) Arrhenius plot to estimate activation energy from isothermal crystallization data. (×) represents melt extruded pure PP. Triangles, squares, and circles represent dry mixed, rotary evaporator mixed, and hot coagulated nanocomposites respectively. Filled symbols represent PP/SWNT and open symbols represent PP/C12SWNT.

Figures 4.12a and 4.12b show the plots used to obtain the values of $t_{1/2}$ and ΔEac contained in Table 2. Both values are affected by the presence of the nanotubes and dispersion since heterogeneous nucleation sites tend to lower $t_{1/2}$ and ΔE_{ac} (148). However, ΔE_{ac} is also affected by other factors. For example, the increased viscosity and lower polymer chain mobility resulting from the presence of well dispersed nanotubes tends to increase ΔE_{ac} particularly in the presence of a percolated network. In this investigation, both $t_{1/2}$ and ΔE_{ac} trend with the morphological and rheological results on dispersion; the better dispersed nanocomposites had lower crystallization half times and lower activation energies. For the hot coagulated PP/SWNT, $t_{1/2}$ is only 17 s compared with 93 s for extruded PP and 137 s for hot coagulated and extruded PP. Similarly, ΔE_{ac} = 199 kJ/mol compared to 351 kJ/mol for extruded PP and 245 kJ/mol for DCB processed PP. Clear differences were also seen between the crystallization activation energies for PP/SWNT and PP/C12SWNT mixed by the same method. For the hot coagulated PP/C12SWNT nanocomposites, $t_{1/2}$ = 23 s and ΔE_{ac} = 278 kJ/mol. Interestingly, in some cases the difference between the SWNTs and C12SWNTs was as significant as the difference between the mixing methods.

The thermal decomposition temperatures T_d were determined using thermal gravimetric analysis and are also shown in Table 4.2. The carbon nanotubes increased T_d through stabilization of PP chains in the SWNT/polymer interphase (149) and reduced transport of evolved decomposition products (149,150). Better dispersion leads to both larger interphase volumes and the formation of a nanotube network results in significantly reduced transport. The dry mixed nanocomposites showed the least change in T_d, while both the rotary evaporated and hot coagulated samples showed greater than a 10 ^oC

improvement. As was the case for T_c, there were no clear trends for the values for equivalently processed PP/SWNT and PP/C12SWNT composites

Thermal decomposition kinetics was studied by employing TA Instruments' Modulated TGA™ feature; the rate of weight loss, in response to temperature modulations, was used to estimate the activation energy of decomposition ΔE_{ad}. Testing select samples by both this method and the more traditional isothermal decomposition method gave equivalent results. The nonisothermal method was advantageous because it required less instrument time. As expected, ΔE_{ad} increased slightly from 185 to 195 kJ/mol for the 0.5 vol. % dry mixed SWNTs. The more uniform dispersion enabled by the rotary evaporation method enabled further increase to 210 kJ/mol for PP/SWNT. However, for the hot coagulated and extruded PP/SWNT, ΔE_{ad} was a mere 170 kJ/mol. This result can be attributed to the effect of the hot coagulation process on the PP. As was the case for crystallization, while the polymer degradation resulting from the hot coagulation method did not significantly affect thermal decomposition temperature, it did significantly affect decomposition kinetics. While ΔE_{ad} = 185 kJ/mol for the extruded PP it was a mere 137 kJ/mol for the hot coagulated PP. Therefore, PP/SWNT ΔE_{ad} = 170 kJ/mol represented a 33 kJ/mol improvement over equivalently processed PP, compared to 25 kJ/mol improvement for rotary evaporated PP/SWNT. In contrast, there were no clear trends for the values of ΔE_{ad} for PP/C12SWNTs. As expected based on dispersion uniformity, for the rotary evaporated composites both T_d and ΔE_{ad} were higher for PP/SWNTs than PP/C12SWNTs. However, for both the dry mix and hot coagulation methods ΔE_{ad} was higher for PP/C12SWNTs than for PP/SWNTs even though the values

of T_d were equivalent for the hot coagulation method and T_d of the dry mixed PP/C12SWNT was higher than that for dry mixed PP/SWNT.

4.5 Tensile strength and modulus

Table 4.3 summarizes the results from mechanical tests on the nanocomposites. The addition of nanotubes drastically increased the Young's modulus of all nanocomposites while only marginally increasing the tensile strength of the RE and HC nanocomposites. The modest increase in tensile strength was surprising considering the excellent dispersion obtained, especially in HC nanocomposites. These results were, however, comparable to those obtained by Manchado et al. (78).

Sample	**Tensile Strength (MPa)**	**Youngs Modulus (MPa)**
PP	38.8 ± 2.6	756 ± 61
PP-SWNT DM	36.6 ± 3.2	1647 ± 220
PP-C12SWNT DM	36.0 ± 4.3	1686 ± 314
PP-SWNT RE	37.9 ± 3.9	1734 ± 209
PP-C12SWNT RE	39.5 ± 4.5	1918 ± 204
PP-SWNT HC	42.0 ± 3.4	2349 ± 182
PP-C12SWNT HC	40.0 ± 3.1	2102 ± 204

Table 4.3. Tensile strength and Young's modulus of PP nanocomposites.

4.6 Conclusions

This investigation clearly showed that the degree and uniformity of carbon nanotube distribution in polymer, prior to melt extrusion, in a Haake Minilab is critical to imparting their properties to bulk composite materials. Morphological evaluations demonstrated that the best dispersion was achieved from the hot coagulation process, and the poorest dispersion from dry blending, with rotary evaporation mixing falling somewhere in between. However, rheological and thermal characterizations revealed that dispersion alone does not tell the whole story; the effects of the dispersion process on the polymer must be considered in conjunction. The hot coagulation process resulted in polymer degradation as evidenced by a deterioration of rheological and thermal properties of the pure polymer. This degradation limited the property improvement enabled by incorporating nanotubes through the hot coagulation process. Rotary evaporation mixing resulted in a uniform coating of nanotubes on PP surface, which translated into significantly improved nanotube distribution and dispersion compared to dry mixed methods in the final melt extruded nanocomposites. Rotary evaporator processing of plain PP resulted in minimal polymer deterioration. Further optimization of the rotary evaporation process, perhaps in conjunction with an extruder containing distributive mixing elements, may ultimately provide the most scalable process and perhaps even the greatest nanocomposite property improvements. In addition, it must be noted that melt extrusion conditions also play a pivotal role in the dispersion and distribution of the nanotubes in PP. Thus, melt extrusion process parameters also require optimization to ultimately lead to maximized nanocomposite properties.

Chapter 5

The Effect of Melt Extrusion Process Parameters on Dry Mixed Polypropylene Nanocomposites

The previous chapter revealed that the distribution of the nanomaterials in the bulk polymer prior to melt extrusion has a significant effect on the dispersion and properties of the final melt extruded nanocomposites. It must also be realized that the processing parameters employed during melt extrusion also play a vital role in determining the final nanocomposite properties. For example, the lower viscosity of the polymer matrix at high melt extrusion temperatures results in greater nanomaterial mobility, thus leading to better dispersion. However, higher temperatures also tend to deteriorate polymer properties. Understanding the individual and combined effects of the melt extrusion conditions provides insight into designing better processing conditions. The previous chapter showed that PP nanocomposites fabricated from materials that were dry mixed tended to possess large nanotube aggregates after extrusion at 190 ^{o}C, 10 rpm, and 10 min.

This chapter investigated the influence of melt processing conditions on the properties of PP nanocomposites that were initially mixed by dry mixing. A detailed description of the materials and procedure employed is provided in Section 3.3.2. The melt extrusion process parameters investigated included extrusion temperature, extrusion speed, and extrusion time. A design of experiments approach was employed to

investigate the individual and combined effects of the process factors on the nanocomposites.

5.1 Results and Discussion

As seen in the previous chapter, optical microscopy images showed that simple dry mixing of the nanomaterials and PP before melt extrusion did not break apart the aggregates of nanomaterials in the melt extruded nanocomposite (Figure 5.1). The poor dispersion and presence of large aggregates was probably a result of insufficient shear applied on the nanotubes and lack of distributive and dispersive mixing in the extruder.

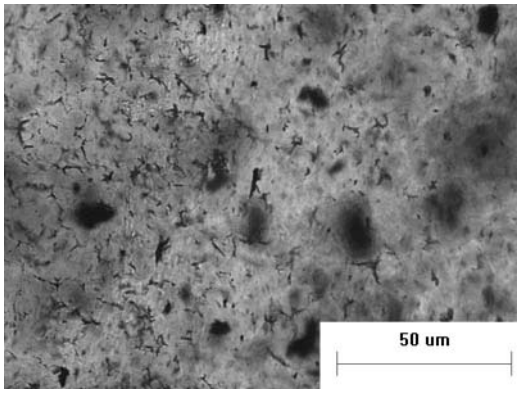

Figure 5.1. Optical microscopy image of melt extruded PP-SWNT nanocomposite.

Std	Run	Temperature (°C) Factor - A	Speed (rpm) Factor - B	Time (min) Factor -C	Melt Temperature (°C)	Crystallization Temperature (°C)
8	1	230	80	20	155.1	109.23
11	2	210	55	14	156.75	109.05
4	3	230	80	8	156.82	107.84
3	4	190	80	8	156.23	111.24
1	5	190	30	8	154.11	109.04
10	6	210	55	14	156.08	108.44
7	7	190	80	20	154.84	107.09
6	8	230	30	20	155.18	109.59
12	9	210	55	14	155.07	110.11
2	10	230	30	8	156.13	108.65
5	11	190	30	20	156.34	105.96
9	12	210	55	14	155.53	109.3

Table 5.1. Run sequence for dry mixed PP-SWNT nanocomposites generated by Design Expert 6.0.

As shown in Table 5.1, processing conditions did not have much effect on the thermal properties of the nanocomposite; there was approximately 3 °C variation in the melt and crystallization temperature. Investigating a wide range of processing conditions revealed that the processing conditions employed in the extruder were insufficient to effectively break apart the nanotube aggregates, resulting in a low number of nucleation sites for PP crystallization. Thus, no enhancement in thermal properties was observed. Dynamic rheological tests were carried out on the nanocomposite samples within the linear viscoelastic region. The tests, as seen in Figure 5.2, did not show any appreciable differences in the storage and loss moduli of the nanocomposites compared to plain PP.

However, PP-C12SWNT nanocomposites fabricated at 230 ^{o}C, 80 rpm, and 20 min displayed over 65% increase in storage modulus and an equivalent increase in loss modulus over other nanocomposites. Storage modulus, as mentioned earlier, is a measure of the elasticity of a material. The absence of a low frequency plateau in the storage modulus indicates that the nanotubes were not dispersed well and did not form a percolated network. SWNTs are rigid rods with large persistence lengths of approximately tens of microns (151,152). As stated in earlier sections, rods in a network percolate at a critical concentration between 0.001 and 0.002 for an average aspect ratio of 700. Figure 5.3 shows the complex viscosity of the nanocomposites. Due to the presence of aggregates, neither nanomaterial addition nor processing variations resulted in any increase in the complex viscosity. PP-C12SWNT nanocomposites melt extruded at 230 oC, 80 rpm, and 20 min, however, did show roughly a 70% increase in complex viscosity over plain PP processed at the same conditions. Therefore, functionalizing the SWNTs with C12 groups improved dispersion of nanotubes compared to unfunctionalized SWNTs. It is also observed that while the higher processing conditions decreased the storage and loss modulus, and complex viscosity values of plain PP, PP-VGCF, and PP-SWNT nanocomposites compared to the other two processing conditions; the values of PP-C12SWNT did not vary. This further supports that better dispersion of nanotubes in PP-C12SWNT, compared to the other nanocomposites, provided it with enhanced thermal stability allowing it to maintain its storage and loss modulus, and complex viscosity values even at the higher processing conditions.

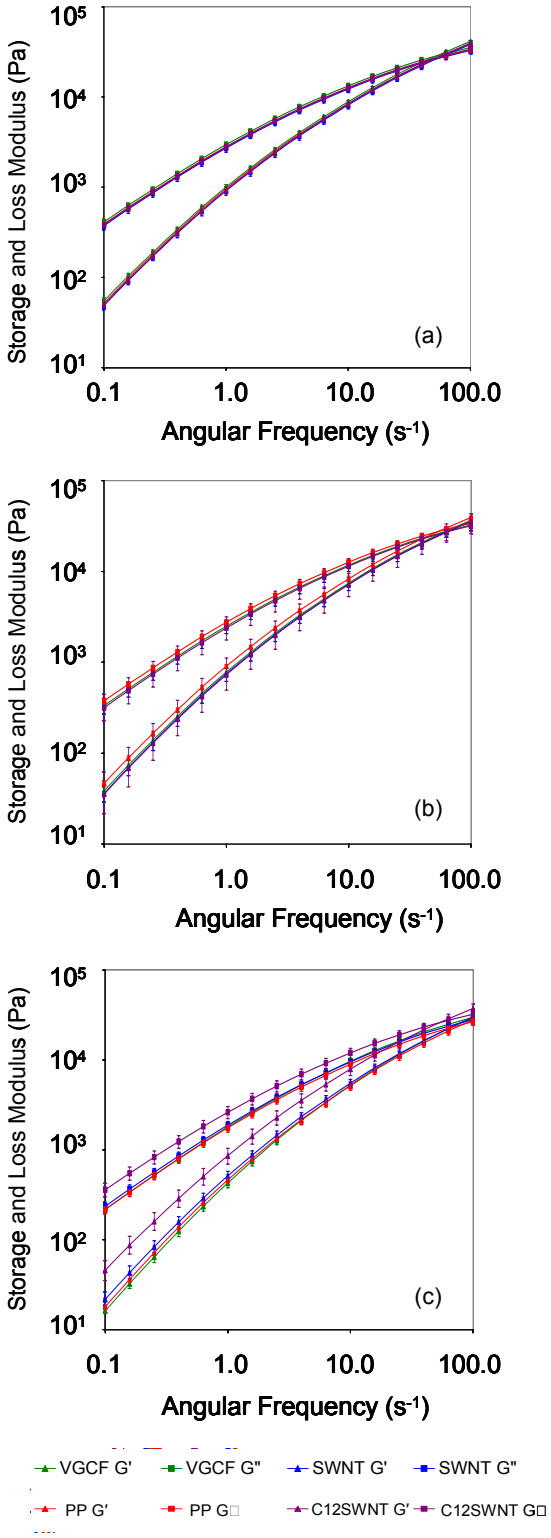

Figure 5.2. Storage (G') and loss (G") modulus of PP nanocomposites extruded at (a) 190 °C, 30 rpm, 8 min (b) 210 °C, 55 rpm, 14 min (c) 230 °C, 80 rpm, 20 min

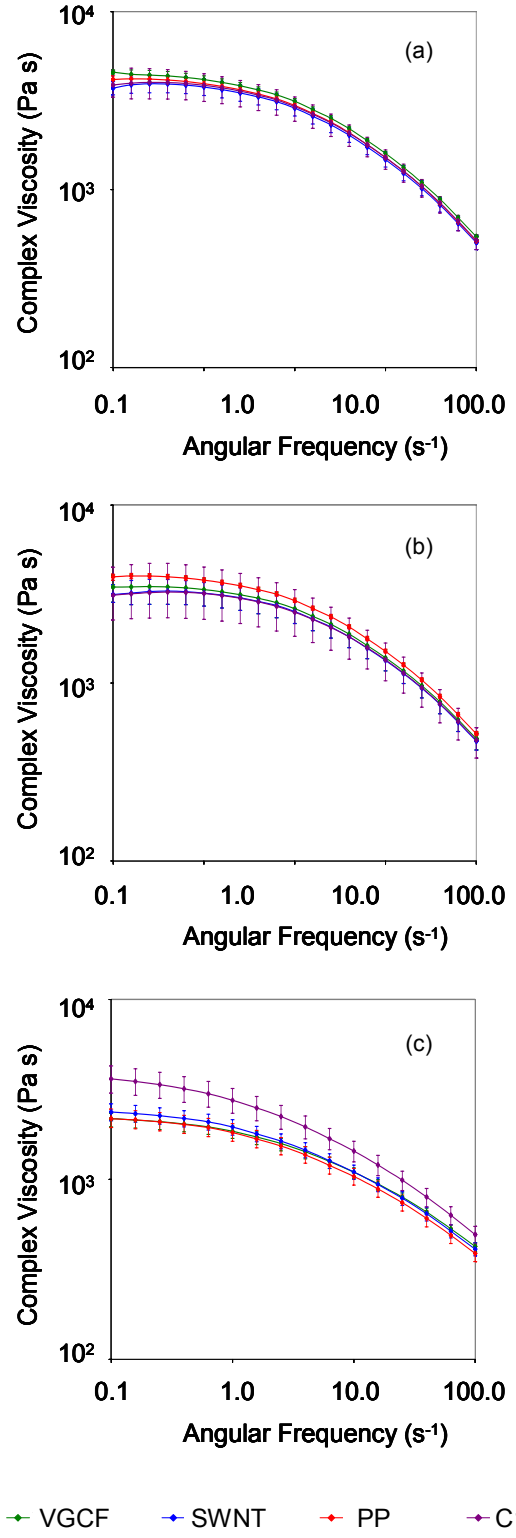

Figure 5.3. Complex viscosity of PP nanocomposites extruded at (a) 190 ^{o}C, 30 rpm, 8 min (b) 210 ^{o}C, 55 rpm, 14 min (c) 230 ^{o}C, 80 rpm, 20 min.

5.2 Conclusion

The design did not provide any significant information as there were very little difference in properties of the nanocomposites. The results were mostly within the margin of error. The work reinforced the fact that simply dry mixing nanomaterials with polypropylene did not provide initial mixing that was sufficient to enable well dispersed composites after melt extrusion in the Haake Minilab. The investigation provided information on the effect of functionalization and showed that functionalizing the nanotubes did in fact promote dispersion in the dry mixed samples. The dispersion attained is, however, dependant on the processing conditions employed. The results also led to the realization that the processing conditions range investigated may have been too limited. Increasing the range of melt extrusion temperature, speed, and time employed would provide much deeper insight into the effects of processing conditions on the properties of the resulting nanocomposites

Chapter 6

The Effect of Melt Extrusion Process Parameters on Hot Coagulated Polypropylene Nanocomposites

The investigation presented in Chapter 4 revealed that the hot coagulation (HC) method resulted in spectacular distribution of the nanomaterials in PP. This chapter seeks to investigate the effect of melt extrusion processing conditions on the properties of PP nanocomposites initially mixed by the hot coagulation method. 1% vol. SWNTs, C12SWNTs, or VGCF were incorporated into PP using the HC method in 1, 2-dichlorobenzene, followed by melt extrusion. A detailed explanation of the materials and procedures employed in this investigation is provided in Section 3.3.3. As in Chapter 5, a design of experiments (DOE) approach was used to elucidate the effects of nanomaterial type, extrusion temperature, screw speed, and recirculation time on nanocomposite thermal properties and stability. A drawback to the investigation in Chapter 5 was the rather limited range of processing conditions explored. To garner better insight into the effects of the processing conditions, a wider range of melt extrusion conditions has was investigated. The results were considered in terms of fraction of polymer stabilized in the interphase region, polymer degradation, and changes in the dispersion structure with processing. A key finding from this work was that the optimum processing conditions for a particular property were highly material dependent, and that interaction between

processing parameters such as time, extrusion temperature and screw speed had enormous effect on the properties.

6.1 $C_{12}H_{25}$ Functionalization and Selection of Sonication Time

The presence of dodecyl groups on the sidewalls of C12SWNTs was confirmed by Raman spectroscopy and thermal gravimetric analysis (TGA); approximately one in every 30 carbon atoms was functionalized with a $C_{12}H_{25}$ chain. The variation in the degree of functionalization from that gained earlier is normal and expected due to variation in the batch of SWNTs used.

As stated in the experimental section, sonication times of the nanomaterials were chosen so as to achieve similar aspect ratios for the SWNTs and C12SWNTs, and a dispersion of primarily individual VGCFs. The nanomaterials were sonicated in 1, 2-dichlorobenzene for 5 min, 30 min, 1 h, 2 h, 6 h, and 24 h. AFM analysis of drop dried samples of the sonicated dispersions was performed to investigate nanomaterial dispersion status and measure nanofibers or nanotube individual/bundle size. A sonication time of 30 min for VGCF, 6 h for C12SWNTs, and 24 h for SWNT resulted in the required aspect ratios. The histogram of the aspect ratios of measured entities, and the length, diameter, and aspect ratio of the nanomaterials are shown in Figures 6.1, 6.2, and 6.3, and Table 6.1.

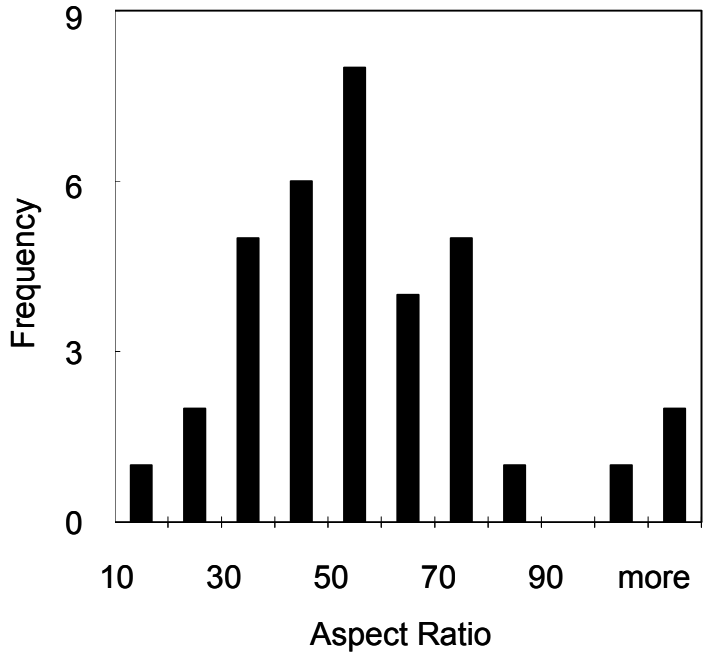

Figure 6.1. Aspect Ratio of VGCF after 30 min sonication.

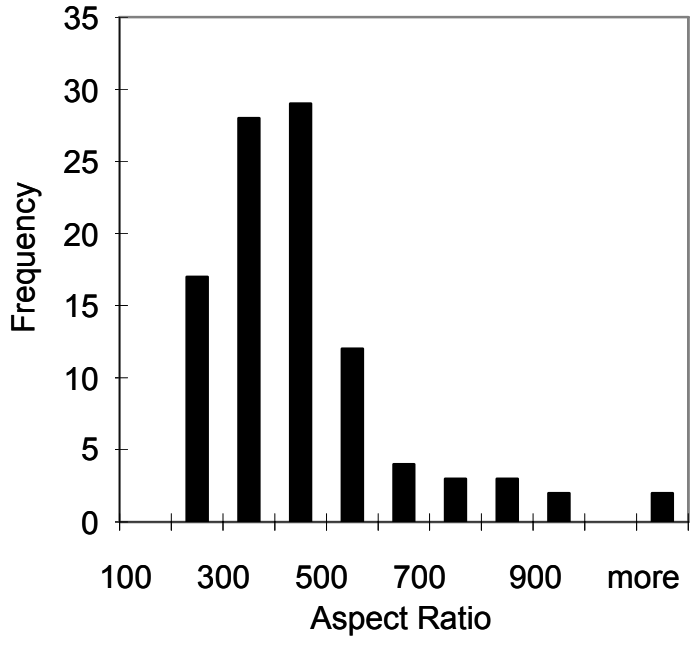

Figure 6.2. Aspect Ratio of C12SWNT after 6 h sonication.

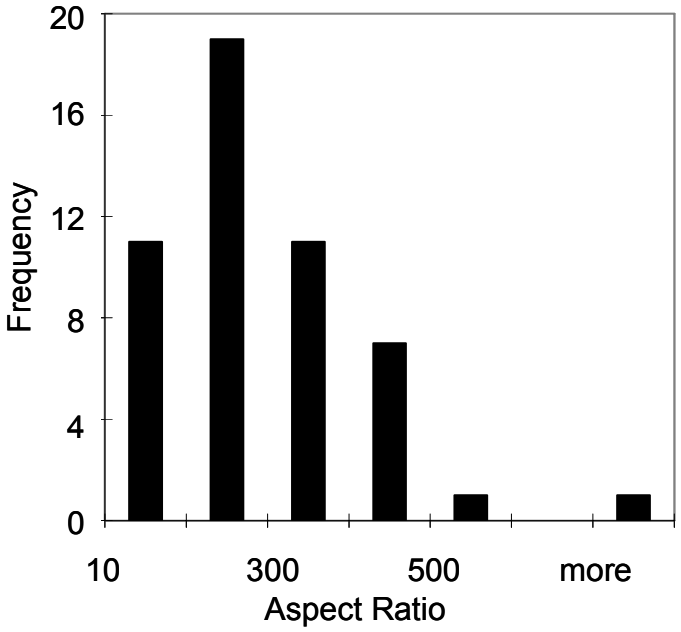

Figure 6.3. Aspect Ratio of SWNT after 24 h sonication.

Material	Sonication Time (hr)	Length (nm)	Dia. (nm)	Aspect Ratio
SWNT	24.0	798	4.3	200
C12SWNT	6.0	727	2.3	320
VGCF	0.5	4270	93	50

Table 6.1. Average length, diameter and aspect ratio of nanomaterials after sonication in DCB; 100 entities were measured for each sample.

6.2 Hot Coagulation of Pure Polypropylene

Preliminary investigations into hot coagulation of pure PP revealed degradation visualized by yellowing of the resulting processed polymer. Rheological comparison of pure PP and DCB processed PP (Figures 6.4 and 6.5), both extruded at 250 ^{o}C, 100 rpm, for 10 min, showed a decrease in the complex viscosity and storage modulus of DCB processed PP, further demonstrating the degradation resulting from the hot coagulation process alone.

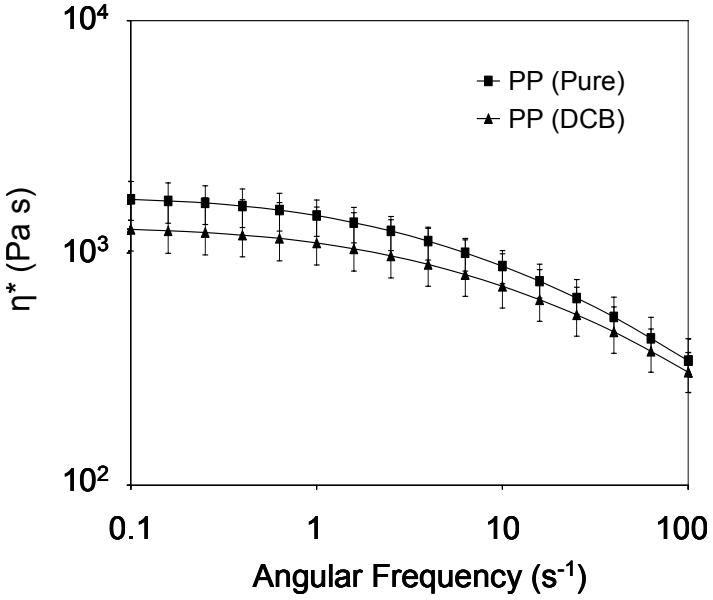

Figure 6.4. Complex viscosity of Pure PP and DCB processed PP

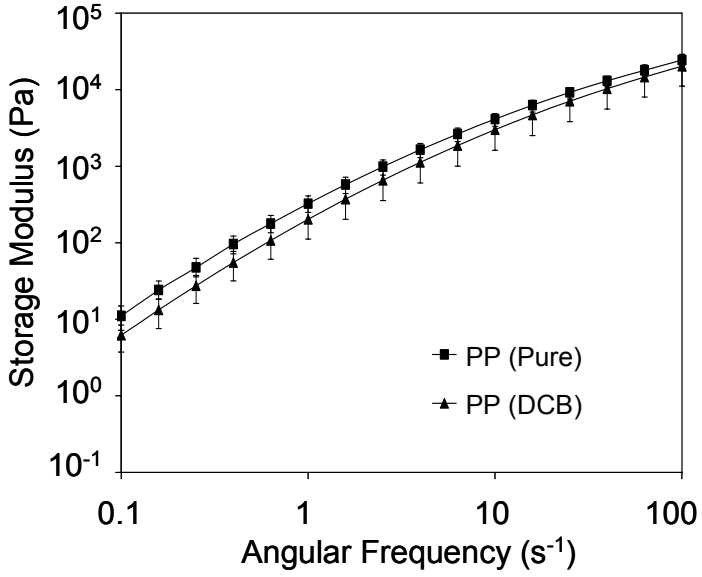

Figure 6.5. Storage modulus of pure PP and DCB processed PP.

6.3 Experimental Design and Model

The factors considered in the design included extrusion temperature (*T*) of 190 ^{o}C and 250 ^{o}C, extrusion speed (*n*) of 10 and 100 rpm, extrusion time (*t*) of 10 and 240 min, and nanomaterial type (*M*) of VGCFs, SWNTs, and C12SWNTs. Table 6.2 shows the design generated models for the decomposition, melt, and crystallization temperature of each nanocomposite type as a function of *T*, *n*, and *t*.

In order to further understand the effects of processing conditions on nanomaterial dispersion, and consequently the composites' thermal properties, a subset of the processing conditions that included the corner points of the design at a constant speed of 10 rpm were further characterized to measure the half time for crystallization ($t_{1/2}$) and activation energy for crystallization (ΔE_{ac}); their experimental data are included in Table

6.3. The effect of processing on each of the response variables is discussed in detail in the following sections.

T = Temperature (^{o}C), n = Screw Speed (rpm), t = Time (min)		
Decomposition Temperature T_d (^{o}C)	SWNT	$T_d = 467.05 - 0.102*T - 0.0059*n - 0.0069*t - 7.76E\text{-}04*n*t$
	C12SWNT	$T_d = 400.51 + 0.11*T - 0.0059*n - 0.038*t - 7.76E\text{-}04*n*t$
	VGCF	$T_d = 426.52 - 0.039*T - 0.0059*n - 0.092*t - 7.76E\text{-}04*n*t$
Melt Temperature T_m (^{o}C)	SWNT	$T_m = 167.45 - 0.024*n - 1.21E\text{-}03*t$
	C12SWNT	$T_m = 166.15 - 0.024*n - 3.61E\text{-}04*t$
	VGCF	$T_m = 165.08 - 0.024*n - 0.022*t$
Crystallization Temperature T_c (^{o}C)	SWNT	$T_c = 126.08 + 0.013*T + 0.026*t - 1.11E\text{-}04*T*t$
	C12SWNT	$T_c = 122.72 + 0.013*T + 0.025*t - 1.11E\text{-}04*T*t$
	VGCF	$T_c = 118.87 + 0.013*T + 0.011*t - 1.11E\text{-}04*T*t$

Table 6.2. Design generated model of response variables.

Sample	T_d (°C)	T_m (°C)	T_c (°C)	$t_{1/2}$ (s) (at 128 °C)	$\Delta E_{a,c}$ (kJ/mol)
Extrusion Conditions: 190 °C, 10 rpm, 10 min					
SWNT	445	168	129	22	166
C12SWNT	421	162	124	86	376
VGCF	421	165	120	140	305
PP	401	163	119	137	245
Extrusion Conditions: 190 °C, 10 rpm, 240 min					
SWNT	448	168	129	19	229
C12SWNT	407	167	125	26	329
VGCF	395	158	120	154	303
PP	401	162	115	355	278
Extrusion Conditions: 250 °C, 10 rpm, 10 min					
SWNT	444	166	129	22	174
C12SWNT	425	166	126	33	285
VGCF	416	165	122	130	282
PP	392	164	113	535	314
Extrusion Conditions: 250 °C, 10 rpm, 240 min					
SWNT	432	165	129	24	187
C12SWNT	417	165	125	30	320
VGCF	400	161	117	161	317
PP	356	151	113	1950	354

Table 6.3. Representative thermal properties of nanocomposites at a screw speed of 10 rpm. Measurement error was found to be ± 1.5 °C for T_d, ± 1 °C for T_m and T_c, and ± 5 kJ/mol for ΔE_{ac}.

6.4 Thermal Decomposition Temperature (T_d)

Analysis of variance (ANOVA) of the T_d data for all 36 runs in the DOE isolated the nanomaterial and processing factors that had a statistically significant effect on the thermal decomposition temperature (Table 6.4). Factors and interactions with $p < 0.05$ were deemed significant and were included in the predictive models for T_d given in Table 6.2. The Model F-value of 71.6 ($p < 0.0001$) indicated that the model was significant and that there was only a 0.01% chance the variation associated with the changing of the control factor could occur due to experimental noise. An $R^2 = 0.966$ indicated that the

model explained 96.6% of the total variation observed in T_d. The coefficient of variability (C.V.), a measure of the relative amount of unexplained variation present, was 1.02; confirming that the T_d model had a high predictive value for this data set. A comparison between the experimental data and the model predicted data showed good agreement between the data sets (Figure 6.6). The percentage contributions of the process factors on the final T_d value were calculated as the ratio of the individual sum of squares of the process factors to the total sum of squares. It was found that the nanomaterial used had the most significant effect with a contribution of 63% towards the final T_d value while extrusion time had a 21% contribution. Other factors, such as screw speed, and interactions between extruder temperature and nanomaterial, screw speed and time, and time and nanomaterial, had smaller, albeit statistically significant, effects.

All nanocomposites had higher thermal decomposition temperatures than equivalently processed PP. The models for T_d, shown in Table 6.2, can be better visualized by the interaction plots shown in Figure 6.7; for reference, experimental data for the composites and polypropylene also are included. The effect of processing on T_d can be explained by changes in polymer molecular weight and dispersion microstructure. As expected for polymers that can undergo free radical thermal decomposition (153), the T_d of PP was strongly dependent on the extent of degradation during extrusion and tended to be lowered by higher temperatures, longer times, and higher screw speeds. Incorporation of nanomaterials can increase T_d in two ways: first, by stabilizing polymer chains in the interphase region against degradation, and/or second, by forming a percolated SWNT network that hinders thermal decomposition by slowing the transport of evolved decomposition products (149,154).

Decomposition Temperature, T_d

Source	Sum of Squares	DF	Mean Square	F Value	Prob > F
Model	13071.27	10	1307.13	71.54	< 0.0001
Extrusion Temp (*T*)	1.81	1	1.08	0.10	0.7556
Screw Speed (*n*)	652.10	1	652.10	35.69	< 0.0001
Extrusion Time (*t*)	2847.70	1	2847.70	55.87	< 0.0001
Nanomaterial (*M*)	8460.64	2	4230.32	231.55	< 0.0001
TM Interaction	205.24	2	102.62	5.62	0.0097
nt Interaction	425.26	1	425.26	23.28	< 0.0001
tM Interaction	480.36	2	240.18	13.15	0.0001
Residual	456.75	25	18.27		
Cor. Total	13528.02	35			

Std. Dev. 4.27 Mean 419.11 R^2 0.966 Coeff. Of Var. 1.02

Melt Temperature, T_m

Source	Sum of Squares	DF	Mean Square	F Value	Prob > F
Model	250.99	6	41.83	18.69	< 0.0001
Screw Speed (*n*)	34.76	1	34.76	15.53	0.0005
Extrusion Time (*t*)	24.26	1	24.26	10.84	0.0026
Nanomaterial (*M*)	153.72	2	76.86	34.34	< 0.0001
tM Interaction	40.67	2	20.34	9.09	0.0009
Residual	64.91	29	2.24		
Cor. Total	315.91	35			

Std. Dev. 1.50 Mean 164.06 R^2 0.794 Coeff. Of Var. 0.912

Crystallization Temperature, T_c

Source	Sum of Squares	DF	Mean Square	F Value	Prob > F
Model	509.13	7	72.73	89.82	< 0.0001
Extrusion Temp (*T*)	0.02	1	0.02	0.03	0.8729
Extrusion Time (*t*)	5.57	1	5.57	6.87	0.0140
Nanomaterial (*M*)	458.94	2	229.47	283.39	< 0.0001
Tt Interaction	3.84	1	3.84	4.74	0.0380
tM Interaction	17.44	2	8.72	10.77	0.0003
Residual	22.67	28	0.81		
Cor. Total	531.80	35			

Std. Dev. 0.90 Mean 124.96 R^2 0.957 Coeff. Of Var. 0.72

Table 6.4. Analysis of variance

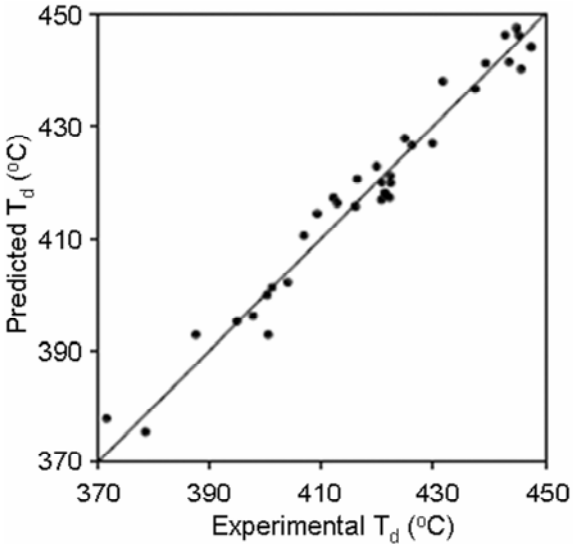

Figure 6.6. Model predicted decomposition temperature values compared to experimental decomposition temperature values.

For PP/SWNT, T_d was both much higher and less dependent on processing conditions than PP. For example, as shown in Table 6.3, for nanocomposites extruded at a screw speed of 10 rpm T_d(PP/SWNT) = 440 ± 8 °C while T_d(PP) = 378 +/- 23 °C. These results compared to a 32 °C increase in T_d obtained by Marosföi et al. (2006) after the addition of 3 % vol. multi-walled carbon nanotubes to PP at a fixed processing condition (149). Based on SEM after extrusion at 190 °C, 10 rpm, 10 min, the SWNTs were dispersed as bundles on the order of D ~ 20 nm. If the thickness of the interfacial shell of stabilized chains was on the order of the radius of gyration of the polymer (155) the majority of the polymer was in the stabilized interphase region. In fact, efforts to perform rheological characterization of 1% vol. PP/SWNT failed because the network was so stiff that the material could not flow uniformly even at elevated temperatures.

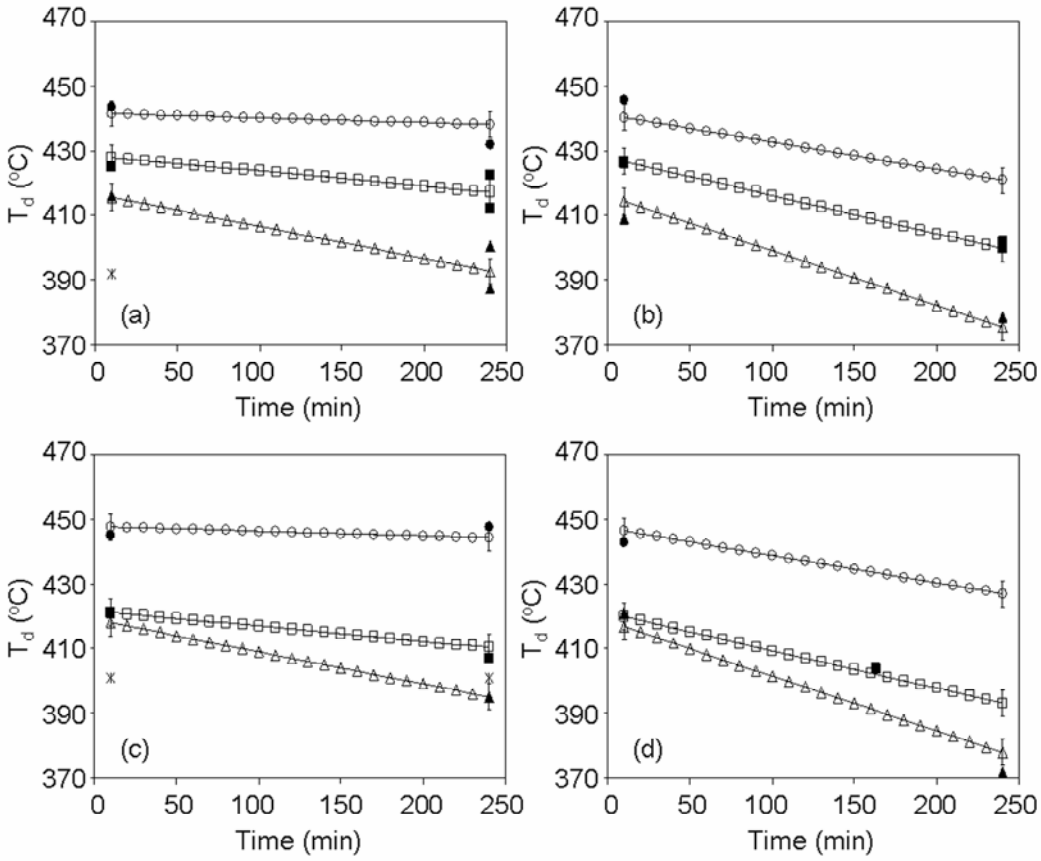

Figure 6.7. Model generated interaction plots of decomposition temperature at (a) 250 °C and 10 rpm, (b) 250 °C and 100 rpm, (c) 190 °C and 10 rpm, and (d) 190 °C and 100 rpm. Open circles, squares and triangles are PP/SWNT, PP/C12SWNT, and PP/VGCF respectively. Closed symbols are experimental data and asterisks are reference values for the hot coagulated and extruded polypropylene.

In order to study their rheology, PP/SWNT samples were diluted to 0.25 % vol. SWNT by re-extruding them at a fixed processing condition of 190 °C, 55 rpm, and 10 min. While this approach prohibited direct rheological comparison to PP/C12SWNT and PP/VGCF, it provided an indication of the relative effects of processing on PP/SWNT samples. Figure 6.8 shows the complex viscosity η^* as a function of angular frequency ω for the conditions shown in Table 6.3. For the diluted PP/SWNT

nanocomposites that were characterized rheologically, the T_d was observed to generally trend with low frequency complex viscosity. Complex viscosity is dependent on both nanomaterial dispersion and polymer degradation; increased degradation (or decreased polymer molecular weight) will lower viscosity while improved nanomaterial dispersion will increase it. At an extrusion temperature of 190 ^{o}C, the viscosity of samples initially extruded for 10 min was lower than samples initially extruded for 240 min (Figure 6.8). This result was due to improved SWNT dispersion with time. Nanotube distribution was evaluated using optical microscopy and Raman mapping (Figures 6.9 and 6.10) as well as the shear stress recorded during extrusion. Within a given sample, the relative Raman G-band intensity is a function of nanotube concentration; higher intensity indicates higher localized SWNT concentration. The Raman intensity maps provided a clear visualization of the differences between composite distributions; the data was quantified in terms of the standard deviation of the G-band intensities ($\sigma(G)$) in 20 X 20 μm^2 maps (138). The nanotube distributions for samples extruded at 190 ^{o}C and 10 rpm were equivalent after 10 and 240 min of extrusion with $\sigma(G) \sim 8$. However, continuous measurements of shear stress in the extruder's recirculation channel showed that at 10 min the shear stress was still increasing; a steady state dispersion microstructure had not been reached (Figure 6.11). In contrast, for the sample extruded at 240 min, a plateau in the shear stress profile was reached after 20 min, and a second jump in shear stress occurred at approximately 140 min followed by a second plateau at a 10% higher shear stress. These results are consistent with other authors' observations of both a critical stress and a critical mixing time to achieve a uniform dispersion of nanomaterials in polymers (122,156). Therefore, the higher viscosity at long extrusion time can be attributed to improved dispersion with

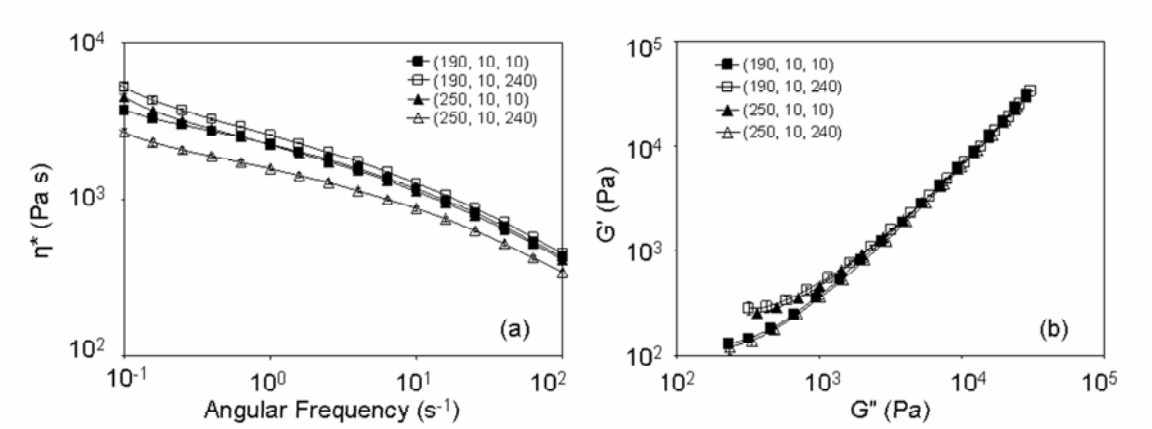

Figure 6.8. (a) Complex viscosity, and (b) Cole-Cole plot of PP/SWNT diluted to 0.25 % vol. The numbers in the legend correspond to extrusion temperature (^{o}C), speed (rpm), and time (min) respectively.

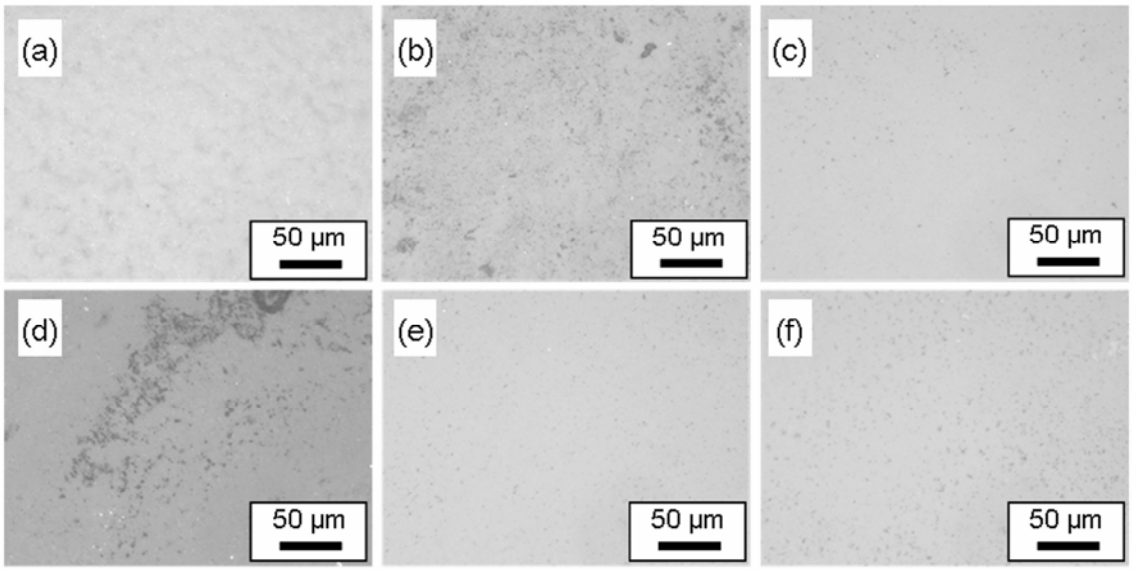

Figure 6.9. Optical microscopy images of (a, b, c) PP/VGCF, PP/C12SWNT, and PP/SWNT processed at 190 ^{o}C, 10 rpm, 10 min, and (d, e, f) PP/VGCF, PP/C12SWNT, and PP/SWNT processed at 190 ^{o}C, 10 rpm, 240 min. Scale bars on all images are 50 µm.

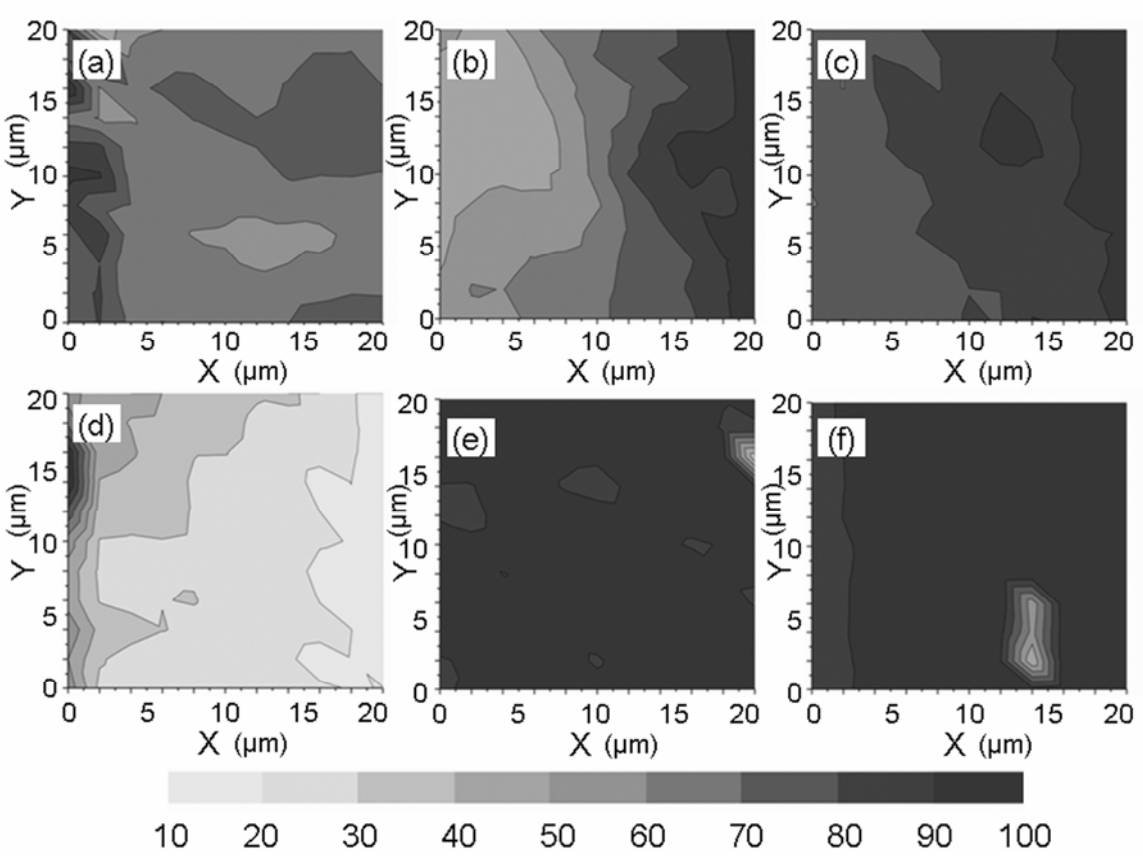

Figure 6.10. Raman map of (a, b, c) PP/VGCF, PP/C12SWNT, and PP/SWNT processed at 190 ^{o}C, 10 rpm, 10 min, and (d, e, f) PP/VGCF, PP/C12SWNT, and PP/SWNT processed at 190 ^{o}C, 10 rpm, 240 min.

time. The Cole-Cole plot in Figure 6.8b further confirms that for samples processed at 190^{o} C, the microstructure was more complex in the samples initially extruded for 240 min.

In contrast, for samples initially extruded at 250 ^{o}C, the viscosity of samples initially extruded for 10 min was higher than those extruded for 240 min (Figure 6.8a). While even at 250 ^{o}C the shear stress during extrusion had not reached steady state in 10 min, the higher temperature and accompanying lower polymer matrix viscosity most likely facilitated faster dispersion than at an extrusion temperature of 190 ^{o}C. On the

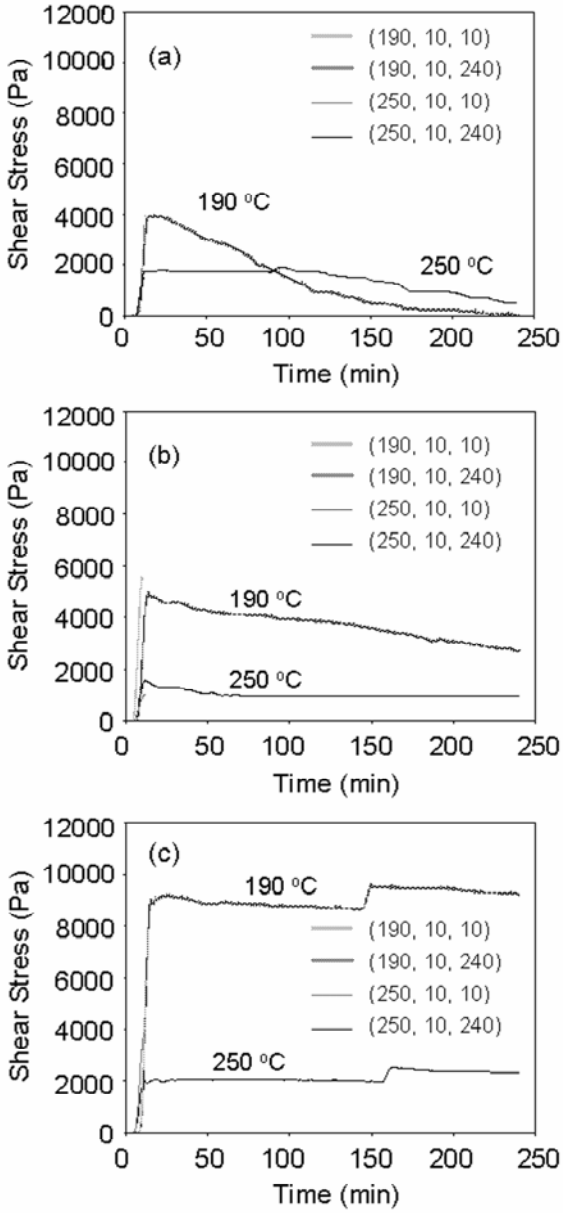

Figure 6.11. Shear stress during low speed extrusion (10 rpm) of (a) PP/VGCF, (b) PP/C12SWNT, and (c) PP/SWNT. The numbers in the legend correspond to extrusion temperature (^{o}C), speed (rpm), and time (min) respectively. The shear stress profiles of the 10 min extrusion overlay the 240 min extrusion, at the same extrusion temperature.

other hand, at long times, even though shear stress did increase at t > 150 min, the lower matrix viscosity allowed eventual nanotube reaggregation over the extended extrusion period. This is supported by the gradual decrease in intensities of regions evident in the Raman map of PP/SWNT processed at 250 ^{o}C (Figure 6.12); (σ(G)) = 7.8 at 10 min and 9.0 at 240 min. Thus, the marginal increase in T_d with extrusion time for samples extruded at 190 ^{o}C and 10 rpm can be attributed improved dispersion. However, for samples extruded at 250 ^{o}C dispersion becomes worse at long times, resulting in fewer stabilized chains in the interphase and a decrease in T_d.

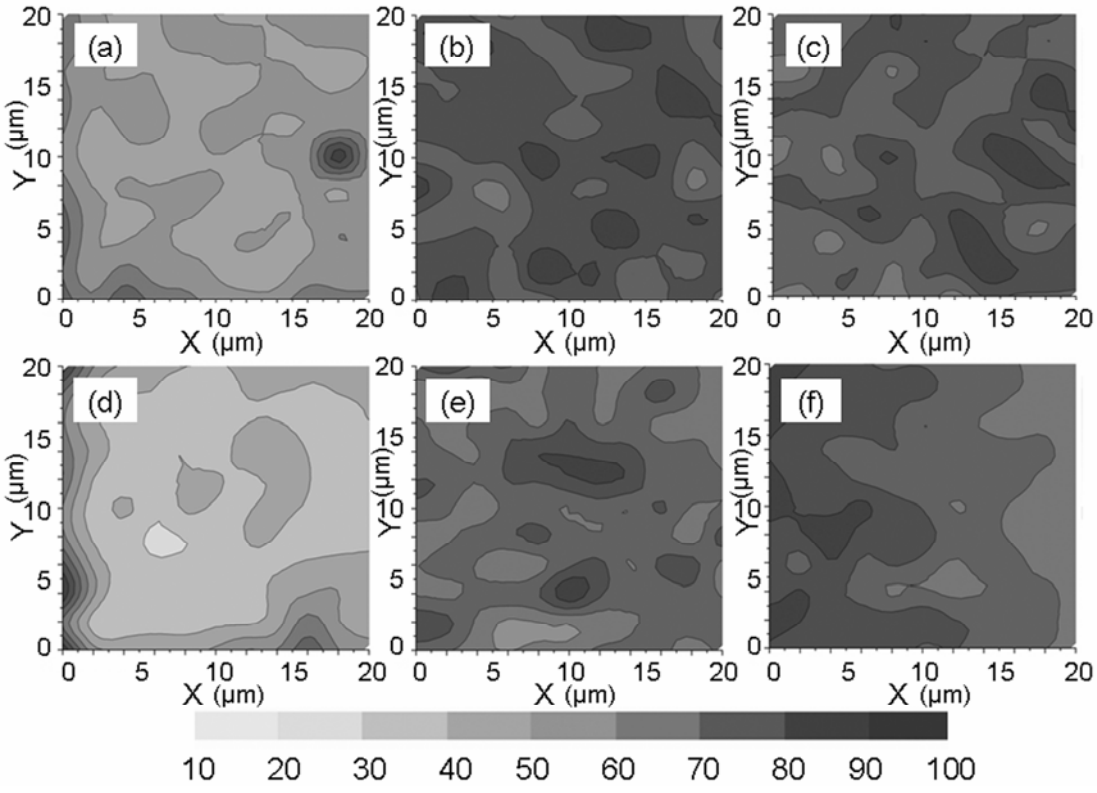

Figure 6.12. Raman map of (a, b, c) PP/VGCF, PP/C12SWNT, and PP/SWNT processed at 250 ^{o}C, 10 rpm, 10 min, and (d, e, f) PP/VGCF, PP/C12SWNT, and PP/SWNT processed at 250 ^{o}C, 10 rpm, 240 min.

As shown by the model in Table 6.2, the interaction of screw speed, n, and time, t, also affected T_d; reductions in T_d with time were more pronounced at higher screw speeds. This reduction was fairly insignificant at short times. For example, at T = 190 ^oC and t = 10 min, the predicted T_d was 447 ^oC at n = 10 rpm and the predicted T_d was 446 ^oC at n = 100 rpm (Figure 6.7). However, after 240 min of extrusion at 100 rpm the predicted T_d decreased to 427 ^oC. These results indicate that high extrusion screw speed, especially in combination with a high extrusion temperature or extrusion time, is not always necessary and, in fact, can be detrimental to thermal stability. A gradual decrease in the shear stress profile during extrusion of PP/SWNTs processed at high speeds and long times also was observed (Figure 6.13), and was attributed to polypropylene degradation and SWNT reaggregation. For PP/SWNTs processed at 190 ^oC, 100 rpm, and 240 min, the Raman maps indicated an even distribution of SWNTs with $\sigma(G) \sim 8$ (Figure 6.14). However, for PP/SWNTs processed at 230 ^oC, 100 rpm, and 240 min, $\sigma(G) \sim 12$, indicating a more uneven SWNT distribution, possibly resulting from severe polypropylene degradation at the higher extrusion temperature and speed.

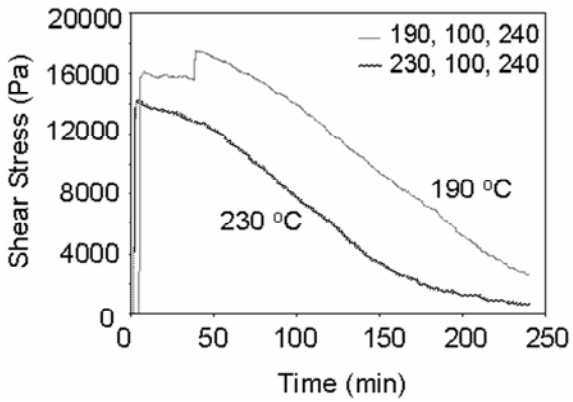

Figure 6.13. Shear stress during extrusion of PP/SWNT processed at 190 ^oC, 100 rpm, 240 min, and 230 ^oC, 100 rpm, 240 min.

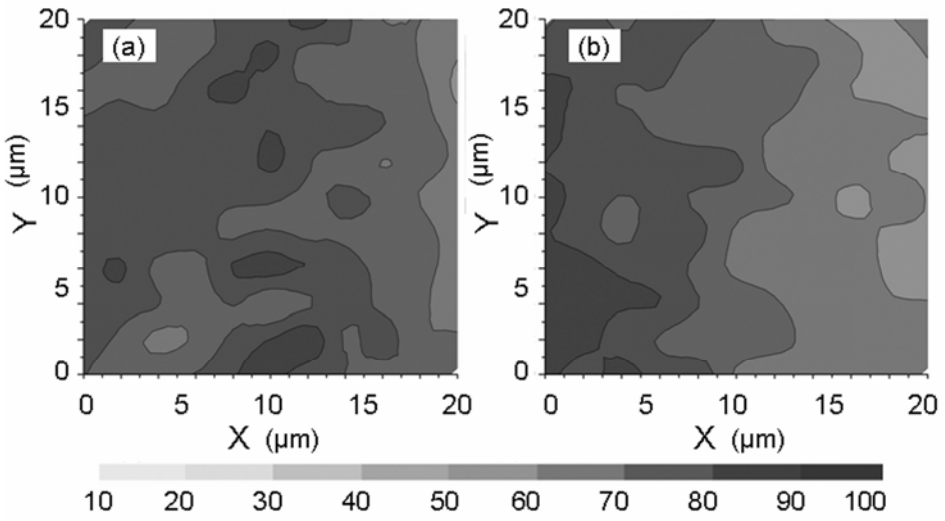

Figure 6.14. Raman map of PP/SWNT processed at 190 ^{o}C, 100 rpm, 240 min, and 230 ^{o}C, 100 rpm, 240 min.

In contrast to PP/SWNT, the thermal stabilities of PP/C12SWNT and PP/VGCF were more strongly dependent on processing conditions employed. As shown by the model (Table 6.2), both the effects of screw speed and the interaction between screw speed and time were the same for both PP/C12SWNT and PP/VGCF. However, the T_d of the PP/C12SWNT was affected more significantly by extrusion temperature, while the T_d of the PP/VGCF was more strongly dependent on extrusion time. The fact that PP/C12SWNT and PP/VGCF were more strongly, and differently, affected by processing parameters than PP/SWNT suggests there were differences in the origin of the thermal stability enhancement for each system. The T_d of PP/C12SWNT was significantly lower than that of PP/SWNT at all conditions. This is counterintuitive since the C12SWNT should facilitate better dispersion and interaction with the polymer matrix. Comparisons of C12SWNT and SWNT in PP using different techniques for introducing the nanomaterial and polymer also showed poorer dispersion in C12SWNT/PP, but did not

probe the effects of processing (138). C12SWNT/PP, however, did show improved dispersion with varying processing conditions when initially mixed by dry mixing. While the reason for the mostly poorer dispersion of C12SWNTs is unclear, it was speculated that the presence of residual lithium from the functionalization reaction and sonication in DCB may have led to the formation of lithium chloride salts and catalyzed the free radical degradation of the polymer backbone (157).

The effect of extrusion time on the T_d of PP/C12SWNT was nearly an order of magnitude greater than for PP/SWNT. Interestingly, higher temperatures resulted in higher T_d for C12SWNTs. The fact that T_d increased with increasing extrusion temperature suggests that higher thermal energy, and lower initial polymer matrix viscosity, at elevated temperatures enabled enhanced dispersion of the functionalized nanotubes in the polymer matrix and improved interfacial interactions between the polymer chains and the C12 groups. Rheological characterization supported this hypothesis. Assuming equivalent dispersion, the viscosity of the PP/C12SWNT processed 10 rpm for 240 min at 250 ^{o}C should have been lower than that processed at 190 ^{o}C due to increased polymer degradation. The fact that these viscosities were nearly equivalent (Figure 6.15) implied better dispersion at higher temperature and long extrusion time.

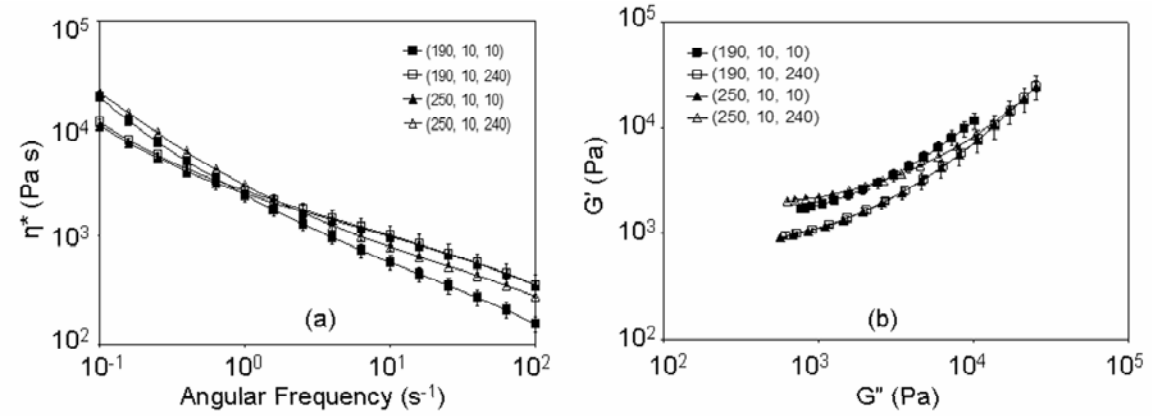

Figure 6.15. (a) Complex viscosity, and (b) Cole-Cole plot of PP/C12SWNT. The numbers in the legend correspond to extrusion temperature (°C), speed (rpm), and time (min) respectively.

As with the PP/SWNT, the shear stress profile (Figure 6.11b) showed that 10 min was insufficient to reach a steady state dispersion microstructure for PP/C12SWNT at 190 °C and 10 rpm. In addition, optical microscopy (Figure 6.9) clearly showed that samples processed for 240 min had fewer large aggregates than those processed for 10 min. Raman Mapping of PP/C12SWNT processed at 190 °C, 10 rpm, and 10 min resulted in σ(G) of ~ 17; twice as high as that for equivalently processed SWNT. This means that there was significantly less polymer stabilized in the interphase during the first 10 minutes of extrusion, and explains the lower T_d compared to equivalently processed PP/SWNT. For PP/C12SWNT processed at the same temperature and speed but a longer time of 240 min, σ(G) ~ 6 was similar to that obtained for SWNTs. However, after reaching a plateau value of shear stress at approximately 25 min into extrusion, much sooner than for SWNTs, the shear stress steadily decreased; indicating ongoing polymer degradation, possibly due to free radicals formed prior to achieving better dispersion. Although the C12SWNTs were better dispersed after 240 min

compared to 10 min, the complex viscosity (Figure 6.15a) and T_d (Table 6.3) decreased due to the presence of degraded polypropylene in the final nanocomposite. In contrast, at 250 ^oC, while the shear stress had not reached a steady state at 10 min, over long times the shear stress, while displaying an initial decrease, remained fairly constant after ~ 75 min into extrusion. At the higher temperature, the lower matrix viscosity resulted in more facile dispersion and less shear degradation of the polymer chains. The initial drop in the polymer molecular weight, as implied by the drop in shear stress during extrusion (Figure 6.11b), in conjunction with Raman mapping showing similar dispersion (Figure 6.12) accounted for the 8 ^oC decrease in T_d for PP/C12SWNT processed at 250 ^oC, 10 rpm, and 240 min ($\sigma(G) \sim 8$) compared to that processed for 10 min ($\sigma(G) \sim 7$). The Cole-Cole plot (Figure 6.15b) highlights the less complex nature of the microstructures of PP/C12SWNTs processed at 190 ^oC, 10 rpm, and 240 min, and 250 ^oC, 10 rpm, and 10 min compared to the other samples confirming that both extrusion time and extrusion temperature affected the microstructure.

The T_d of the PP/VGCF was affected more strongly by extrusion time than the other materials. This is easily seen in both the model (Table 6.2) and the interaction plot (Figure 6.7), where the T_d of PP/VGCF decreased rapidly with increasing extrusion time, particularly at higher screw speed. Optical microscopy and Raman mapping (Figures 6.9, 6.10, and 6.12) showed significant aggregation of VGCF with time. The $\sigma(G)$ of PP/VGCF processed at 190 ^oC, 10 rpm, and 10 min was 8 compared to 14 for that processed for 240 minutes. Similarly, for samples processed at 250 ^oC and 10 rpm, $\sigma(G) \sim 8$ after 10 min and $\sigma(G) \sim 13$ after 240 min of extrusion. Differences in viscosity and T_d with extrusion time were much greater at 190 ^oC than 250 ^oC due to the higher shear

stresses resulting from higher viscosity at lower temperature serving to both facilitate VGCF breakage and shear induced polymer degradation.

The strong time dependence can be explained in terms of the initial dimensions of the VGCFs and their friability. The friable nature of the VGCF was evidenced by the rapid decrease in length with sonication time, and also has been observed previously in polymer nanocomposite extrusion (158). If one assumes that the width of the interphase shell of stabilized PP chains is on the order of the radius of gyration R_g at a concentration of 1% vol. of VGCF, most of the chains are in the bulk polymer matrix and not the more stabilized interphase region. In addition, the initial dimensions of the VGCF were not sufficient to sustain a percolated network. The percolation threshold for rods $\phi_c \sim R/L$ (159). Thus, a concentration of 1% vol. is approximately the percolation threshold for VGCF, while it is 4 to 7 times higher than ϕ_c for the SWNTs and C12SWNTs. The concentration being so close to ϕ_c means that even a small reduction in aspect ratio would have resulted in loss of the percolated network. In fact, rheological measurements showed that in contrast to PP/SWNT and PP/C12SWNT none of the VGCF samples exhibited evidence of percolated networks; G′ was always dependent on frequency (Figure 6.16). While PP/VGCF processed at 250 ^oC, 10 rpm, and 240 min showed a slight deviation in slope at low frequency, the other samples had slopes of $G' \propto \omega^1$ compared to $G' \propto \omega^{1.3}$ for terminal behavior of plain PP. The complex viscosity of PP/VGCF, Figure 6.17a, trended with T_d. The Cole-Cole plot, in Figure 6.17b, confirmed that the PP/VGCF samples processed for only 10 min had a more complex microstructure. This further highlights that, for friable materials such as VGCF, long processing times can be detrimental to both dispersion and thermal stability.

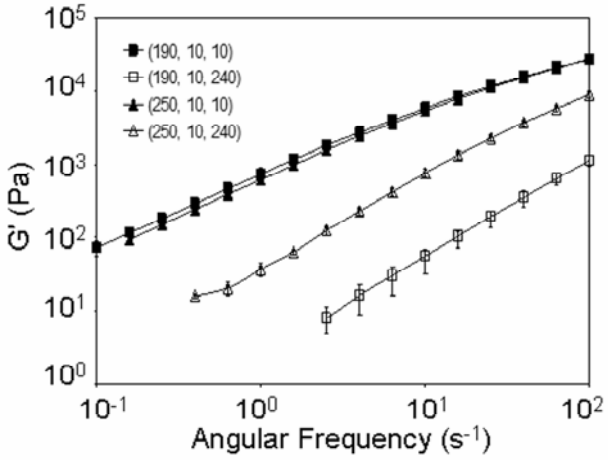

Figure 6.16. Storage modulus of PP/VGCF. The numbers in the legend correspond to extrusion temperature (°C), speed (rpm), and time (min) respectively.

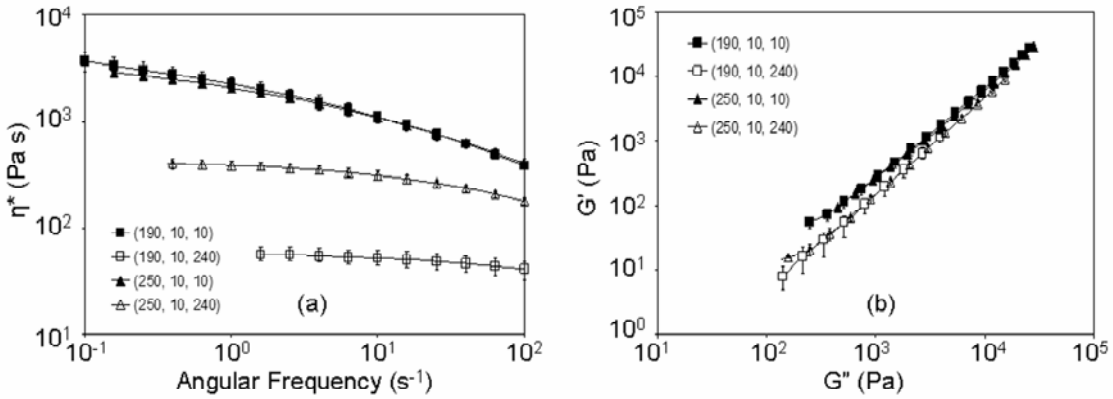

Figure 6.17. (a) Complex viscosity, and (b) Cole-Cole plot of PP/VGCF. The numbers in the legend correspond to extrusion temperature (°C), speed (rpm), and time (min) respectively.

To summarize, it was observed that the type of nanomaterial incorporated in the polymer matrix contributed the most towards the T_d of the final nanocomposite, while processing conditions had a smaller, although significant, effect. In addition, the T_d of

PP/SWNT was observed to be less dependent on processing conditions than PP/C12SWNT or PP/VGCF. At lower extrusion temperatures of 190 ^{o}C, T_d of PP/SWNT increased with processing time owing to better dispersion; while at higher extrusion temperatures of 250 ^{o}C, T_d decreased with time owing to lower matrix viscosity leading to SWNT reaggregation. In the case of PP/C12SWNTs, T_d was strongly affected by extrusion temperature and was observed to increase when processed at 250 ^{o}C. PP/VGCF, on the other hand, was strongly affected by extrusion time and was observed to rapidly decrease with processing time. The decomposition temperature of all nanocomposites was severely reduced when processed at high screw speeds for long time, again due to severe polymer degradation and nanomaterial reaggregation.

6.5 Melting Temperature

Analyses of melting temperature (T_m) data were performed in the same manner as for thermal decomposition (Table 6.4). The model for melt temperature is given in Table 6.2. The model had an F-value = 18.69 ($p < 0.0001$), and $R^2 = 0.794$. The relatively low R^2 can be attributed to the relatively small changes in T_m for the PP/SWNT and PP/C12SWNT compared to the measurement error of ± 1 ^{o}C. The type of nanomaterial integrated in the polymer had the most significant effect and contributed to 49% of the response observed. In contrast to the T_d data, the extrusion temperature, and the interaction of nanomaterial and extrusion temperature did not have a statistically significant effect on T_m. Screw speed and extrusion time had slight effects with contributions of 11 % and 8%, respectively. Figure 6.18 shows the interaction plots for the nanocomposite melt temperature. While the T_m of PP/SWNT and PP/C12SWNT

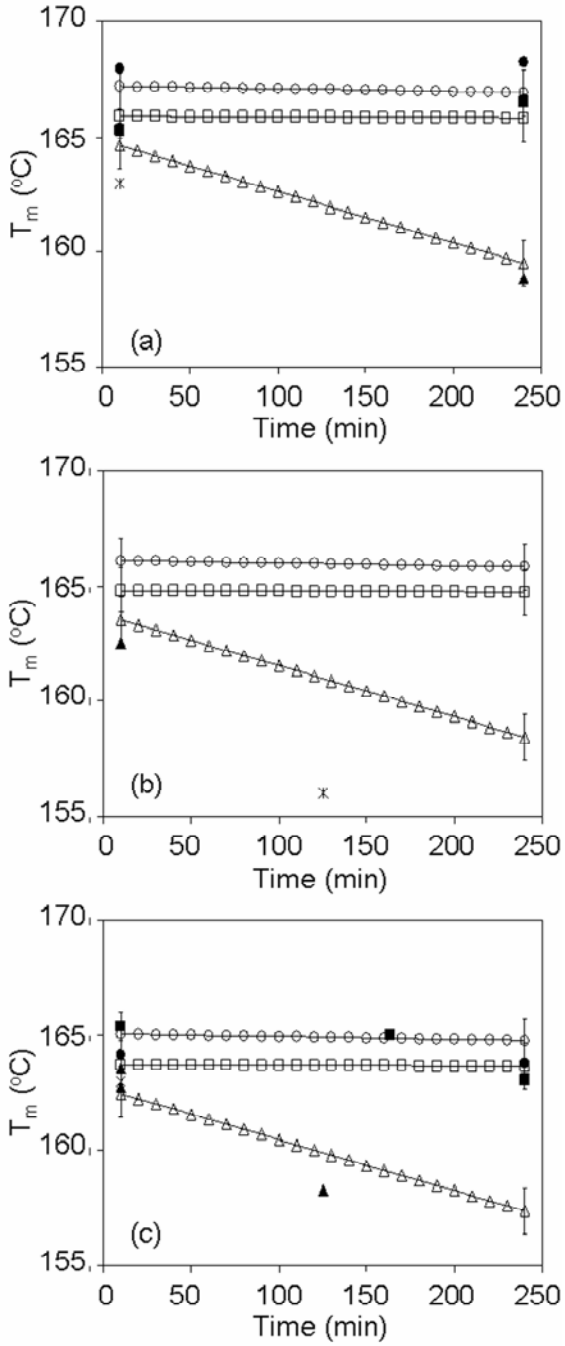

Figure 6.18. Model generated interaction plots of melt temperature at (a) 10 rpm, (b) 55 rpm, and (c) 100 rpm. Open circles, squares and triangles are PP/SWNT, PP/C12SWNT, and PP/VGCF respectively. Closed symbols are experimental data, and asterisks are reference values for the hot coagulated and extruded polypropylene.

stayed relatively unchanged over extended processing times, that of PP/VGCF decreased drastically with extrusion time, particularly at 190 ^{o}C. This response was similar to that observed for T_d and could again be attributed to the friability of the VGCF, higher shear stress at low temperature, reaggregation, and the lack of a percolated network. The relatively poor thermal stability imparted by VGCF to the composites allowed ongoing polymer degradation resulting in shorter, more mobile, polymer chains and a lower melt temperature.

6.6 Crystallization Temperature

Nanomaterials are known to increase polymer crystallization temperature T_c by providing heterogeneous nucleation sites (133,160). Consistent with previous works, all of the nanocomposites in this study exhibited higher values of T_c than PP; Bhattacharyya et al. (132) and Manchado et al. (78) both observed that the addition of only 0.5 % vol. SWNT to PP was sufficient to increase T_c considerably. The model for crystallization T_c is given in Table 6.2 (ANOVA in Table 6.4). The model was highly significant with an F-value = 89.82 ($p<0.0001$), and R^2 = 0.957. Since crystallization temperature is an intrinsic property, it is not surprising that the design showed that the type of nanomaterial contributed over 85% of the effect on the resulting T_c. There was a slight, but statistically significant, effect of time on T_c which, as in the case of T_d and T_m, was more significant for PP/VGCF (Figure 6.19). The combined influences of extrusion temperature and nanomaterial, and extrusion temperature and time also had significant effects on the nanocomposites crystallization temperature, but the effect of extrusion speed was not significant. The slightly lower values of T_c for PP/C12SWNT relative to

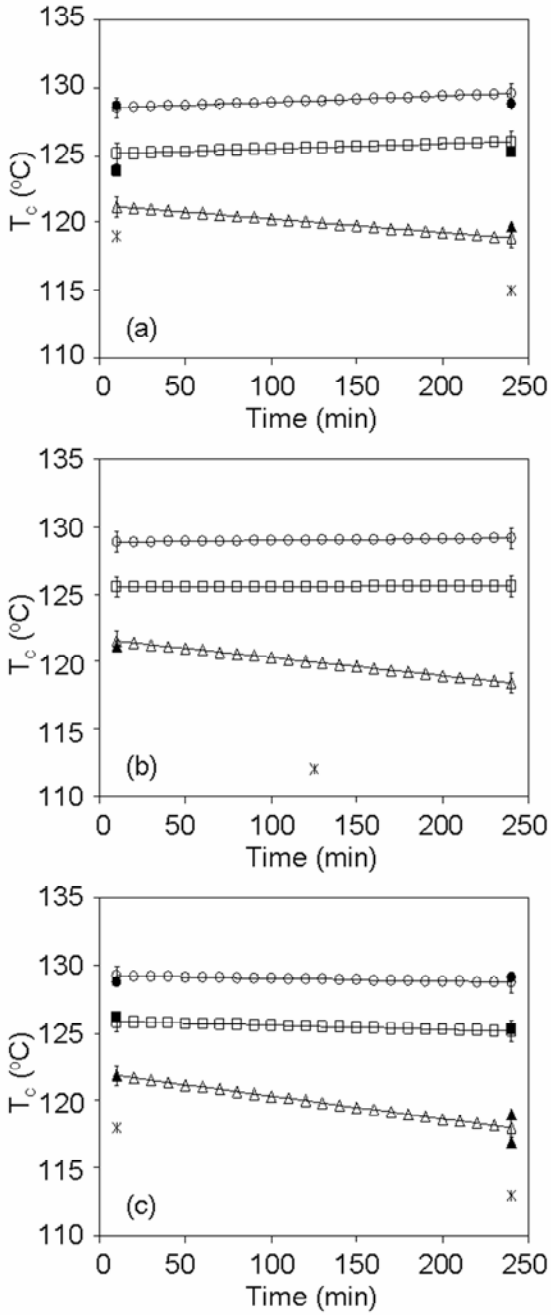

Figure 6.19. Model generated interaction plots of crystallization temperature at (a) 190 ^{o}C, (b) 220 ^{o}C, and (c) 250 ^{o}C. Open circles, squares and triangles are PP/SWNT, PP/C12SWNT, and PP/VGCF respectively. Closed symbols are experimental data, and asterisks are reference values for the hot coagulated and extruded polypropylene.

PP/SWNT processed at the same condition likely were due to a combination of poorer dispersion and the ligands on the C12SWNTs providing less favorable nucleation sites for crystallization. The even lower values of T_c for PP/VGCF were likely due to geometric effects. Due to the difference in size of the nanomaterials, a loading of 1% vol. resulted in a number fraction of VGCFs that was three orders of magnitude lower than for C12SWNT and SWNT. Even allowing for VCGCF breakage, this translated into fewer nucleation sites in the PP/VGCF nanocomposites. In addition, the reduction in polymer molecular weight resulting from the relatively low thermal and shear stability of the PP/VGCF composites also contributed to lower values of T_c compared to the other nanocomposites since lower molecular weight polymers tend to crystallize at a lower temperature (161).

The crystallization temperature data also showed some potential subtle effects from improved SWNT dispersion at longer extrusion time, and improved interaction between the C12SWNTs and the polymer at higher temperatures and longer times. To further explore these potential effects, the half times $t_{1/2}$ and activation energies for crystallization ΔE_{ac} of nanocomposites produced at 10 rpm were measured. The magnitude of $t_{1/2}$ was a function of both the crystallization kinetics and the total number of nucleation sites, while ΔE_{ac} only measured the energy barrier to crystallization. The crystallization kinetics were studied using the Avrami equation (134) .

Numerical values for $t_{1/2}$ for samples extruded at 10 rpm and 190 ^{o}C and 250 ^{o}C are listed in Table 6.3. Faster crystallization rates are indicated by lower crystallization half times. For PP samples fabricated at 10 rpm, $t_{1/2}$ ranged from 137 s after processing at 190 ^{o}C for 10 min to 1950 s after processing at 250 ^{o}C for 240 min at a T_c of 128 ^{o}C. The

large increase in $t_{1/2}$ was due to the significant decrease in PP molecular weight when processed at high temperature for long times and the lower driving force for crystallization of the resulting shorter chains. In contrast, since SWNTs imparted the most stability to the polymer and provided numerous nucleation sites, the PP/SWNT nanocomposites had the lowest values of $t_{1/2}$ at all processing conditions. In the case of the PP/C12SWNT, $t_{1/2}$ was higher than for PP/SWNT at short processing times. However, at longer processing time, $t_{1/2}$ for PP/C12SWNT decreased significantly becoming comparable to SWNT. This was attributed to the previously described enhanced dispersion of C12SWNTs in PP at longer extrusion times. The effect of the VGCF on $t_{1/2}$ was harder to discern. In all cases, $t_{1/2}$ for PP/VGCF was higher than for the other nanocomposites, presumably due to fewer nucleation sites and the lower average polymer molecular weight resulting from PP degradation. Interestingly, at 190 ^{o}C, $t_{1/2}$ for PP/VGCF was comparable to PP at 10 min; however it was much lower than PP at t = 240 min. At 250 ^{o}C, the $t_{1/2}$ of PP/VGCF was markedly lower than that of PP at both the short and long extrusion time. This is attributed to the fact that PP is quite stable when processed at the lower temperature and time of 190 ^{o}C and 10 min but tended to degrade at higher processing temperatures and times. This suggests that, for PP/VGCF, $t_{1/2}$ was the combined result of the ability of the VGCF to serve as nucleation sites and the degree of polymer degradation.

The activation energy required for crystallization was estimated by the Arrhenius equation (Equation 2.20). Several competing factors contribute to the activation energy of crystallization for polymer nanocomposites. First, nanomaterials can lower ΔE_{ac} by providing nucleation sites (148). However, if the nanomaterials form a percolated

network, the associated reduction in polymer chain mobility increases ΔE_{ac}. Finally, if the polymer has degraded, the thermodynamic driving force for crystallization is reduced which again results in higher values of ΔE_{ac}. In the case of PP, the ΔE_{ac}, like $t_{1/2}$, clearly increased for samples processed at conditions which increased degradation. In the case of PP/SWNT, ΔE_{ac} was lower than for equivalently processed PP as a combined result of the enhanced polymer stability and the presence of nucleation sites. For PP/SWNT processed at 190 ^{o}C and 10 rpm, the higher ΔE_{ac} for samples processed at 240 min compared to that of samples processed for 10 min was surprising given that the SWNTs were better dispersed after the longer processing time. However, as stated earlier, the nanotubes processed at 10 min did not attain a steady state microstructure, while those processed for 240 min did. The more complex microstructure of the composite processed for 240 min resulted in a higher viscosity of the material, reduced polymer chain mobility and, consequently, higher ΔE_{ac}.

The ΔE_{ac} for PP/C12SWNTs was affected by the level of nanotube dispersion and degree of polymer degradation. The highest value of ΔE_{ac} was obtained for PP/C12SWNT processed at 190 ^{o}C, 10 rpm, and 10 min. While the percolated network did exist, the nanotubes were not as well dispersed as they were after 240 min. When processed at a higher temperature of 250 ^{o}C, the degree of nanotube dispersion was similar at both 10 and 240 min of extrusion as seen from Raman mapping ($\sigma(G) \sim 8$). However, the slight polymer degradation resulted in a higher value of ΔE_{ac} for samples extruded for 240 min.

In the case of PP/VGCF, there was surprisingly little change between ΔE_{ac} at 190 ^{o}C; for both 10 min and 240 min, with $\Delta E_{ac} \sim 304$ kJ/mol. At 250 ^{o}C, however, the long

processing time of PP/VGCF increased ΔE_{ac} which was consistent with significant polymer degradation and nanotube aggregation. These results indicated that the processing conditions employed, in conjunction with the nanomaterial being used, play an important role in determining the crystallization kinetics.

6.7 Conclusions

Excellent nanotube distribution obtained during the initial mixing process helped in easily distinguishing the effects of the melt processing conditions. The design of experiments approach used in this study proved to be an effective framework in understanding the individual and combined effects of the material and processing on the nanocomposite. The analysis showed that the optimum melt processing conditions to be employed varied depending on the materials being used and the property of interest. The effects noted were the result of complex interactions between the degree of dispersion, polymer and filler degradation, and stability of the nanocomposite microstructure. The fraction of the polymer in the interphase region, a function of nanomaterial size and dispersion, and the stability of the percolated network were critical to increasing the thermal stability of the polymer in terms of the onset of non-isothermal degradation. A significant observation noted here, also observed by other researchers, was the existence of a critical time of mixing needed to achieve a stable and steady nanocomposite microstructure. The critical time was seen to be more than two hours in some cases of PP/SWNT nanocomposites. While the crystallization temperature was almost solely affected by the type of nanomaterial added, the processing conditions, especially extrusion time, did seem to have an effect on the rate of crystallization of the C12SWNT

and VGCF nanocomposites. Other parameters studied were sensitive to both nanomaterial type and processing conditions; in particular, optimization of decomposition temperature requires simultaneous consideration of nanomaterial type and processing conditions, in addition to a suitable initial mixing method.

Chapter 7

The Effect of Melt Extrusion Process Parameters on Rotary Evaporated Polypropylene Nanocomposites

The results presented in Chapter 4 showed that rotary evaporation (RE) provided better dispersion and properties than dry mixing without the complexity associated with hot coagulation. This chapter is focused on understanding the interrelationships between processing and chemistry of nanomaterials on the properties of PP nanocomposites initially mixed by the rotary evaporation method. The RE method was used to incorporate 0.5 % vol. SWNTs or C12SWNTs, in isopropanol, into PP; this was followed by melt extrusion. A detailed explanation of the materials and procedures employed in this investigation is provided in Section 3.3.4. Design of experiments (DOE) was used to reveal the effects of nanomaterial type, nanomaterial concentration, extrusion temperature, screw speed, and recirculation time on nanocomposite thermal properties and stability. Nanomaterial concentration, a factor that has not been investigated thus far in this research, had a significant influence on the nanocomposite flow behavior during processing, and thus plays an important role in determining optimal processing conditions. A main variation in this chapter, compared to previous chapters, was the type of SWNT employed. This study used CoMoCat SWNTs from SouthWest Nanotechnologies, as opposed to HiPco SWNTs used in the previous studies based on the functionalized SWNTs appearing to be more thermally stable.

7.1 $C_{12}H_{25}$ Functionalization

The presence of dodecyl groups on the sidewalls of C12SWNTs was confirmed by Raman spectroscopy and thermal gravimetric analysis (Figures 7.1 and 7.2). The D:G ratio, in Raman spectroscopy, increased from 0.09 for plain SWNTs to 0.32 for functionalized C12SWNTs. The increased D:G ratio indicated an increase in the fraction of sp^3 hybridized carbons and provided evidence of successful covalent addition of $C_{12}H_{25}$ chains to the nanotube surface. TGA analysis estimated approximately one in every 30 carbon atoms was functionalized with $C_{12}H_{25}$ chain, similar to that obtained in Chapter 6 with HiPco SWNTs.

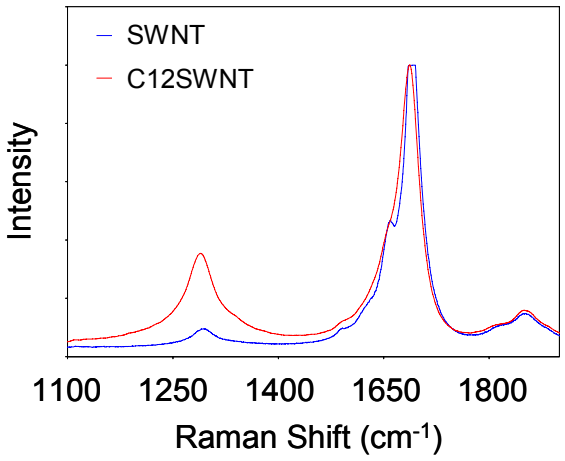

Figure 7.1. Raman spectroscopy of CoMoCat SWNTs and functionalized C12SWNTs.

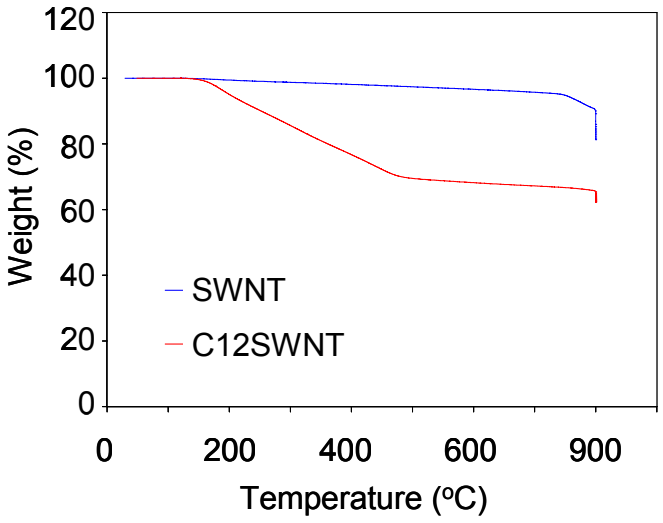

Figure 7.2. TGA of SWNTs and functionalized C12SWNTs under nitrogen.

7.2 Design of Experiments

The design factors considered in this investigation were nanomaterial type, nanomaterial concentration, extrusion temperature, extrusion speed, and extrusion time. A D-optimal design was employed with the upper and lower levels of the process factors as given in Table 7.1. The software generated experimental design run sequence is given in Table 7.2. The experimental runs were randomized to alleviate potential effects from changes in environmental conditions and other unaccounted for factors. Several runs were repeated in order to establish experimental error and differentiate real effects from noise.

Design Factor	Type	Lower Level	Upper Level
Extrusion Temperature (T)	Numerical	190	250
Extrusion Speed (n)	Numerical	10	100
Extrusion Time (t)	Numerical	30	240
Nanomaterial (M)	Categorical	SWNT	C12SWNT
Concentration (x)	Numerical	0.25 % vol.	0.75 % vol.

Table 7.1. Upper and lower levels of design factors.

Numerous responses were measured in order to provide detailed insight into the relationships between nanomaterial type and processing conditions on the final nanocomposite properties. The rheological responses studied were storage modulus (G') at an angular frequency of 0.1 s^{-1}, complex viscosity at an angular frequency of 0.1 s^{-1}, and the slope of G' in the low frequency region. The thermal responses studied were thermal decomposition temperature, melt temperature, crystallization temperature, crystallization activation temperature, and half-time of crystallization.

7.2 Rheology

Rheological characterization provides profound insight into nanotube dispersion and nanocomposite microstructure, in addition to evidence of polymer degradation. As such, rheology is a key tool in understanding the effect of processing parameters on nanocomposite properties.

Run	Temperature (°C)	Speed (rpm)	Time (min)	Concentration (% vol.)	Nanomaterial
1	190	100	30	0.25	C12SWNT
2	190	10	240	0.25	C12SWNT
3	250	10	240	0.75	C12SWNT
4	250	100	135	0.75	SWNT
5	250	100	30	0.25	SWNT
6	220	55	135	0.5	C12SWNT
7	250	55	240	0.75	SWNT
8	220	10	240	0.75	SWNT
9	190	10	240	0.75	C12SWNT
10	250	10	240	0.25	SWNT
11	190	100	240	0.25	SWNT
12	250	10	240	0.25	SWNT
13	190	55	30	0.25	SWNT
14	190	10	30	0.5	SWNT
15	250	100	240	0.75	C12SWNT
16	250	100	30	0.75	C12SWNT
17	190	100	240	0.25	SWNT
18	250	100	240	0.25	C12SWNT
19	190	10	30	0.75	C12SWNT
20	250	10	30	0.75	SWNT
21	250	10	30	0.25	C12SWNT
22	250	100	30	0.75	C12SWNT
23	190	10	135	0.75	SWNT
24	220	55	135	0.5	C12SWNT
25	190	10	30	0.25	C12SWNT
26	190	10	135	0.25	SWNT
27	220	10	30	0.25	SWNT
28	190	100	240	0.75	C12SWNT
29	190	100	30	0.75	SWNT
30	190	10	30	0.5	SWNT

Table 7.2. Design generated experimental runs sequence.

7.2.1 Storage Modulus

Analysis of variance (ANOVA) of G' data for 29 of the 30 runs in the DOE isolated the factors that had a statistically significant effect on G' (Table 7.3). Run number 18 (PP/C12SWNT 0.25 % vol. processed at 250 ^{o}C, 100 rpm, 240 min) was not included in analyzing the design of rheological responses as the material did not result in useable data owing to severe degradation. The ratio of the maximum G' response obtained to the minimum G' response obtained, amongst all the runs, was greater than 10, thus indicating a transformation was required in analyzing the design. A $\log_{10}$ (G') transformation of G' was applied in order to result in a better predictive model for the storage modulus. Factors and interactions with $p < 0.05$ were deemed significant and included in the predictive models for G' given in Table 7.4. The Model F-value of 30.54 ($p < 0.0001$) indicated that the model is significant and that there was only a 0.01% chance the variation associated with the changing of the control factor could occur due to experimental noise. An $R^2 = 0.786$ indicated that the model explains 78.6 % of the total variation observed in G'. The coefficient of variability (C.V.), a measure of the relative amount of unexplained variation present, was 24.3 %.

Source	**Sum of Squares**	**DF**	**Mean Square**	**F Value**	**Prob > F**
Model	7.99	3	2.66	30.54	<0.0001
Extrusion Temp (*T*)	2.26	1	2.26	25.88	<0.0001
Extrusion Speed (*n*)	1.22	1	1.22	13.98	0.0010
Concentration (*x*)	5.23	1	5.23	60.00	<0.0001
Residual	2.18	25	0.087		
Cor. Total	10.17	28			
Standard Deviation 0.3	**Mean** 1.21		**R^2** 0.786	**Coefficient of Variance**	24.3

Table 7.3. ANOVA of storage modulus G'.

	Storage Modulus at 0.1 s^{-1}
SWNT	$Log_{10}(G') = 2.257 - 0.0103*T + 5.053E\text{-}03*n + 1.883*x$
C12SWNT	$Log_{10}(G') = 2.257 - 0.0103*T + 5.053E\text{-}03*n + 1.883*x$

Table 7.4. DOE generated model for storage modulus G'.

A comparison between the experimental data and the model predicted data showed good agreement between the data sets (Figure 7.3). The percentage contribution of the process factors on the final G' value was calculated as the ratio of the individual sum of squares of the process factors to the total sum of squares. G', at an angular frequency of 0.1 s^{-1}, was mostly affected by nanomaterial concentration, extrusion temperature, and extrusion speed. It is to be noted that the model for G' does not predict the modulus behavior over the entire angular frequency range, but only at an angular frequency of 0.1 s^{-1}. Nanomaterial concentration had the most significant effect with a contribution of over 50 % towards the final G' value, while extrusion temperature and speed had 22 % and 12 % contribution respectively. It was a surprising revelation that the type of nanomaterial incorporated did not have a significant effect on G' (thus explaining the identical model for both PP/SWNT and PP/C12SWNT). This indicated that functionalizing the nanotubes with $C_{12}H_{25}$ groups did not enhance nanotube dispersion during melt processing. It is possible that some or all of the functional groups were removed from nanotube surface during the high temperature processing conditions in the extruder. Functionalizing nanotubes does have its benefits; such as a much lower sonication time for C12SWNTs to attain nearly the same aspect ratio as SWNTs in

isopropanol. The model generated for G' indicated that higher extrusion temperature resulted in lower G' values, most likely owing to polymer degradation at high temperatures. However, higher extrusion speed and nanotube concentration resulted in higher storage modulus.

The effect of nanomaterial concentration, extrusion temperature, extrusion speed can be better visualized by examining their interaction plots (Figure 7.4). At low nanomaterial concentrations, the processing conditions did not have any effect on G' of the nanocomposite. G' of nanocomposites largely depended on the ability of the nanomaterials to prevent the polymer chains from relaxing. This was attained by nanotube network formation achieved by a combination of nanotube concentration and dispersion.

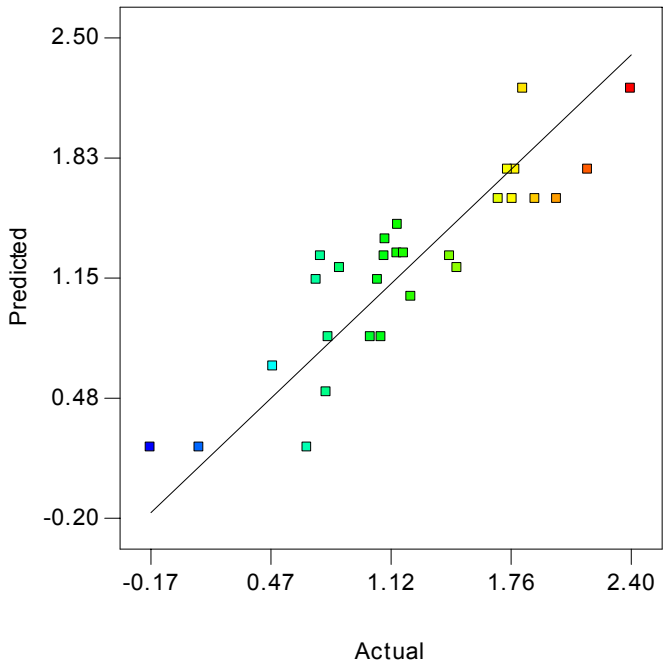

Figure 7.3. Actual versus model predicted $\log_{10}$(G'). (The different colors are an indication of variation in magnitude).

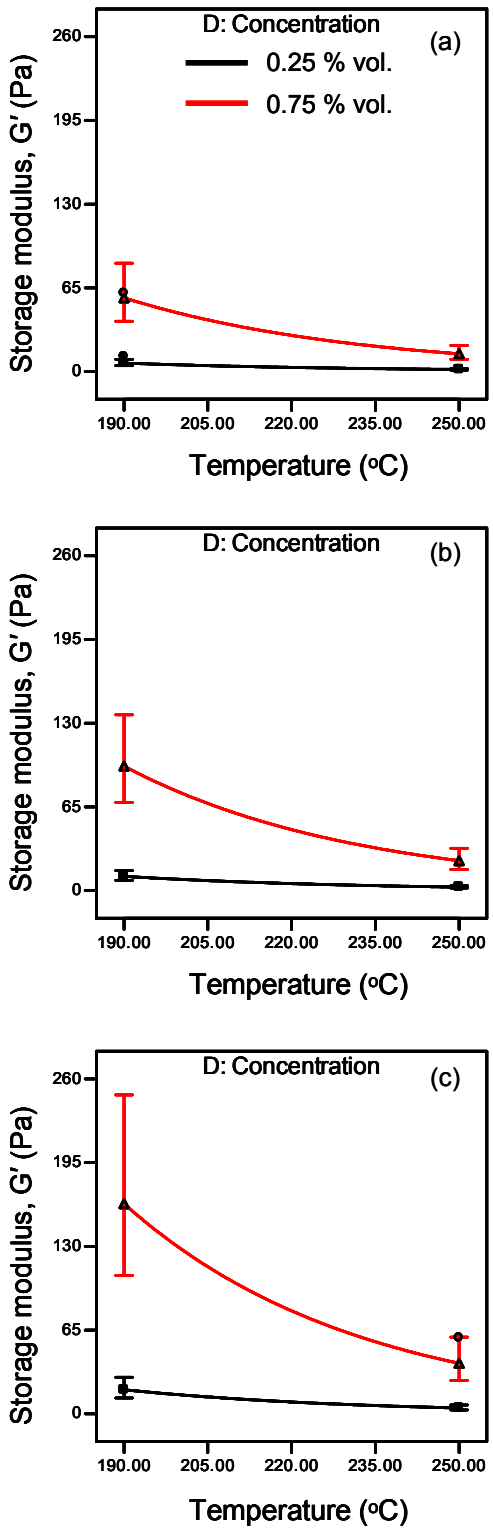

Figure 7.4. Effect of interaction of extrusion temperature, speed, and concentration on PP nanocomposites' storage modulus (a) 10 rpm, (b) 55 rpm, and (c) 100 rpm.

At 0.25 vol. %, the amount of nanotubes present in the polymer matrix was insufficient to provide a strong enough nanotube network to affect PP terminal region behavior. A slight increase in the G' of PP nanocomposites (0.25 % vol.) was observed with an increase in extrusion speed to 100 rpm at 190 ^{o}C. While higher extrusion speed translates into higher applied shear on the nanotube aggregates and thus breaks them apart into smaller bundles and increases G', a nanotube concentration of 0.25 % vol. was still below the percolation threshold, regardless of aggregation state, and therefore there no drastic changes in G' was observed. Percolation is expected between a concentration of 0.35 % and 0.5 % vol. for an aspect ratio of 200 to 300 (assuming nanotube bundle diameter of 4 nm) (128). Figure 7.5 shows experimental data comparing the effect of processing conditions on G' value of PP/C12SWNT nanocomposites. The plot shows, for a concentration of 0.25 % vol., there was no significant difference in G' at $\omega = 0.1\ s^{-1}$ due to the increase in extrusion speed (the red and green lines in the plot). However, an increase in concentration to 0.75 % vol. resulted in approximately and order of magnitude increase in G'. This reaffirms the fact that a concentration of 0.25 % vol. was well below percolation, and therefore changing the processing conditions had little effect on G'.

At a vol. % of 0.75, the amount of nanotubes present in the polymer matrix was well above the theoretical percolation threshold for the nanotube bundles. At such high concentrations, processing conditions can have a significant effect on the nanotube network formation and percolation of PP nanocomposites. As seen from Figure 7.4, the G' of the nanocomposites, especially at 190 ^{o}C, more than doubled in value with an increase in processing speed from 10 rpm to 100 rpm. Again, higher shear at the higher speeds broke apart the nanotube bundles and dispersed them through the bulk polymer.

The presence of a significantly larger amount of nanotubes in the 0.75 % vol. nanocomposites compared to the 0.25 % vol. nanocomposites results in much higher influence of extrusion speed and temperature on the properties of nanocomposites with higher concentration. of nanotubes.

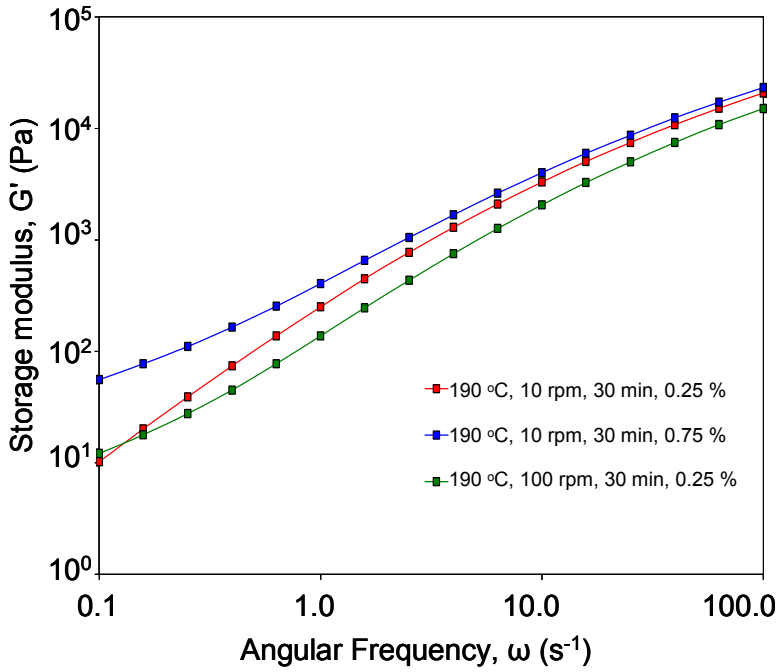

Figure 7.5. Effect of processing conditions on PP/C12SWNT

Figure 7.6 compares the effect of extrusion temperature and speed on G' at $\omega = 0.1\ s^{-1}$ of PP/C12SWNT (0.75 % vol.) nanocomposites processed for 30 min. The plot shows a significant increase in G' at $\omega = 0.1\ s^{-1}$ when processed at the higher temperature and speed, reaffirming the influence of these processing conditions in breaking apart the nanotube aggregates in to smaller bundles. The increase in G' seen in the figure was solely due to higher shear from the increased speed; high extrusion temperature did not contribute to the increase in G', and was in fact detrimental due to the degradation in PP it

brought forth. In oscillatory rheological tests, low frequencies probe the nanocomposite behavior under long testing time (conditions where the polymer chains are relaxed and the response is largely due to the nanomaterials present in the polymer), while high frequencies probe the nanocomposite behavior under short testing time (conditions wherein the response is due to the polymer). Variation in G' at higher frequencies indicate variations in PP molecular weight. The degradation in PP, due to processing at higher temperatures, is evident from the figure by the lower G' values at higher frequencies compared to the nanocomposite processed at 190 ^{o}C.

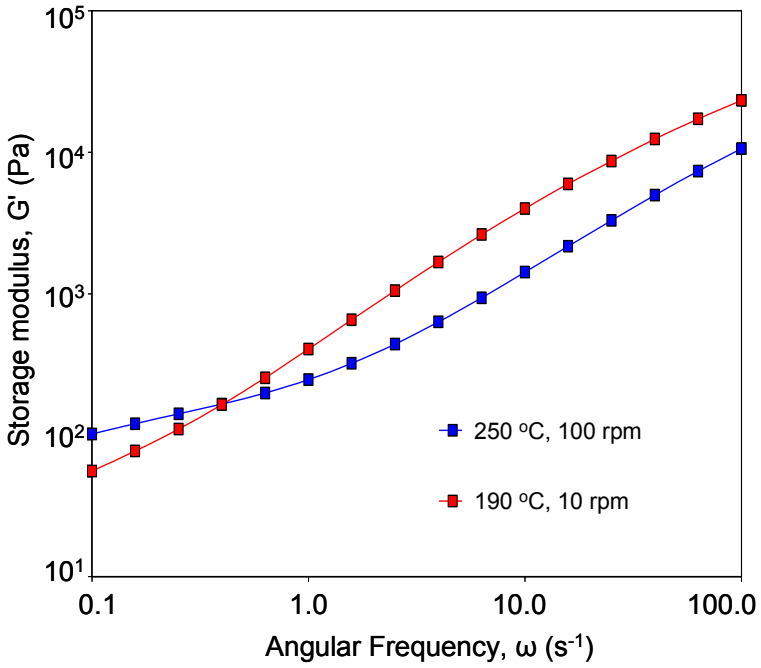

Figure 7.6. Storage modulus of PP/C12SWNT 0.75 % vol. extruded for 30 min.

Percolation in polymer nanocomposites is also manifested as an apparent yield stress in G' in the terminal region on an oscillatory rheological test (at $\omega < 1$ s^{-1}) (130). Plain PP exhibited typical terminal region behavior with a G' slope ~ 2. With the

addition of nanotubes, the G' values tended to get higher and the curves tended to get flatter (thus decreasing the slope). At percolation, the slope is ~ 0 and G' is independent of frequency. Thus, a lower value for the slope is desired as it indicates nanotube network formation. It should also be noted that the magnitude of G' and the slope of the G' curve does not necessarily trend together. While high shear will help disperse nanotubes in PP and significantly increase G' magnitude and decrease the G' slope (indicating nanotube network formation), the combined effect of high shear with other processing conditions may have contrasting results. For example, a very high shear applied for a long time may result in excellent nanotube dispersion, thus decreasing G' slope, but, depending on the extrusion temperature, the long processing period may also significantly degrade the polymer, resulting in a decrease in G' magnitude. In this study, extrusion speed and time, and nanotube concentration had very significant effects on the slope of the G' curve and therefore the degree of nanotube network formation in PP. The extrusion speed and time each had a ~ 28 % contribution towards determining the G' slope, while the nanotube concentration had a 12 % contribution. Other significant factors included the interactions between temperature and speed, and that between speed and nanomaterial type. Table 7.5 shows the ANOVA while Table 7.6 shows the predictive model for G' slope as generated by the design software. A $(\text{G' slope} + 0.5)^{1/2}$ transformation was employed in analyzing the data. Interaction plots in Figure 7.7 clearly show that higher concentration always result in lower slope, indicating a better nanotube network and more complex nanocomposite microstructure. In addition, it was observed that processing at higher speeds and longer durations led to lower G' slopes, indicating that the continuous application of shear for long processing periods tended to

break apart the nanotube aggregates, and also provided sufficient time to disperse the debundled nanotubes through the PP matrix and encouraged nanotube network formation.

Source	Sum of Squares	DF	Mean Square	F Value	Prob > F
Model	1.10	7	0.16	26.03	<0.0001
Extrusion Temp (*T*)	1.73E-03	1	1.73E-03	0.29	0.5981
Extrusion Speed (*n*)	0.34	1	0.34	56.30	<0.0001
Time (*t*)	0.34	1	0.34	56.53	<0.0001
Concentration (*x*)	0.14	1	0.14	22.50	0.0001
Material (*M*)	5.29E-03	1	5.29E-03	0.87	0.3609
Tn	0.08	1	0.08	12.31	0.0021
nM	0.04	1	0.04	6.72	0.0170
Residual	0.13	21	6.06E-03		
Cor. Total	1.23	28			

Standard Deviation	0.08	**Mean**	1.09	**R^2**	0.897	**Coefficient of Variance**	7.16

Table 7.5. ANOVA of G' slope.

Slope of Storage Modulus Curve	
SWNT	Sqrt(G' slope + 0.5) = 0.978 + 2.842E-03**T* + 6.522E-03**n* – 1.199E-03**t* – 0.324**x* – 4.635-05**T***n*
C12SWNT	Sqrt(G' slope + 0.5) = 0.846 + 2.842E-03**T* + 8.413E-03**n* – 1.199E-03**t* – 0.324**x* – 4.635-05**T***n*

Table 7.6. DOE generated model for slope of storage modulus curve in terminal region.

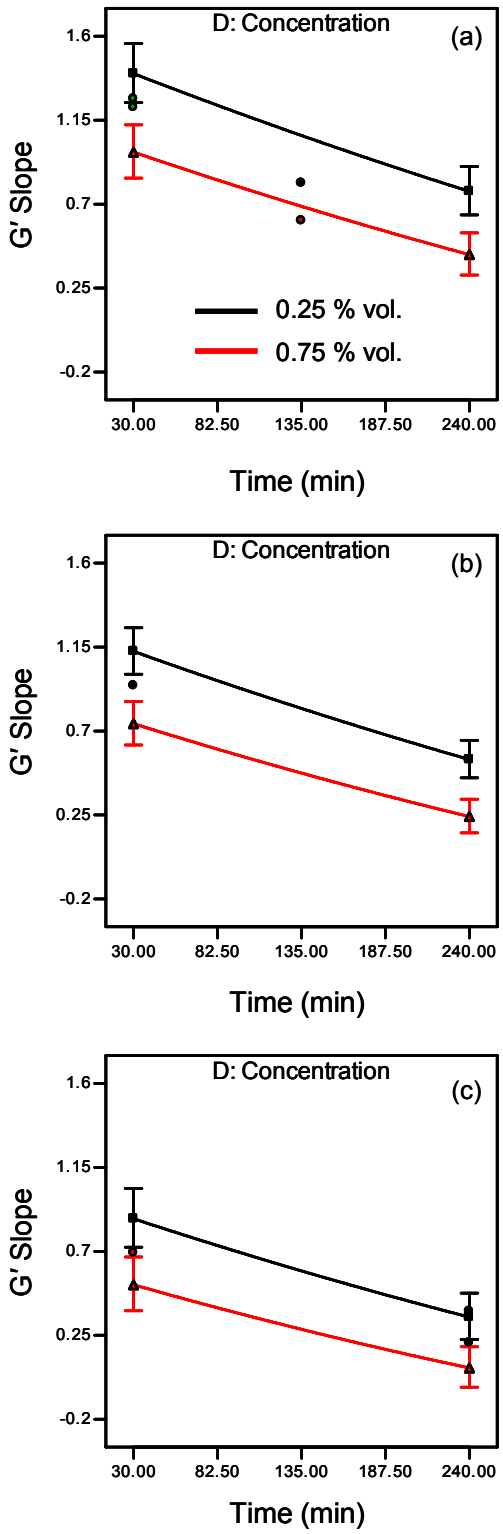

Figure 7.7. Effect of interaction of extrusion time, speed, and concentration on the slope of PP/C12SWNT storage modulus (a) 10 rpm, (b) 55 rpm, and (c) 100 rpm. PP/SWNT nanocomposites display similar interaction effects.

Figure 7.8 shows G' behavior of PP/C12SWNT processed at 190 ^{o}C, 10 rpm, with extrusion time of 30 or 240 min and concentration of 0.25 or 0.75 % vol. For a concentration of 0.25 % vol., the magnitudes of G' at $\omega = 0.1\ s^{-1}$ extruded at 30 min and 240 min were similar. However, at higher frequencies the PP/C12SWNT extruded for 240 min had a much lower G' value, indicating a decrease in PP molecular weight. During extrusion, shear acted to break up the nanotube aggregates. Longer processing time allowed more nanotube aggregates to break or peel off in to smaller bundles and more uniformly disperse in PP. The fact that both these nanocomposites had the same G' magnitude at $\omega = 0.1\ s^{-1}$, even though the longer extrusion time resulted in better nanotube dispersion, is due to considerably more PP degradation in PP/C12SWNT 0.25 % extruded for 240 min resulting from the longer processing time. At the higher concentration of 0.75 % vol., the higher magnitude and lower slope at low frequency after processing at 240 min. suggests network formation. At higher frequencies the difference between the magnitudes of 0.75 % vol. material processed at 30 min and 240 min is less pronounced than for the lower concentration material. This is due to the fact that while polymer degradation did still occur over long processing times, the network formation stabililzed the interphase and reduced the amount of degradation.

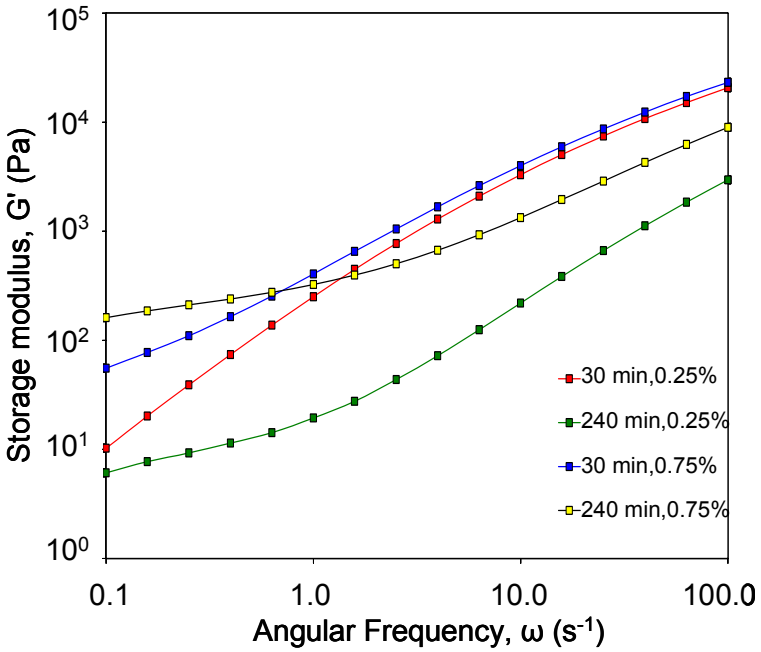

Figure 7.8. Storage modulus of PP/C12SWNTs processed at 190 °C and 10 rpm.

From the discussion above for the magnitude of G' at $\omega = 0.1\ s^{-1}$ and the slope of the G' curve, it can be summarized that achieving best values for both will require a lower extrusion temperature, and a higher extrusion speed and time, at a high nanotube concentration. Figure 7.9 shows a plot of G' from experimental data on PP/C12SWNT 0.75 % vol. A low extrusion temperature of 190 °C, and high extrusion speed and time of 100 rpm and 240 min clearly resulted in the smallest slope and the largest G' magnitude. An increase in extrusion temperature to 250 °C brought about a drastic decrease in G' value when combined with a long extrusion period of 240 min, again owing to severe PP degradation. However, from the figure, there was not much evidence for PP degradation when processed at 250 °C for just 30 min. This is attributed to the fact that the concentration of nanotubes in PP at 0.75 % vol. is sufficiently high to

stabilize the polymer chains from degradation during shorter processing periods at high temperatures.

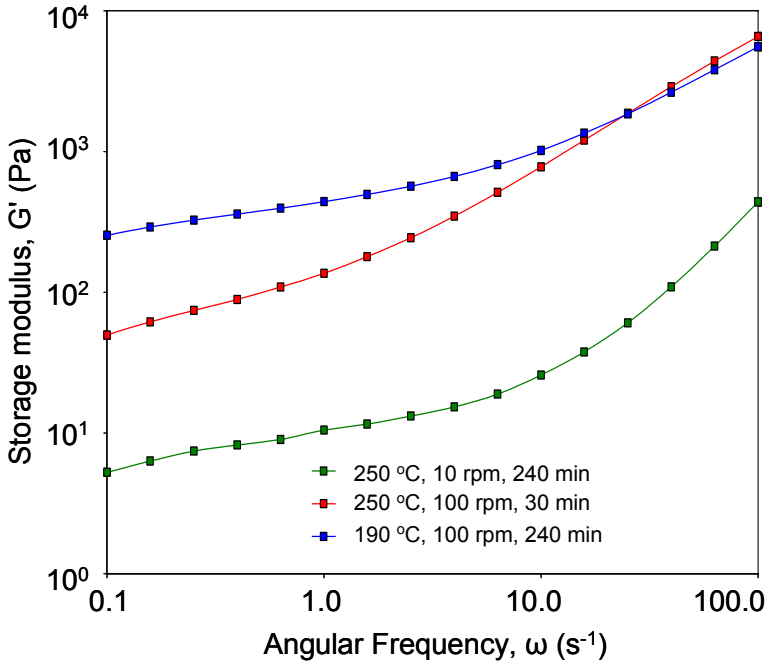

Figure 7.9. Storage modulus of PP/C12SWNT (0.75 % vol.).

6.2.2 Complex Viscosity, η^*

ANOVA was also performed on complex viscosity, η^* at $\omega = 0.1$ s^{-1}. Extrusion temperature, extrusion time, nanotube concentration, and the interaction between speed and concentration were found to be the dominant factors affecting complex viscosity. Temperature and concentration had the most significant effects with contributions over 25 % each towards determining η^*. Again, as with G' magnitude at $\omega = 0.1$ s^{-1}, nanotube type did not affect η^*. Thus the predictive model was identical for both PP/SWNT and PP/C12SWNT. The ANOVA for η^* is presented in Table 7.7 and the design generated model is presented in Table 7.8.

Source	Sum of Squares	DF	Mean Square	F Value	Prob > F
Model	2614.89	5	522.98	9.00	<0.0001
Extrusion Temp (*T*)	1012.86	1	1012.86	17.43	0.0004
Extrusion Speed (*n*)	49.64	1	49.64	0.85	0.3649
Time (*t*)	797.56	1	797.56	13.73	0.0012
Concentration (*x*)	1043.28	1	1043.28	17.96	0.0003
nx	326.92	1	326.92	5.63	0.0264
Residual	1336.38	23	58.10		
Cor. Total	3951.27	28			

Standard Deviation	7.62	**Mean**	27.86	**R^2**	0.662	**Coefficient of Variance**	27.4

Table 7.7. Analysis of Variance for complex viscosity.

Complex Viscosity at 0.1 s^{-1}	
SWNT	$\text{Sqrt}(\eta^* + 0.5) = 81.246 - 0.227*T - 0.209*n - 0.056*t + 7.645*x + 0.354*n*x$
C12SWNT	$\text{Sqrt}(\eta^* + 0.5) = 81.246 - 0.227*T - 0.209*n - 0.056*t + 7.645*x + 0.354*n*x$

Table 7.8. Design generated predictive model for complex viscosity.

The predictive models showed that higher temperature and time tended to decrease complex viscosity. This was related to the fact that processing at higher temperatures and long times led to significant PP degradation. On the other hand, increasing nanotube concentration and the interaction between concentration and speed resulted in an increase in η^*. This was again attributed to the fact that higher concentration could more easily

form complex nanotube networks that prevented PP chain relaxation and flow. Figure 7.10 shows the large increase in η^* magnitude with increase in nanotube concentration.

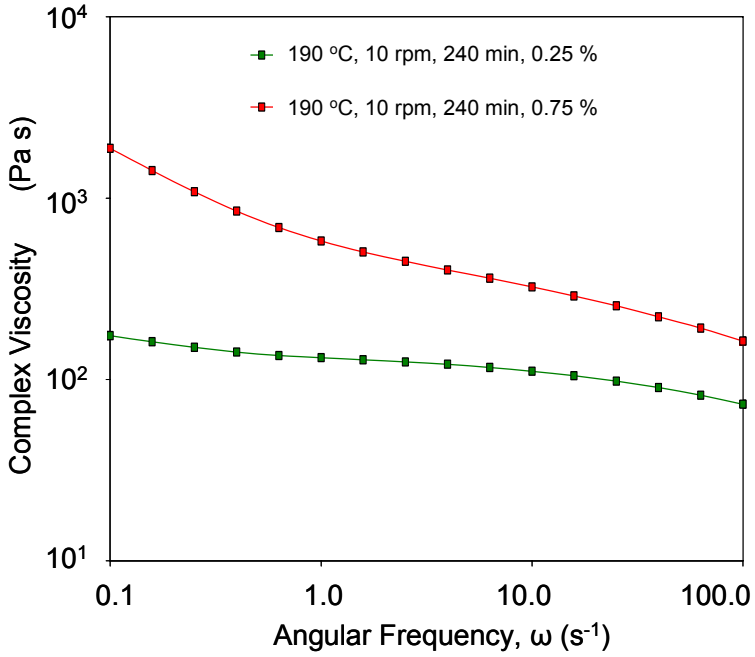

Figure 7.10. Complex viscosity of PP/C12SWNT. Error bars on the curves are negligible.

The interactions between all the factors can be visualized in Figure 7.11 (since the nanotube type was not a significant factor, the interaction plot in the figure is valid for both PP/SWNT and PP/C12SWNT). As expected, for a given processing condition, higher SWNT concentration resulted in higher η^*. Higher temperatures and longer extrusion periods drastically decreased η^* for a given concentration and screw speed.

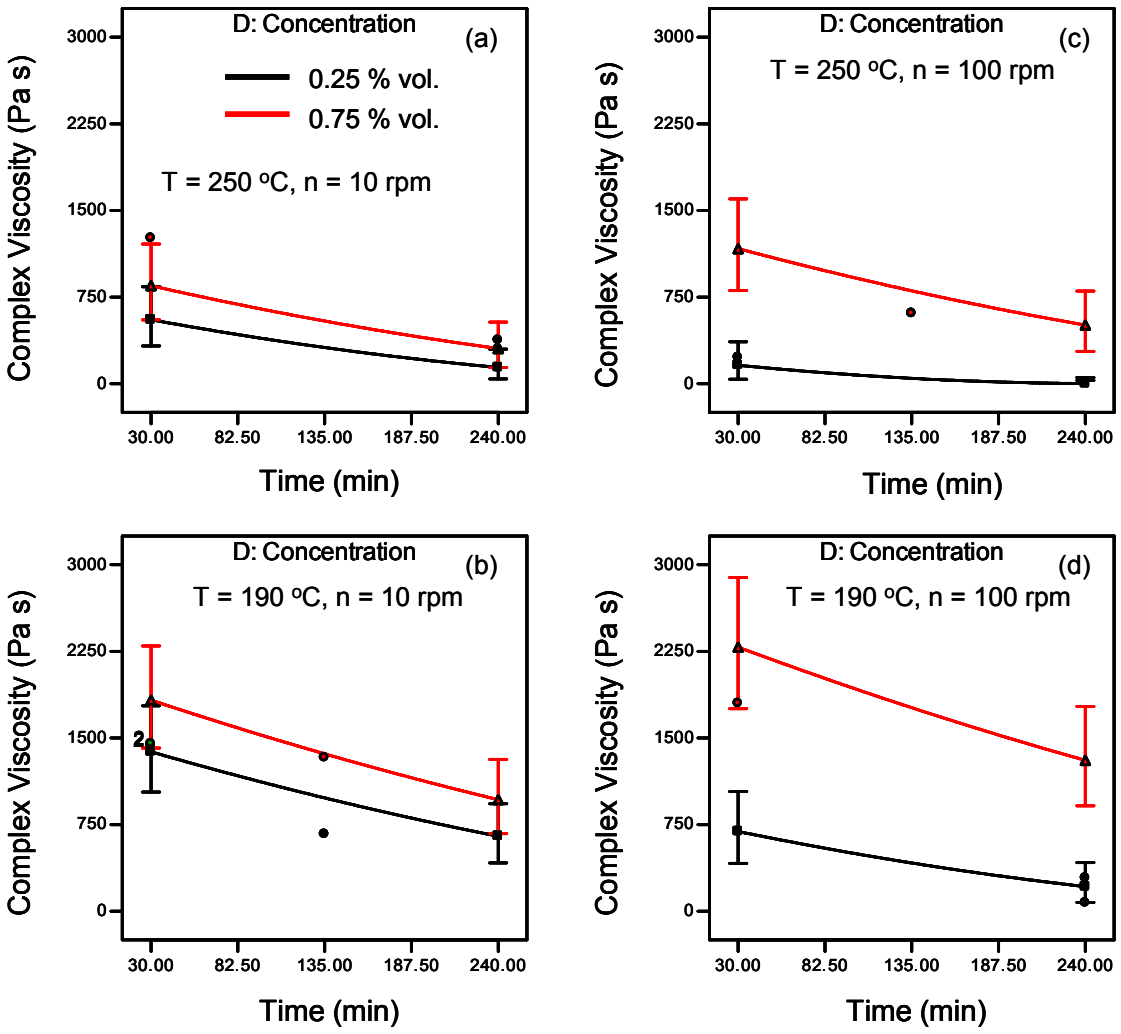

Figure 7.11. Interaction plot of complex viscosity η*.

However, while higher screw speed is also expected to increase shear degradation of PP, extrusion speeds of 100 rpm resulted in a significant increase in η^* of 0.75 % vol. PP nanocomposites, especially at low extrusion time, when processed at either 190 or 250 ^{o}C (Figure 7.12). This was due to higher shear facilitating the break up of aggregates and the resulting network stabilizing against PP degradation. However, the effect of speed at lower nanotube concentrations was the exact opposite and η^* was seen to decrease with

increase extrusion speed. This is attributed to the lack of nanotubes to form a network or stabilize against PP degradation.

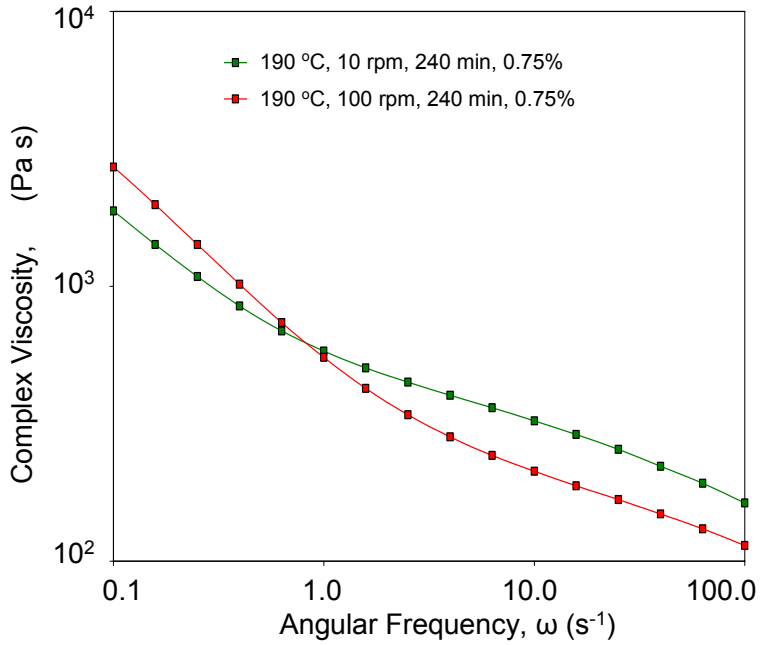

Figure 7.12. Complex viscosity of PP/C12SWNT nanocomposites.

7.3 Thermal Decomposition Temperature (T_d)

Analysis of variance (ANOVA) of the T_d data for all 30 runs in the DOE isolated the nanomaterial, concentration, and processing factors that had a statistically significant effect on the thermal decomposition temperature (Table 7.9). Factors and interactions with $p < 0.05$ were deemed significant and were included in the predictive models for T_d given in Table 7.10. The Model F-value of 22.44 ($p < 0.0001$) indicated that the model was significant and that there was only a 0.01% chance the variation associated with the changing of the control factor could occur due to experimental noise. An $R^2 = 0.824$ indicated that the model explained 82.4 % of the total variation observed in T_d. The

coefficient of variability (C.V.) was 1.94; confirming that the T_d model had a high predictive value for this data set. A comparison between the experimental data and the model predicted data showed good agreement between the data sets (Figure 7.13).

Source	**Sum of Squares**	**DF**	**Mean Square**	**F Value**	**Prob > F**
Model	7273.84	5	1454.77	22.44	<0.0001
Extrusion Temp (*T*)	2249.80	1	2249.80	34.70	<0.0001
Extrusion Time (*t*)	3557.66	1	3557.66	54.87	<0.0001
Concentration (*x*)	817.71	1	817.71	12.61	0.0016
Material (*M*)	347.80	1	347.80	5.35	0.0296
TM	375.24	1	375.24	5.79	0.0242
Residual	1556.03	24	64.83		
Cor. Total	8829.87	29			

Standard Deviation	8.05	**Mean**	415.93	**R^2**	0.824	**Coefficient of Variance**	1.94

Table 7.9. Analysis of variance for decomposition temperature.

	Decomposition Temperature
SWNT	$T_d = 464.070 - 0.189*T - 0.115*t + 22.923*x$
C12SWNT	$T_d = 513.614 - 0.446*T - 0.115*t + 22.923*x$

Table 7.10. Design generated predictive model for decomposition temperature.

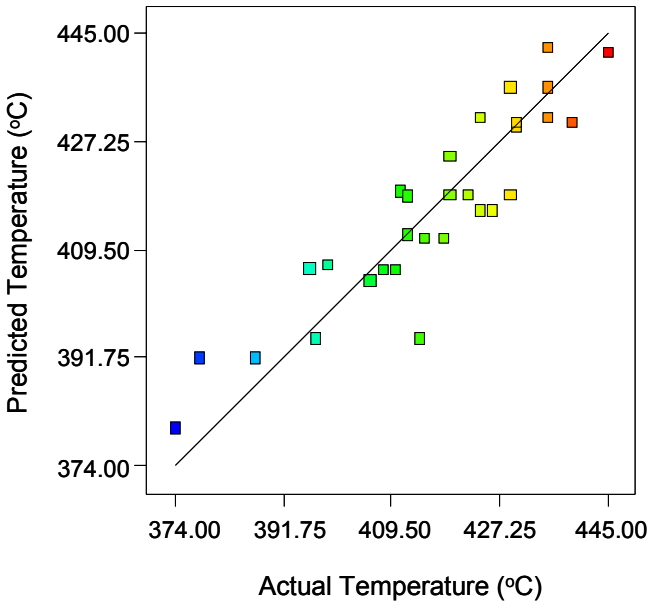

Figure 7.13. Comparison of model predicted decomposition temperature to experimental values.

Extrusion temperature and extrusion time had the most significant contribution in determining T_d at 25 % and 40 % respectively. Other factors such as nanomaterial type, nanomaterial concentration, and the interaction between extrusion temperature and nanomaterial type had significant effects too. Both extrusion temperature and time tended to decrease T_d due to these parameters resulting in polymer degradation, which in turn resulted in more free radicals to catalyze decomposition at lower temperatures. On the other hand, increasing concentration tended to increase T_d. This was attributed to the fact that a higher concentration of nanotubes led to higher volume of PP chains in the stabilized interphase region. Besides, higher nanotube concentrations tended to form an interconnected network more effortlessly (even when dispersed as small bundles) than at lower concentrations (wherein the nanotubes have to be individually dispersed to form a network), thus preventing the decomposition products from escaping, and led to higher

T_d. These effects of the process factors are clearly visualized in the interaction plot in Figure 7.14. The effect of the process factors on PP/C12SWNT was similar to that on PP/SWNT. The figure illustrates the decrease in T_d with increasing temperature or processing time, and also shows the higher T_d for nanocomposites with higher concentration of nanotubes.

A major deviation in the effect of processing conditions on the RE nanocomposites compared to the HC nanocomposites in Chapter 6 was the effect of extrusion temperature. Extrusion temperature was not a significant factor by itself in HC nanocomposites (however, the interaction of extrusion temperature and nanomaterial had a significant effect). This was likely due to the fact that the HC nanocomposites contained more nanotubes (1 % vol.), and the nanotubes were significantly better dispersed prior melt extrusion compared to RE nanocomposites. These two aspects of the HC nanocomposites led to better stability against PP degradation, and consequently extrusion temperature alone did not influence T_d. In the case of RE nanocomposites, the nanotube concentration was lower than that in the HC nanocomposites and the nanotubes were not as well dispersed in the feed that enters the extruder; thus achieving a lower degree of stability against PP degradation. Consequently, extrusion temperature had a significant effect on PP degradation and the resulting T_d.

7.4 Melting Temperature

Analyses of melting temperature (T_m) data was performed in the same manner as for thermal decomposition and rheological responses (Table 7.11). The model for melt

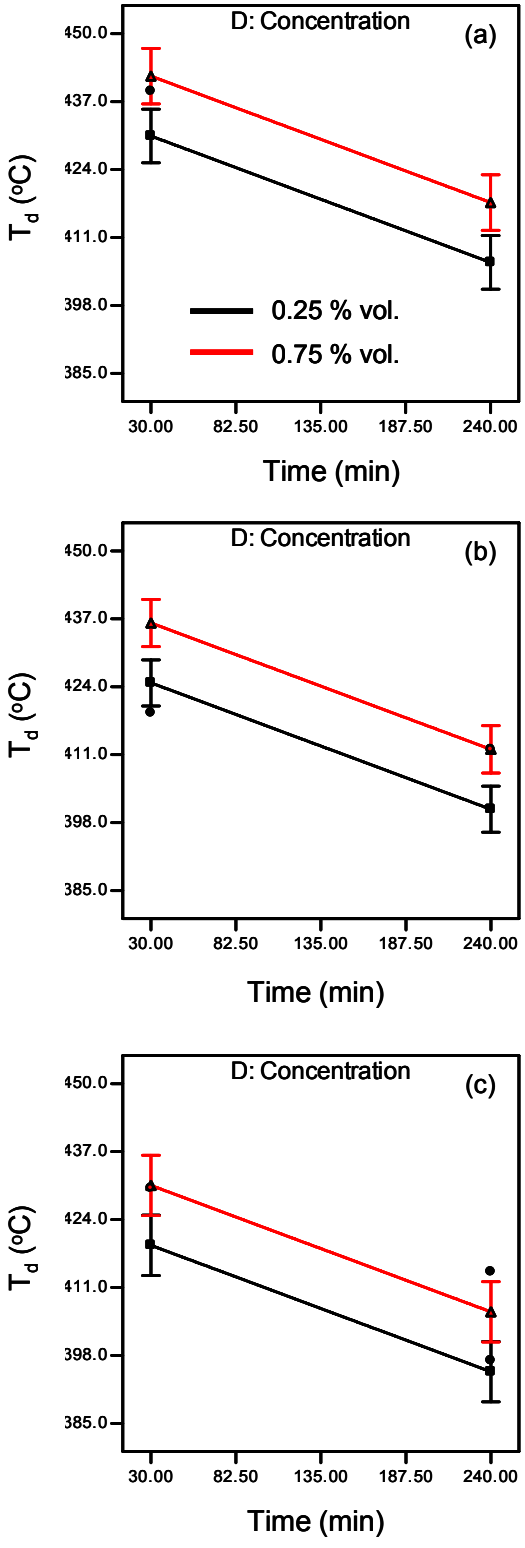

Figure 7.14. Interaction plot of decomposition temperature of PP/SWNT (a) 190 ^{o}C, (b) 220 ^{o}C, and (c) 250 ^{o}C.

temperature is given in Table 7.12. The model had an F-value = 26.31 ($p < 0.0001$), and $R^2 = 0.949$. Extrusion temperature and extrusion time had the most significant effects on T_m and accounted for approximately 20 % and 40% of the contribution respectively. T_m was also affected by numerous other factors and interactions (Table 7.11). It was interesting to note that T_m was affected by large number of factors. It can be recalled that, for nanocomposites fabricated from HC samples, T_m was largely affected by the type of nanomaterial incorporated. In this investigation, the type of nanomaterial incorporated, SWNTs or C12SWNTs, while statistically significant, were not major contributors in deciding the melt temperature of the resulting nanocomposites. This was attributed to the fact that the sonication times employed for SWNTs and C12SWNTs were different and resulted in comparable initial dispersion in isopropanol and approximately the same aspect ratio. Thus, while functionalizing the nanotubes helped reduce the sonication time in the initial mixing, it did not have any effect on the T_m of the nanocomposites compared to pristine SWNTs. They were both equivalently dispersed in PP, depending on the processing conditions employed, and had the same effect on PP chain mobility and the resulting T_m. Figure 7.15 compares the predicted values to experimental values, and confirms the high predictability of the model.

7.5 Crystallization Temperature

The ANOVA for crystallization temperature, T_c is given in Table 7.13, and the model is given in Table 7.14. The model was highly significant with an F-value = 24.48 ($p < 0.0001$), and $R^2 = 0.928$. Since crystallization temperature is an intrinsic property, it was not surprising that the design showed that the type of nanomaterial incorporated and

Source	Sum of Squares	DF	Mean Square	F Value	Prob > F
Model	345.81	12	28.82	26.39	<0.0001
Extrusion Temp (*T*)	76.66	1	76.66	70.20	<0.0001
Extrusion Speed (*n*)	21.96	1	21.96	20.11	0.0003
Extrusion Time (*t*)	140.45	1	140.45	128.61	<0.0001
Concentration (*x*)	9.71	1	9.71	8.89	0.0084
Material (*M*)	7.43	1	7.43	6.80	0.0184
Tn	7.71	1	7.71	7.06	0.0166
Tt	25.84	1	25.84	23.66	0.0001
Tx	15.64	1	15.64	14.32	0.0015
nt	13.98	1	13.98	12.80	0.0023
nx	14.19	1	14.19	12.99	0.0022
nM	9.58	1	9.58	8.78	0.0087
tM	7.36	1	7.36	6.74	0.0188
Residual	18.56	17	1.09		
Cor. Total	364.38	29			
Standard Deviation 1.05	**Mean** 161.41	**R^2** 0.949	**Coefficient of Variance** 0.65		

Table 7.11. Analysis of variance of melt temperature.

	Melt Temperature
SWNT	$T_m = 149.103 + 0.076*T + 0.048*n + 0.066*t + 21.757*x - 4.486E\text{-}04*T*n - 3.483E\text{-}04*T*t - 0.105*T*x - 1.560E\text{-}04*n*t + 0.071*n*x$
C12SWNT	$T_m = 154.264 + 0.046*T + 0.080*n + 0.056*t + 21.757*x - 4.486E\text{-}04*T*n - 3.483E\text{-}04*T*t - 0.105*T*x - 1.560E\text{-}04*n*t + 0.071*n*x$

Table 7.12. Design generated predictive model for melt temperature.

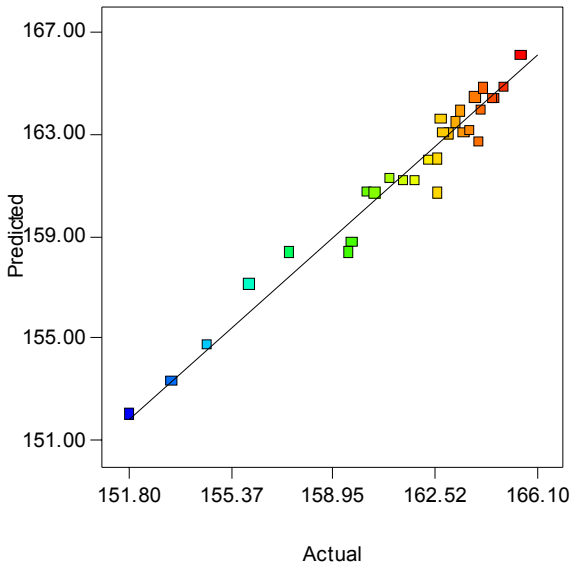

Figure 7.15. Comparison of predicted and experimental melt temperature

nanomaterial concentration contributed for over 20 % and 35 % respectively of the effect on the resulting T_c. Surprisingly, time did not have a significant effect on the crystallization temperature. However, the interaction of time and temperature had a significant effect and resulted in a decrease in T_c. Extrusion temperature and speed had significant effects with contributions over 15 % each. In addition, quite a few process factors interactions had significant effects on T_c, and are listed in Table 7.13. The T_c of PP/SWNTs slightly increased with temperature while that of PP/C12SWNTs decreased quite rapidly. The decrease in T_c of PP/C12SWNTs was largely attributed to the fact that the functional groups tended to decompose quite rapidly at higher processing temperatures, thus decreasing their effectiveness. T_c increased with concentration, more so with C12SWNTs than SWNTs. Higher concentration of nanotubes resulted in more polymer chain nucleation sites, and thus a higher crystallization temperature. The

Source	Sum of Squares	DF	Mean Square	F Value	Prob > F
Model	150.01	10	15.00	24.48	<0.0001
Extrusion Temp (*T*)	24.12	1	24.12	39.39	<0.0001
Extrusion Speed (*n*)	26.10	1	26.10	42.60	<0.0001
Extrusion Time (*t*)	0.48	1	0.48	0.78	0.3891
Concentration (*x*)	54.95	1	54.95	89.70	<0.0001
Material (*M*)	34.55	1	34.55	56.39	<0.0001
Tt	6.54	1	6.54	10.68	0.0040
TM	3.45	1	3.45	5.63	0.0283
xM	6.77	1	6.77	11.05	0.0036
n^2	3.07	1	3.07	5.00	0.0375
t^2	5.18	1	5.18	8.45	0.0090
Residual	11.64	19	0.61		
Cor. Total	161.65	29			

Standard Deviation	0.78	**Mean**	126.63	$\mathbf{R^2}$	0.928	**Coefficient of Variance**	0.62

Table 7.13. Analysis of variance of crystallization temperature.

	Crystallization Temperature
SWNT	$T_c = 122.111 + 4.127E\text{-}03*T + 0.081*n + 0.069*t + 3.836*x - 1.825E\text{-}04*T*t - 5.153E\text{-}04*n^2 - 1.130E\text{-}04*t^2$
C12SWNT	$T_c = 123.359 - 0.022*T + 0.081*n + 0.069*t + 8.189*x - 1.825E\text{-}04*T*t - 5.153E\text{-}04*n^2 - 1.130E\text{-}04*t^2$

Table 7.14. Design generated predictive model for crystallization temperature

interaction of extrusion temperature and time had a negative effect on T_c. This is expected since extrusion at high temperatures for long durations tended to degrade PP, and the resulting shorter PP chains tended to be more mobile and crystallize at lower temperatures.

The previously discussed effects can be seen in the interaction plots in Figure 7.16. While T_c of PP/SWNTs was not drastically affected by temperature, the T_c of PP/C12SWNTs was highly temperature dependent and tended to decrease rapidly with increasing temperature. Higher screw speeds tended to increase T_c. This was again attributed to the fact that higher screw speeds translated into higher shear forces applied on the nanotube aggregates. The break up of these aggregates provided a drastic increase in the available nucleation sites for PP chains, thus increasing the crystallization temperature.

The effect of processing conditions observed on T_c was also observed on the crystallization half-time, $t_{1/2}$, and crystallization activation energy $\Delta E_{a,c}$. The half-time was estimated at a crystallization temperature of 128 ^oC, and was seen to be significantly affected by extrusion temperature, extrusion speed, nanotube type, and nanotube concentration. A complete ANOVA performed on crystallization half-time is provided in Table 7.15 and the model is provided in Table 7.16.

Nanotube concentration had the largest contribution in determining $t_{1/2}$ and was estimated at close to 40 %. In addition, extrusion speed had a contribution of approximately 35 %, while nanotube type had a contribution of 12 %. These results were similar to those obtained for T_c and indicated that a higher concentration of nanotubes provided larger number of nucleation sites, thus accelerated the crystallization process and decreased $t_{1/2.}$ The model clearly showed a decreasing trend in $t_{1//2}$ with increasing speed or concentration. Figure 7.17 shows the effect of interaction between extrusion speed, temperature, and concentration on $t_{1//2}$.

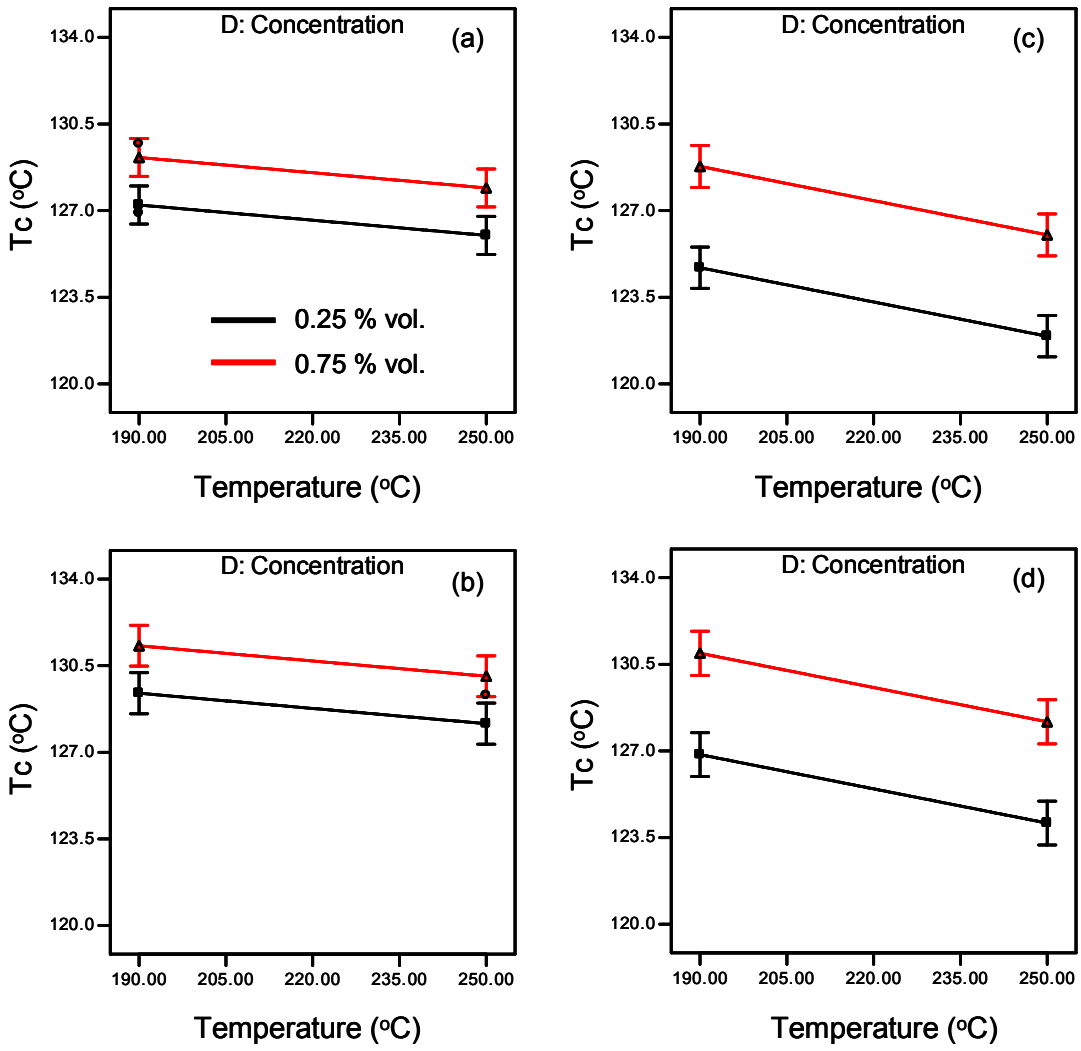

Figure 7.16. Interaction plots for crystallization temperature. PP/SWNTs at (a) 10 rpm and 135 min, and (b) 100 rpm and 135 min, and PP/C12SWNT at (c) 10 rpm and 135 min, and (d) 100 rpm and 135 min.

Source	Sum of Squares	DF	Mean Square	F Value	Prob > F
Model	2.51	5	0.50	34.92	<0.0001
Extrusion Temp (*T*)	0.19	1	0.19	12.90	0.0015
Extrusion Speed (*n*)	0.99	1	0.99	69.05	<0.0001
Concentration (*x*)	1.09	1	1.09	75.85	<0.0001
Material (*M*)	0.35	1	0.35	23.99	<0.0001
n^2	0.18	1	0.18	12.31	0.0018
Residual	0.35	24	0.014		
Cor. Total	2.86	29			

Standard Deviation	0.12	**Mean**	2.14	**R^2**	0.879	**Coefficient of Variance**	5.60

Table 7.15. Analysis of variance performed on crystallization half-time.

Crystallization Half-time at 128 ^{o}C	
SWNT	$\text{Log}_{10}(t_{1/2}) = 2.189 + 2.886\text{E-}03*T - 0.017*n - 838*x + 1.118\text{E-}04*n^2$
C12SWNT	$\text{Log}_{10}(t_{1/2}) = 2.408 + 2.886\text{E-}03*T - 0.017*n - 838*x + 1.118\text{E-}04*n^2$

Table 7.16. Design generated predictive models for crystallization half-time.

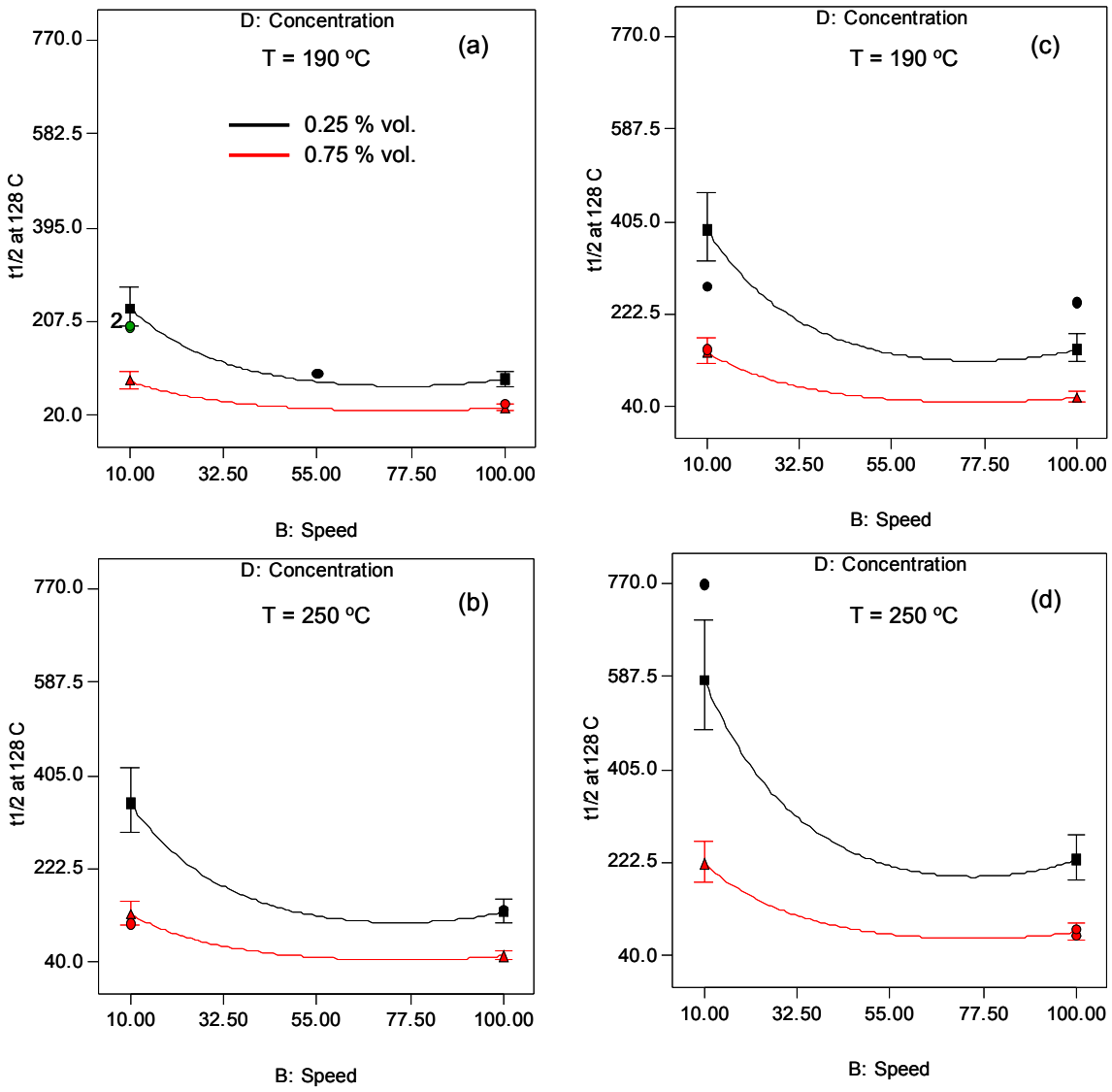

Figure 7.17. Interaction plot of crystallization half-time of (a) and (b) PP/SWNT, and (c) and (d) PP/C12SWNT.

The interaction plots showed that, at low speeds, the nanotubes were largely aggregated, thus providing very few nucleation sites, especially at lower concentrations. With increasing speed, and consequent nanotube aggregate break ups, $t_{1/2}$ gradually decreased. The values of $t_{1/2}$ also increased at high screw speeds. This was more prominent in

nanocomposites with lower concentrations of 0.25 % vol. SWNT or C12SWNT, and was attributed to polymer degradation.

Nanotube type and concentration were major factors in deciding crystallization properties, and had a very significant effect on the crystallization activation energy, $\Delta E_{a,c}$. The ANOVA for $\Delta E_{a,c}$ is given in Table 7.17 and the model is given in Table 7.18. Nanotube type had 11 % contribution towards the final $\Delta E_{a,c}$, while nanotube concentration had 44 % contribution. In addition, extrusion temperature, speed, and time all had significant effects on the activation energy.

Source	**Sum of Squares**	**DF**	**Mean Square**	**F Value**	**Prob > F**
Model	66418.25	5	13283.65	12.38	<0.0001
Extrusion Temp (*T*)	7456.74	1	7456.74	6.95	0.0145
Extrusion Speed (*n*)	6740.19	1	6740.19	6.28	0.0194
Extrusion Time (*t*)	10162.00	1	10162.00	9.47	0.0052
Concentration (*x*)	40452.14	1	40452.14	37.71	<0.0001
Material (*M*)	10280.58	1	10280.58	9.58	0.0049
Residual	25747.21	24	1072.80		
Cor. Total	92165.47	29			

Standard Deviation	32.8	**Mean**	246.53	**R^2**	0.721	**Coefficient of Variance**	13.3

Table 7.17. Analysis of variance of crystallization activation energy.

	Crystallization Activation Energy
SWNT	$\Delta E_{a,c} = 175.343 + 0.582*T - 0.369*n + 0.194*t - 161.321*x$
C12SWNT	$\Delta E_{a,c} = 213.164 + 0.582*T - 0.369*n + 0.194*t - 161.321*x$

Table 7.18. Design generated model for crystallization activation energy.

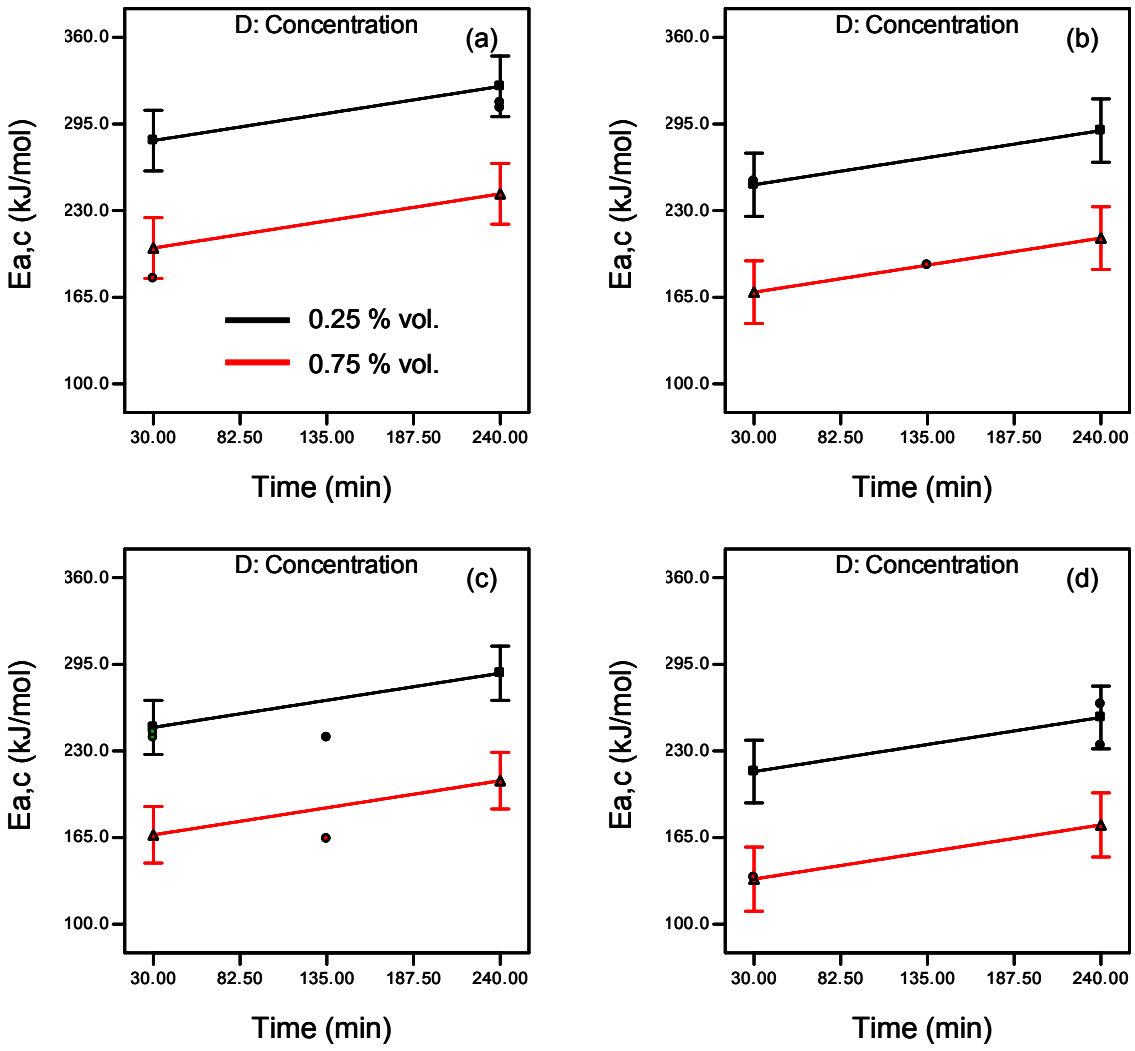

Figure 7.18. Interaction plot of crystallization activation energy for PP/SWNT.

Based on the model, increasing nanotube concentration and extrusion speed decreased $\Delta E_{a,c}$. Increasing extrusion temperature and time tended to increase $\Delta E_{a,c}$, indicating, again, that processing at high temperature and time degraded the polymer, thus requiring higher energy to crystallize. These interactions are illustrated in the interaction plots for PP/SWNT in Figure 7.18; thePP/C12SWNT interaction plots were similar. Increasing speed resulted in a noticeable decrease in the activation energy, again

attesting to the fact that higher speeds broke apart the aggregates of nanotubes coating the PP surface in rotary evaporated PP nanocomposites.

A key difference between the effect of processing conditions seen here and that seen with the HC nanocomposites in Chapter 6 was the effect of extrusion temperature and speed. While extrusion temperature and speed had significant effects on the RE nanocomposites, their effect on the HC nanocomposite crystallization was insignificant. The primary reason for this discrepancy was the higher degree of nanotube dispersion obtained in the HC nanocomposites prior to melt extrusion. The already well dispersed nanotubes in PP in HC nanocomposites provided stability from degradation at high extrusion temperatures, thus voiding the effect of extrusion temperature. In addition, due to the fact that the nanotubes were dispersed as much smaller bundles in PP prior to melt extrusion, speed also did not have a discernibly significantly effect.

7.6. Conclusions

The design of experiments approach used in this investigation narrowed down the factors that significantly influenced polymer nanocomposite responses. The initial mixing prior to melt extrusion achieved uniform distribution of nanotube bundles on the surface of PP flakes. As with the design on the hot coagulated nanocomposites in Chapter 6, this design also indicated that the optimum melt processing conditions to be employed was highly dependent on the nanocomposite property desired. Nanotube concentration was observed to be a very significant factor among all responses studied. Higher nanotube concentration improved nanocomposite properties by either forming an interconnected network, thus preventing PP chain relaxation in melts, or just by the sheer number

available as PP nucleation sites, leading to improved crystallization kinetics. In addition, higher nanotube concentration provided significantly higher stability against PP degradation. Extrusion speed played a much more significant role in melt extruded rotary evaporated nanocomposites compared to the hot coagulated nanocomposites from Chapter 6. This was attributed to the fact that the rotary evaporated nanocomposites tended to have larger aggregates of nanotubes adhered to their surface, and consequently the effect of speed, or shear, was more prominent and noticeable. Nanotube chemistry did not have a significant effect on the nanocomposite rheological behavior. This was surprising, considering the functionalized nanotubes were expected to disperse better than plain SWNTs. While crystallization temperature increased with both nanotube loading and extrusion speed, decomposition temperature was unaffected by extrusion screw speed. The effects noted were the result of complex interactions between nanotube concentration, degree of dispersion, and polymer degradation.

Chapter 8

Conclusions

The investigation reinforced the fact that the degree and uniformity of carbon nanotube dispersion in polymer is critical to imparting their nanoscale properties to bulk composite materials. Effective, scalable, techniques for achieving and measuring dispersion are required to translate the improvements theorized and observed in the laboratory to industrial scale. The investigation executed the first direct comparison of three potential dispersion techniques: dry blending, hot coagulation, and rotary evaporation (a model process similar to spray drying); each initial mixing process was followed by melt extrusion at the same conditions. The results revealed that the distribution of nanomaterials in the polymer prior to melt extrusion in the Haake Minilab is key to obtaining the best dispersion. Characterizing the nanocomposites confirmed that the best dispersion was achieved from the hot coagulation process, poorest dispersion resulted from dry blending, with rotary evaporation falling somewhere in between. In addition, the effect of melt extrusion conditions was observed to significantly vary depending on the initial nanomaterial distribution obtained. Melt processing had very limited effect on the properties of dry mixed nanocomposites. The apparently large aggregates of nanomaterials present after dry mixing were too big to be effectively broken apart and distributed through the polymer melt during melt extrusion in the Haake Minilab. The excellent nanotube dispersion obtained during initial mixing by hot coagulation rather

subdued the effects of melt extrusion on the ultimate dispersion state. The resulting stabilization of the interphase also reduced the effects of processing on polymer degradation during extrusion, particularly for SWNT composites. In other words, nanotube dispersion after initial mixing was already excellent and there was little that could be done during melt extrusion to make it better. Melt extrusion, however, had very significant effects on the properties of rotary evaporated nanocomposites due to the fact that the nanotubes, while well distributed through the polymer matrix, were still largely present as aggregates after initial mixing. The effects were observed to be a result of complex interactions between the nanomaterial concentration, degree of dispersion, polymer and filler degradation, and stability of the nanocomposite microstructure. A significant observation in the hot coagulated nanocomposites was the existence of a critical time of mixing needed to achieve a stable and steady nanocomposite microstructure. The critical time, in some cases, was as high as two hours. The results from this research indicated a definite interrelationship between the nanomaterial structure, processing conditions, and nanocomposite properties. However, there was no set processing condition that maximized all nanocomposite properties. This research clearly demonstrated that the optimum melt processing conditions to be employed varied depending on the materials being used and the property of interest.

The finding that initial mixing by rotary evaporation, together with optimized melt processing conditions, may provide a simple scalable route to polymer nanocomposite fabrication provides a foundation for future research. Since the nanotubes are largely adhered on the surface to the polymer flakes/pellets, a thorough investigation into the effect of varying the polymer flake/pellet size needs to be carried out. Smaller

polymer flake/pellet size is expected to result in better distribution of nanomaterials through the bulk matrix. Given that the Haake Minilab lacks distributive and dispersive mixing elements, further investigations need to be carried out to study the requirement of an initial mixing method during fabrication of polymer nanocomposites in industrial scale melt extruders that posses both these mixing elements.

Finally the results of this dissertation show that while the large number of runs required to use a Design of Experiments approach may be daunting it is also rewarding. This approach provides a wealth of information on interactions and non-linear responses that can not be obtained by one at a time experimentation. Therefore, while this approach has rarely been used in carbon nanomaterial research, it is a powerful tool for optimizing specific properties of nanocomposite systems.

References

(1) E Roduner: Size matters: why nanomaterials are different. Chemical Society Reviews 35 583-92.

(2) FW Eduardo Hl Falcao, Carbon allotropes: beyond graphite and diamond, 2007, p. 524-31.

(3) S Iijima: Helical microtubules of graphitic carbon. Nature 354 (1991) 56-58.

(4) A Thess, R Lee, P Nikolaev, D Hongjie, P Petit, J Robert, X Chunhui, L Young Hee, K Seong Gon, AG Rinzler, DT Colbert, GE Scuseria, D Tomanek, JE Fischer, RE Smalley: Crystalline ropes of metallic carbon nanotubes. Science v273 (1996) p483(5).

(5) X Zhang, Q Li, TG Holesinger, PN Arendt, J Huang, PD Kirven, TG Clapp, RF DePaula, X Liao, Y Zhao, L Zheng, DE Peterson, Y Zhu: Ultrastrong, Stiff, and Lightweight Carbon-Nanotube Fibers. Advanced Materials 19 (2007) 4198-201.

(6) G Natta, P Pino, P Corradini, F Danusso, E Mantica, G Mazzanti, G Moraglio: Crystalline High Polymers of αλπηα Olefins. Journal of the American Chemical Society 77 (1955) 1708-10.

(7) J Cowie: Polymers: chemistry and physics of modern materials, CRC press, 1991.

(8) C Maier, T Calafut: Polypropylene: the definitive user's guide and databook, CRC, 1998.

(9) E Klein, V Lukes, Z Cibulkova: On the energetics of phenol antioxidants activity. Petroleum and Coal 47 (2005) 33-39.

(10) MS Dresselhaus, G Dresselhaus, PC Eklund: Science of fullerenes and carbon nanotubes, Academic Press, San Diego, California, 1996.

(11) VZ Mordkovich: Carbon Nanofibers: A New Ultrahigh-Strength Material for Chemical Technology. Theoretical Foundations of Chemical Engineering 37 (2003) 429-38.

(12) GG Tibbetts, CP Beetz: Mechanical properties of vapour-grown carbon fibres. Journal of Physics D: Applied Physics 20 (1987) 292-97.

(13) T Uchida, DP Anderson, ML Minus, S Kumar: Morphology and modulus of vapor grown carbon nano fibers. Journal of Materials Science 41 (2006) 5851-56.

(14) GG Tibbetts, ML Lake, KL Strong, BP Rice: A review of the fabrication and properties of vapor-grown carbon nanofiber/polymer composites. Composites Science and Technology 67 (2007) 1709-18.

(15) K Lozano: Vapor-crown carbon-fiber composites: Processing and electrostatic dissipative applications. Jom-Journal of the Minerals Metals & Materials Society 52 (2000) A34-A36.

(16) M Reibold, P Paufler, AA Levin, W Kochmann, N Patzke, DC Meyer: Materials: Carbon nanotubes in an ancient Damascus sabre. Nature 444 (2006) 286-86.

(17) P Kim, L Shi, A Majumdar, PL McEuen: Thermal Transport Measurements of Individual Multiwalled Nanotubes. Physical Review Letters 87 (2001) 215502.

(18) J Che, T Cagin, WAG Iii: Thermal conductivity of carbon nanotubes. Nanotechnology 11 (2000) 65-69.

(19) RH Baughman, AA Zakhidov, WA de Heer: Carbon Nanotubes--the Route Toward Applications. Science 297 (2002) 787-92.
(20) A Krishnan, E Dujardin, TW Ebbesen, PN Yianilos, MMJ Treacy: Young's modulus of single-walled nanotubes. Physical Review B 58 (1998) 14013.
(21) M-F Yu, BS Files, S Arepalli, RS Ruoff: Tensile Loading of Ropes of Single Wall Carbon Nanotubes and their Mechanical Properties. Physical Review Letters 84 (2000) 5552.
(22) DA Walters, LM Ericson, MJ Casavant, J Liu, DT Colbert, KA Smith, RE Smalley: Elastic strain of freely suspended single-wall carbon nanotube ropes. Applied Physics Letters 74 (1999) 3803-05.
(23) R Saito, M Fujita: Electronic structure of chiral graphene tubules. Applied Physics Letters 60 (1992) 2204.
(24) TW Odom, J-L Huang, P Kim, CM Lieber: Atomic structure and electronic properties of single-walled carbon nanotubes. Nature 391 (1998) 62-64.
(25) JWG Wilder, LC Venema, AG Rinzler, RE Smalley, C Dekker: Electronic structure of atomically resolved carbon nanotubes. Nature 391 (1998) 59-62.
(26) AH Wazir, L Kakakhel: Preparation and characterization of pitch-based carbon fibers. New Carbon Materials 24 (2009) 83-88.
(27) N Yaman, T Oktem, N Seventekin: Properties of carbon fibers and usage possibilities. Tekstil Ve Konfeksiyon 17 (2007) 90-95.
(28) DDL Chung: Carbon fiber composites, Butterworth-Heinemann, 1994.
(29) O Breuer, U Sundararaj: Big returns from small fibers: A review of polymer/carbon nanotube composites. Polymer Composites 25 (2004) 630-45.
(30) M Endo, YA Kim, T Hayashi, K Nishimura, T Matusita, K Miyashita, MS Dresselhaus: Vapor-grown carbon fibers (VGCFs): Basic properties and their battery applications. Carbon 39 (2001) 1287-97.
(31) IC Finegan, GG Tibbetts: Electrical conductivity of vapor-grown carbon fiber/thermoplastic composites. Journal of Materials Research 16 (2001) 1668-74.
(32) GG Tibbetts, IC Finegan, C Kwag: Mechanical and electrical properties of vapor-grown carbon fiber thermoplastic composites. Molecular Crystals and Liquid Crystals 387 (2002) 353-57.
(33) KI Winey, RA Vaia: Polymer nanocomposites. Mrs Bulletin 32 (2007) 314-19.
(34) JN Coleman, U Khan, YK Gun'ko: Mechanical reinforcement of polymers using carbon nanotubes. Advanced Materials 18 (2006) 689-706.
(35) MSP Shaffer, AH Windle: Fabrication and characterization of carbon nanotube/poly(vinyl alcohol) composites. Advanced Materials 11 (1999) 937-+.
(36) XL Xie, YW Mai, XP Zhou: Dispersion and alignment of carbon nanotubes in polymer matrix: A review. Materials Science & Engineering R-Reports 49 (2005) 89-112.
(37) M-F Yu, O Lourie, MJ Dyer, K Moloni, TF Kelly, RS Ruoff: Strength and Breaking Mechanism of Multiwalled Carbon Nanotubes Under Tensile Load. Science 287 (2000) 637-40.
(38) A Peigney, C Laurent, E Flahaut, RR Bacsa, A Rousset: Specific surface area of carbon nanotubes and bundles of carbon nanotubes. Carbon 39 (2001) 507-14.
(39) MJ Green, N Behabtu, M Pasquali, WW Adams: Nanotubes as polymers. Polymer 50 (2009) 4979-97.

(40) CT White, TN Todorov: Carbon nanotubes as long ballistic conductors. Nature 393 (1998) 240-42.
(41) W Liang, M Bockrath, D Bozovic, JH Hafner, M Tinkham, H Park: Fabry - Perot interference in a nanotube electron waveguide. Nature 411 (2001) 665-69.
(42) M Ouyang, J-L Huang, CL Cheung, CM Lieber: Energy Gaps in "Metallic" Single-Walled Carbon Nanotubes. Science 292 (2001) 702-05.
(43) SG Louie, in M.S. Dresselhaus, G. Dresselhaus, P. Avouris (Eds.), Electronic Properties, Junctions, and Defects of Carbon Nanotubes. Springer-Verlag, Heidelberg, 2001, p. 113.
(44) C Journet, WK Maser, P Bernier, A Loiseau, ML de la Chapelle, S Lefrant, P Deniard, R Lee, JE Fischer: Large-scale production of single-walled carbon nanotubes by the electric-arc technique. Nature 388 (1997) 756-58.
(45) Correspondence. Carbon 37 (1999) 1865-68.
(46) H Takikawa, O Kusano, T Sakakibara: Graphite cathode spot produces carbon nanotubes in arc discharge. Journal of Physics D: Applied Physics 32 (1999) 2433-37.
(47) T Guo, P Nikolaev, AG Rinzler, D Tomanek, DT Colbert, RE Smalley: Self-Assembly of Tubular Fullerenes. Journal of Physical Chemistry 99 (1995) 10694-97.
(48) T Guo, P Nikolaev, A Thess, DT Colbert, RE Smalley: Catalytic growth of single-walled manotubes by laser vaporization. Chemical Physics Letters 243 (1995) 49-54.
(49) HM Cheng, F Li, G Su, HY Pan, LL He, X Sun, MS Dresselhaus: Large-scale and low-cost synthesis of single-walled carbon nanotubes by the catalytic pyrolysis of hydrocarbons. Applied Physics Letters 72 (1998) 3282-84.
(50) P Nikolaev, MJ Bronikowski, RK Bradley, F Rohmund, DT Colbert, KA Smith, RE Smalley: Gas-phase catalytic growth of single-walled carbon nanotubes from carbon monoxide. Chemical Physics Letters 313 (1999) 91-97.
(51) B Kitiyanan, WE Alvarez, JH Harwell, DE Resasco: Controlled production of single-wall carbon nanotubes by catalytic decomposition of CO on bimetallic Co-Mo catalysts. Chemical Physics Letters 317 (2000) 497-503.
(52) SM Bachilo, L Balzano, JE Herrera, F Pompeo, DE Resasco, RB Weisman: Narrow (n,m)-distribution of single-walled carbon nanotubes grown using a solid supported catalyst. Journal of the American Chemical Society 125 (2003) 11186-87.
(53) YQ Tan, DE Resasco: Dispersion of single-walled carbon nanotubes of narrow diameter distribution. Journal of Physical Chemistry B 109 (2005) 14454-60.
(54) JN Coleman, DF O'Brien, M in het Panhuis, AB Dalton, B McCarthy, RC Barklie, WJ Blau: Solubility and purity of nanotubes in arc discharge carbon powder. Synthetic Metals 121 (2001) 1229-30.
(55) OJBSEB Aljoscha Roch, High-yield synthesis of single-walled carbon nanotubes with a pulsed arc-discharge technique, 2007, p. 3907-10.
(56) CD Scott, S Arepalli, P Nikolaev, RE Smalley: Growth mechanisms for single-wall carbon nanotubes in a laser-ablation process. Applied Physics a-Materials Science & Processing 72 (2001) 573-80.

(57) Y-L Li, L-H Zhang, X-H Zhong, AH Windle: Synthesis of high purity single-walled carbon nanotubes from ethanol by catalytic gas flow CVD reactions. Nanotechnology 18 (2007) 225604.
(58) H Li, X Wang, Y Song, Y Liu, Q Li, L Jiang, D Zhu: Super-"Amphiphobic" Aligned Carbon Nanotube Films. Angewandte Chemie International Edition 40 (2001) 1743-46.
(59) E Lafuente, M Piñol, L Oriol, E Muñoz, AM Benito, WK Maser, AB Dalton, JL Serrano, MT Martínez: Polyazomethine/carbon nanotube composites. Materials Science and Engineering: C 26 (2006) 1198-201.
(60) A Funck, W Kaminsky: Polypropylene carbon nanotube composites by in situ polymerization. Composites Science and Technology 67 (2007) 906-15.
(61) N Hu, H Zhou, G Dang, X Rao, C Chen, W Zhang, Efficient dispersion of multi-walled carbon nanotubes by in situ polymerization, 2007, p. 655-59.
(62) H-S Kim, BH Park, J-S Yoon, H-J Jin: Nylon 610/functionalized multiwalled carbon nanotubes composites by in situ interfacial polymerization. Materials Letters 61 (2007) 2251-54.
(63) D McIntosh, VN Khabashesku, EV Barrera: Benzoyl Peroxide Initiated In Situ Functionalization, Processing, and Mechanical Properties of Single-Walled Carbon Nanotubeâˆ'Polypropylene Composite Fibers. The Journal of Physical Chemistry C 111 (2007) 1592-600.
(64) K Prashantha, J Soulestin, MF Lacrampe, P Krawczak: Present Status and Key Challenges of Carbon Nanotubes Reinforced Polyolefins: A Review on Nanocomposites Manufacturing and Performance Issues. Polymers & Polymer Composites 17 (2009) 205-45.
(65) F Liang, JM Beach, K Kobashi, AK Sadana, YI Vega-Cantu, JM Tour, WE Billups: In Situ Polymerization Initiated by Single-Walled Carbon Nanotube Salts. Chemistry of Materials 18 (2006) 4764-67.
(66) P Slobodian, A Lengalova, P Saha: Poly(methyl methacrylate)/multi-wall carbon nanotubes composites prepared by solvent cast technique: Composites electrical percolation threshold. Journal of Reinforced Plastics and Composites 26 (2007) 1705-12.
(67) U Khan, K Ryan, WJ Blau, JN Coleman: The effect of solvent choice on the mechanical properties of carbon nanotube-polymer composites. Composites Science and Technology 67 (2007) 3158-67.
(68) R Haggenmueller, JE Fischer, KI Winey: Single Wall Carbon Nanotube/Polyethylene Nanocomposites: Nucleating and Templating Polyethylene Crystallites. Macromolecules 39 (2006) 2964-71.
(69) JC Kearns, RL Shambaugh: Polypropylene fibers reinforced with carbon nanotubes. Journal of Applied Polymer Science 86 (2002) 2079-84.
(70) D Qian, EC Dickey, R Andrews, T Rantell: Load transfer and deformation mechanisms in carbon nanotube-polystyrene composites. Applied Physics Letters 76 (2000).
(71) WE Dondero, RE Gorga: Morphological and mechanical properties of carbon nanotube/polymer composites via melt compounding. Journal of Polymer Science Part B: Polymer Physics 44 (2006) 864-78.

(72) SZ Yu, YK Juay, MS Young: Fabrication and characterization of carbon nanotube reinforced poly(methyl methacrylate) nanocomposites. Journal of Nanoscience and Nanotechnology 8 (2008) 1852-57.
(73) R Abu-Zurayk, E Harkin-Jones, T McNally, G Menary, P Martin, C Armstrong: Biaxial deformation behavior and mechanical properties of a polypropylene/clay nanocomposite. Composites Science and Technology 69 (2009) 1644-52.
(74) X Jiang, LT Drzal: Multifunctional High Density Polyethylene Nanocomposites Produced by Incorporation of Exfoliated Graphite Nanoplatelets 1: Morphology and Mechanical Properties. Polymer Composites 31 1091-98.
(75) AL Moore, AT Cummings, JM Jensen, L Shi, JH Koo: Thermal Conductivity Measurements of Nylon 11-Carbon Nanofiber Nanocomposites. Journal of Heat Transfer-Transactions of the Asme 131 (2009) 5.
(76) S Kumar, H Doshi, M Srinivasarao, JO Park, DA Schiraldi: Fibers from polypropylene/nano carbon fiber composites. Polymer 43 (2002) 1701-03.
(77) Q Zhang, S Rastogi, D Chen, D Lippits, PJ Lemstra: Low percolation threshold in single-walled carbon nanotube/high density polyethylene composites prepared by melt processing technique. Carbon 44 (2006) 778-85.
(78) MAL Manchado, L Valentini, J Biagiotti, JM Kenny: Thermal and mechanical properties of single-walled carbon nanotubes-polypropylene composites prepared by melt processing. Carbon 43 (2005) 1499-505.
(79) Q-Q Ni, C-S Zhang, Y Fu, G Dai, T Kimura: Shape memory effect and mechanical properties of carbon nanotube/shape memory polymer nanocomposites. Composite Structures doi:10.1016/j.compstruct.2006.08.017 (2006).
(80) J Yang, Y Lin, J Wang, M Lai, J Li, J Liu, X Tong, H Cheng: Morphology, Thermal Stability, and Dynamic Mechanical Properties of Atactic Polypropylene/Carbon Nanotube Composites. Journal of Applied Polymer Science 98 (2005) 1087-91.
(81) TE Chang, LR Jensen, A Kisliuk, RB Pipes, R Pyrz, AP Sokolov: Microscopic mechanism of reinforcement in single-wall carbon nanotube/polypropylene nanocomposite. Polymer 46 (2005) 439-44.
(82) YY Huang, SV Ahir, EM Terentjev: Dispersion rheology of carbon nanotubes in a polymer matrix. Physical Review B 73 (2006).
(83) A Rodney, J David, M Mickael, R Terry, Fabrication of Carbon Multiwall Nanotube/Polymer Composites by Shear Mixing, 2002, p. 395-403.
(84) JW Goodwin: Colloids and Interfaces with Surfactants and Polymers, Wiley, 2004.
(85) B Derjaguin, L Landau, Acta Physicochim. URSS, 1941, p. 633-62.
(86) EJW Verwey, J Overbeek, Theory of the stability of lyophobic colloids. Elsevier, Amsterdam, 1948, p. 9.
(87) SN Song, XK Wang, RPH Chang, JB Ketterson: Electronic properties of graphite nanotubules from galvanomagnetic effects. Physical Review Letters 72 (1994) 697.
(88) HC Hamaker: The London--van der Waals attraction between spherical particles. Physica 4 (1937) 1058-72.

(89) JN Israelachvili: Intermolecular and surface forces, Academic press London, 1991.
(90) VA Parsegian: Van der Waals forces, Cambridge University Press Cambridge, UK, 2006.
(91) J Tersoff, RS Ruoff: Structural Properties of a Carbon-Nanotube Crystal. Physical Review Letters 73 (1994) 676.
(92) LA Girifalco, M Hodak, RS Lee: Carbon nanotubes, buckyballs, ropes, and a universal graphitic potential. Physical Review B 62 (2000) 13104.
(93) DW Coffin, LA Carlsson, RB Pipes: On the separation of carbon nanotubes. Composites Science and Technology 66 (2006) 1132-40.
(94) KL Lu, RM Lago, YK Chen, MLH Green, PJF Harris, SC Tsang: Mechanical damage of carbon nanotubes by ultrasound. Carbon 34 (1996) 814-16.
(95) A Lucas, C Zakri, M Maugey, M Pasquali, P van der Schoot, P Poulin: Kinetics of Nanotube and Microfiber Scission under Sonication. Journal of Physical Chemistry C 113 (2009) 20599-605.
(96) QH Cheng, S Debnath, E Gregan, HJ Byrne: Ultrasound-Assisted SWNTs Dispersion: Effects of Sonication Parameters and Solvent Properties. Journal of Physical Chemistry C 114 (2010) 8821-27.
(97) CM Hansen: Hansen solubility parameters: a user's handbook, CRC, 2007.
(98) NC Jonathan, Liquid-Phase Exfoliation of Nanotubes and Graphene, 2009, p. 3680-95.
(99) SD Bergin, Z Sun, D Rickard, PV Streich, JP Hamilton, JN Coleman: Multicomponent Solubility Parameters for Single-Walled Carbon Nanotube - Solvent Mixtures. ACS Nano 3 (2009) 2340-50.
(100) S Detriche, G Zorzini, JF Colomer, A Fonseca, JB Nagy: Application of the Hansen Solubility Parameters Theory to Carbon Nanotubes. Journal of Nanoscience and Nanotechnology 8 (2008) 6082-92.
(101) MJ O'Connell, P Boul, LM Ericson, C Huffman, Y Wang, E Haroz, C Kuper, J Tour, KD Ausman, RE Smalley: Reversible water-solubilization of single-walled carbon nanotubes by polymer wrapping. Chemical Physics Letters 342 (2001) 265-71.
(102) AA Vetcher, S Srinivasan, IA Vetcher, SM Abramov, M Kozlov, RH Baughman, SD Levene: Fractionation of SWNT/nucleic acid complexes by agarose gel electrophoresis. Nanotechnology 17 (2006) 4263-69.
(103) M Zheng, A Jagota, MS Strano, AP Santos, P Barone, SG Chou, BA Diner, MS Dresselhaus, RS McLean, GB Onoa, GG Samsonidze, ED Semke, M Usrey, DJ Walls: Structure-Based Carbon Nanotube Sorting by Sequence-Dependent DNA Assembly. Science 302 (2003) 1545-48.
(104) V Lordi, N Yao: Molecular mechanics of binding in carbon-nanotube-polymer composites. Journal of Materials Research 15 (2000) 2770-79.
(105) WTAH Zhongfang Chen, Reactivity of the Convex and Concave Surfaces of Single-Walled Carbon Nanotubes (SWCNTs) towards Addition Reactions: Dependence on the Carbon-Atom Pyramidalization, 2003, p. 93-97.
(106) J Liu, AG Rinzler, H Dai, JH Hafner, RK Bradley, PJ Boul, A Lu, T Iverson, K Shelimov, CB Huffman, F Rodriguez-Macias, Y-S Shon, TR Lee, DT Colbert, RE Smalley: Fullerene pipes. Science 280 (1998) 1253.

(107) J Chen, AM Rao, S Lyuksyutov, ME Itkis, MA Hamon, H Hu, RW Cohn, PC Eklund, DT Colbert, RE Smalley, RC Haddon: Dissolution of Full-Length Single-Walled Carbon Nanotubes. Journal of Physical Chemistry B 105 (2001) 2525-28.
(108) J Chen, MA Hamon, H Hu, Y Chen, AM Rao, PC Eklund, RC Haddon: Solution Properties of Single-Walled Carbon Nanotubes. Science 282 (1998) 95-98.
(109) KJ Ziegler, Z Gu, H Peng, EL Flor, RH Hauge, RE Smalley: Controlled Oxidative Cutting of Single-Walled Carbon Nanotubes. Journal of the American Chemical Society 127 (2005) 1541-47.
(110) GA Forrest, AJ Alexander: A Model for the Dependence of Carbon Nanotube Length on Acid Oxidation Time. Journal of Physical Chemistry C 111 (2007) 10792-98.
(111) VA Davis: Phase Behavior and Rheology of Single-Walled Carbon Nanotubes (SWNTs) in Superacids with Application to Fiber Spinning, Rice University, Houston, 2006.
(112) S Banerjee, T Hemraj-Benny, SS Wong, Covalent Surface Chemistry of Single-Walled Carbon Nanotubes, 2005, p. 17-29.
(113) F Liang, AK Sadana, A Peera, J Chattopadhyay, Z Gu, RH Hauge, WE Billups: A Convenient Route to Functionalized Carbon Nanotubes. Nano Letters 4 (2004) 1257-60.
(114) F Liang, LB Alemany, JM Beach, WE Billups: Structure Analyses of Dodecylated Single-Walled Carbon Nanotubes. Journal of the American Chemical Society 127 (2005) 13941-48.
(115) PK Rai, ANG Parra-Vasquez, J Chattopadhyay, RA Pinnick, F Liang, AK Sadana, RH Hauge, WE Billups, M Pasquali: Dispersions of functionalized single-walled carbon nanotubes in strong acids: Solubility and rheology. Journal of Nanoscience and Nanotechnology 7 (2007) 3378-85.
(116) HD Wagner, RA Vaia: Nanocomposites: issues at the interface. Materials Today 7 (2004) 38-42.
(117) AK-T Lau, D Hui: The revolutionary creation of new advanced materials--carbon nanotube composites. Composites Part B: Engineering 33 (2002) 263-77.
(118) AH Barber, SR Cohen, HD Wagner: Measurement of carbon nanotubeâ€“polymer interfacial strength. Applied Physics Letters 82 (2003) 4140.
(119) SJV Frankland, A Caglar, DW Brenner, M Griebel: Molecular Simulation of the Influence of Chemical Cross-Links on the Shear Strength of Carbon Nanotube-Polymer Interfaces. Journal of Physical Chemistry B 106 (2002) 3046-48.
(120) K Liao, S Li: Interfacial characteristics of a carbon nanotubeâ€“polystyrene composite system. Applied Physics Letters 79 (2001) 4225.
(121) G-W Lee, S Jagannathan, HG Chae, ML Minus, S Kumar: Carbon nanotube dispersion and exfoliation in polypropylene and structure and properties of the resulting composites. Polymer 49 (2008) 1831-40.
(122) YY Huang, SV Ahir, EM Terentjev: Dispersion rheology of carbon nanotubes in a polymer matrix. Physical Review B (Condensed Matter and Materials Physics) 73 (2006) 125422-9.
(123) J Shin, C Kim, KE Geckler: Single-walled carbon nanotube-polystyrene nanocomposites: dispersing nanotubes in organic media. Polymer International 58 (2009) 579-83.

(124) A Jorio, G Dresselhaus, MS Dresselhaus: Carbon nanotubes: advanced topics in the synthesis, structure, properties and applications, Springer Verlag, 2008.
(125) MS Dresselhaus, A Jorio, MA Pimenta: Resonance Raman spectroscopy in one-dimensional carbon materials. Anais da Academia Brasileira de Ciências 78 (2006) 423-39.
(126) F Du, RC Scogna, W Zhou, S Brand, JE Fischer, KI Winey: Nanotube Networks in Polymer Nanocomposites: Rheology and Electrical Conductivity. Macromolecules 37 (2004) 9048-55.
(127) SB Kharchenko, JF Douglas, J Obrzut, EA Grulke, KB Migler: Flow-induced properties of nanotube-filled polymer materials. Nat Mater 3 (2004) 564-68.
(128) A Celzard, E McRae, C Deleuze, M Dufort, G Furdin, JF Marêché: Critical concentration in percolating systems containing a high-aspect-ratio filler. Physical Review B 53 (1996) 6209.
(129) M-K Seo, S-J Park: Electrical resistivity and rheological behaviors of carbon nanotubes-filled polypropylene composites. Chemical Physics Letters 395 (2004) 44-48.
(130) T McNally, P Pötschke, P Halley, M Murphy, D Martin, SEJ Bell, GP Brennan, D Bein, P Lemoine, JP Quinn: Polyethylene multiwalled carbon nanotube composites. Polymer 46 (2005) 8222-32.
(131) D-H Xu, Z-G Wang, JF Douglas: Influence of Carbon Nanotube Aspect Ratio on Normal Stress Differences in Isotactic Polypropylene Nanocomposite Melts. Macromolecules 41 (2008) 815-25.
(132) AR Bhattacharyya, TV Sreekumar, T Liu, S Kumar, LM Ericson, RH Hauge, RE Smalley: Crystallization and orientation studies in polypropylene/single wall carbon nanotube composite. Polymer 44 (2003) 2373-77.
(133) L Valentini, J Biagiotti, MA Lopez-Manchado, S Santucci, JM Kenny: Effects of carbon nanotubes on the crystallization behavior of polypropylene. Polymer Engineering and Science 44 (2004) 303-11.
(134) M Avrami: Kinetics of Phase Change. I General Theory. The Journal of Chemical Physics 7 (1939) 1103-12.
(135) JY Kim, SI Han, DK Kim, SH Kim: Mechanical reinforcement and crystallization behavior of poly(ethylene 2,6-naphthalate) nanocomposites induced by modified carbon nanotube. Composites Part a-Applied Science and Manufacturing 40 (2009) 45-53.
(136) Q Yuan, S Awate, RDK Misra: Nonisothermal crystallization behavior of polypropylene-clay nanocomposites. European Polymer Journal 42 (2006) 1994-2003.
(137) W Leelapornpisit, MT Ton-That, F Perrin-Sarazin, KC Cole, J Denault, B Simard: Effect of carbon nanotubes on the crystallization and properties of polypropylene. Journal of Polymer Science Part B-Polymer Physics 43 (2005) 2445-53.
(138) VK Radhakrishnan, EW Davis, VA Davis: Influence of initial mixing methods on melt extruded single-walled carbon nanotube - polypropylene nanocomposites. Polymer Engineering and Science in press (2010).
(139) F Du, JE Fischer, KI Winey: Coagulation method for preparing single-walled carbon nanotube/poly(methyl methacrylate) composites and their modulus,

electrical conductivity, and thermal stability. Journal of Polymer Science Part B: Polymer Physics 41 (2003) 3333-38.
(140) R Blaine, B Hahn: Obtaining Kinetic Parameters by Modulated Thermogravimetry. Journal of Thermal Analysis and Calorimetry 54 (1998) 695-704.
(141) WE Dondero, RE Gorga: Morphological and mechanical properties of carbon nanotube/polymer composites via melt compounding. Journal of Polymer Science Part B-Polymer Physics 44 (2006) 864-78.
(142) TD Fornes, JW Baur, Y Sabba, EL Thomas: Morphology and properties of melt-spun polycarbonate fibers containing single- and multi-wall carbon nanotubes. Polymer 47 (2006) 1704-14.
(143) DB Shane, N Valeria, VS Philip, G Silvia, S Zhenyu, HW Alan, R Peter, NPP Niraj, TW Zhi-Tao, C Leslie, JB Werner, JB John, PH James, NC Jonathan: Towards Solutions of Single-Walled Carbon Nanotubes in Common Solvents. Advanced Materials 20 (2008) 1876-81.
(144) RD Booker, MJ Green, H Fan, ANG Parra-Vasquez, N Behabtu, CC Young, RH Hauge, HK Schmidt, RE Smalley, W-F Hwang, M Pasquali: High-shear treatment of single-walled carbon nanotube–superacid solutions as a pre-processing technique for the assembly of fibres and films Proceedings of the Institution of Mechanical Engineers, Part N: Journal of Nanoengineering and Nanosystems 222 (2008) 101-09.
(145) FM Du, RC Scogna, W Zhou, S Brand, JE Fischer, KI Winey: Nanotube networks in polymer nanocomposites: Rheology and electrical conductivity. Macromolecules 37 (2004) 9048-55.
(146) M Maugey, W Neri, C Zakri, A Derre, A Nnicaud, L Noe, M Chorro, P Launois, M Monthioux, P Poulin: Substantial improvement of nanotube processability by freeze-drying. Journal of Nanoscience and Nanotechnology 7 (2007) 2633-39.
(147) SH Lee, E Cho, SH Jeon, JR Youn: Rheological and electrical properties of polypropylene composites containing functionalized multi-walled carbon nanotubes and compatibilizers. Carbon 45 (2007) 2810-22.
(148) E-C Chen, T-M Wu: Isothermal crystallization kinetics and thermal behavior of poly([var epsilon]-caprolactone)/multi-walled carbon nanotube composites. Polymer Degradation and Stability 92 (2007) 1009-15.
(149) BB Marosfoi, A Szabo, G Marosi, D Tabuani, G Camino, S Pagliari: Thermal and spectroscopic characterization of polypropylene-carbon nanotube composites. Journal of Thermal Analysis and Calorimetry 86 (2006) 669-73.
(150) T Kashiwagi, E Grulke, J Hilding, R Harris, W Awad, J Douglas, Thermal Degradation and Flammability Properties of Poly(propylene)/Carbon Nanotube Composites, 2002, p. 761-65.
(151) R Duggal, M Pasquali: Dynamics of Individual Single-Walled Carbon Nanotubes in Water by Real-Time Visualization. Physical Review Letters 96 (2006) 246104-4.
(152) W Zhou, MF Islam, H Wang, DL Ho, AG Yodh, KI Winey, JE Fischer: Small angle neutron scattering from single-wall carbon nanotube suspensions: evidence for isolated rigid rods and rod networks. Chemical Physics Letters 384 (2004) 185-89.

(153) LA Pinheiro, MA Chinelatto, SV Canevarolo: The role of chain scission and chain branching in high density polyethylene during thermo-mechanical degradation. Polymer Degradation and Stability 86 (2004) 445-53.
(154) T Kashiwagi, E Grulke, J Hilding, R Harris, W Awad, J Douglas: Thermal degradation and flammability properties of poly(propylene)/carbon nanotube composites. Macromolecular Rapid Communications 23 (2002) 761-65.
(155) M Chipara, K Lozano, A Hernandez, M Chipara: TGA analysis of polypropylene-carbon nanofibers composites. Polymer Degradation and Stability 93 (2008) 871-76.
(156) YK Choi, KI Sugimoto, SM Song, M Endo: Mechanical and thermal properties of vapor-grown carbon nanofiber and polycarbonate composite sheets. Materials Letters 59 (2005) 3514-20.
(157) M Gryta, J Grzechulska-Damszel, A Markowska, K Karakulski: The influence of polypropylene degradation on the membrane wettability during membrane distillation. Journal of Membrane Science 326 (2009) 493-502.
(158) MKA Rex J. Kuriger: Extrusion conditions and properties of vapor grown carbon fiber reinforced polypropylene. Polymer Composites 22 (2001) 604-12.
(159) RG Larson: The Structure and Rheology of Complex Fluids, Oxford University Press, New York, 1999.
(160) BP Grady, F Pompeo, RL Shambaugh, DE Resasco: Nucleation of Polypropylene Crystallization by Single-Walled Carbon Nanotubes. The Journal of Physical Chemistry B 106 (2002) 5852-58.
(161) X Chen, G Hou, Y Chen, K Yang, Y Dong, H Zhou: Effect of molecular weight on crystallization, melting behavior and morphology of poly(trimethylene terephalate). Polymer Testing 26 (2007) 144-53.

Appendix – A1

Run	*T* (°C)	*n* (rpm)	*t* (min)	*M* Material	T_m (°C)	T_c (°C)	T_d (°C)
1	220	55	10	VGCF	162.57	121.17	412.81
2	250	100	10	VGCF	162.75	121.34	409.26
3	190	100	10	VGCF	163.57	123	420.74
4	250	10	240	VGCF	160.48	116.92	400.49
5	190	10	10	VGCF	165.1	119.77	421.33
6	250	10	240	VGCF	160.58	119	387.54
7	250	100	240	VGCF	159.43	116.78	378.55
8	190	10	240	VGCF	158.83	119.75	394.92
9	250	10	10	VGCF	164.52	121.88	416.06
10	190	100	240	VGCF	154.78	118.98	371.58
11	220	100	125	VGCF	158.25	120.68	397.77
12	250	10	240	C12-SWNT	165.86	125.16	422.19
13	210	10	87	C12-SWNT	165.07	126.63	406.4
14	250	100	10	C12-SWNT	165.37	126.88	426.17
15	190	55	10	C12-SWNT	166.26	125.77	384.06
16	250	100	240	C12-SWNT	163.07	124.76	401.94
17	190	100	163	C12-SWNT	164.99	125.98	403.99
18	250	10	240	C12-SWNT	165.67	125.3	412.14
19	210	70	240	C12-SWNT	164.14	125.95	401.19
20	250	10	10	C12-SWNT	165.75	126.14	414.74
21	190	10	240	C12-SWNT	166.53	125.25	406.88
22	220	78	67.5	C12-SWNT	166.61	125.21	399.96
23	250	100	240	C12-SWNT	162.13	125.0	400.32
24	190	10	240	SWNT	168.98	128.56	442.07
25	190	10	240	SWNT	168.26	128.81	440.78
26	190	10	10	SWNT	167.95	128.68	430.93
27	190	55	125	SWNT	166.9	129.81	439.39
28	230	100	240	SWNT	163.81	129.35	419.87
29	250	10	240	SWNT	165.06	129.09	431.74
30	190	100	10	SWNT	164.15	128.24	419.45
31	250	100	10	SWNT	165.57	128.27	434.69
32	190	100	240	SWNT	163.63	129.73	424.03
33	235	55	125	SWNT	166.06	129.92	437.52
34	190	100	10	SWNT	165.08	129.15	437.6
35	250	10	10	SWNT	166.21	128.75	440.3

Table A1. Design generated run sequence and responses for Chapter 6 (Hot Coagulation).

Appendix - A2

Run	*T* (C)	*n* (rpm)	*t* (min)	*x* (Vol.%)	*M*	Td (C)	Tm (C)	Tc (C)	Ea,c (kJ/mol)	t1/2 s	G′ (Pa)	η* (Pa s)	tan δ	G′ Slope
1	190	100	30	0.25	C12SWNT	435	163.40	125.60	269	246	12.14	911.0	7.43	1.05
2	190	10	240	0.25	C12SWNT	399	160.10	124.20	356	473	6.09	174.5	2.54	0.50
3	250	10	240	0.75	C12SWNT	378	154.50	122.90	332	305	5.25	63.1	0.54	0.25
4	250	100	135	0.75	SWNT	419	159.60	129.30	189	63	58.95	608.5	0.26	0.17
5	250	100	30	0.25	SWNT	411	160.90	127.00	252	143	3.08	227.0	7.26	0.63
6	220	55	135	0.50	C12SWNT	415	160.40	127.60	268	87	29.85	359.5	0.65	0.30
7	250	55	240	0.75	SWNT	396	156.00	127.60	248	58	12.30	128.5	0.30	0.19
8	220	10	240	0.75	SWNT	412	162.30	127.30	235	124	14.32	453.5	2.99	0.60
9	190	10	240	0.75	C12SWNT	422	162.60	128.00	200	145	149.50	2120.0	0.57	0.28
10	250	10	240	0.25	SWNT	397	161.40	125.30	311	270	0.68	299.0	44.10	1.36
11	190	100	240	0.25	SWNT	408	157.40	128.50	265	76	27.25	286.0	0.31	0.21
12	250	10	240	0.25	SWNT	414	161.80	125.10	307	275	1.24	376.5	30.32	1.44
13	190	55	30	0.25	SWNT	439	164.00	127.60	258	104	16.90	1165.0	6.80	0.94
14	190	10	30	0.50	SWNT	435	164.50	126.50	244	198	15.45	1450.0	9.32	1.22
15	250	100	240	0.75	C12SWNT	387	153.30	126.60	301	63	78.10	790.5	0.16	0.10
16	250	100	30	0.75	C12SWNT	424	163.50	128.30	201	80	101.85	1355.0	0.88	0.37
17	190	100	240	0.25	SWNT	410	159.50	128.70	234	87	5.55	72.2	0.83	0.38
18	250	100	240	0.25	C12SWNT	374	151.80	121.20	350	225	***	***	***	***
19	190	10	30	0.75	C12SWNT	435	163.90	126.60	233	153	55.65	1970.0	3.40	0.85
20	250	10	30	0.75	SWNT	430	164.10	127.50	179	115	11.20	1260.0	11.21	1.29

Table A2. Design generated run sequence and responses for Chapter 7 (Rotary Evaporation).

Appendix - A2 contd.

Run	*T* (C)	*n* (rpm)	*t* (min)	*x* (Vol.%)	*M*	Td (C)	Tm (C)	Tc (C)	Ea,c (kJ/mol)	t1/2 s	G′ (Pa)	η* (Pa s)	tan δ	G′ Slope
21	250	10	30	0.25	C12SWNT	406	163.20	121.10	288	768	4.69	926.5	19.75	1.50
22	250	100	30	0.75	C12SWNT	426	162.80	128.70	181	92	49.65	739.0	1.08	0.38
23	190	10	135	0.75	SWNT	430	164.90	129.70	164	61	60.95	1330.0	1.95	0.61
24	220	55	135	0.50	C12SWNT	418	162.60	127.90	198	100	7.00	311.0	4.31	0.65
25	190	10	30	0.25	C12SWNT	424	163.70	123.20	304	276	10.25	1415.0	13.76	1.38
26	190	10	135	0.25	SWNT	412	162.70	126.90	240	142	11.70	666.0	5.60	0.81
27	220	10	30	0.25	SWNT	419	164.20	124.20	247	405	5.94	1043.5	17.55	1.45
28	190	100	240	0.75	C12SWNT	429	163.00	129.40	167	47	253.50	2715.0	0.38	0.22
29	190	100	30	0.75	SWNT	445	165.50	130.10	135	43	67.15	1800.0	2.49	0.69
30	190	10	30	0.50	SWNT	429	164.60	126.40	240	197	14.25	1435.0	10.00	1.26

Table A2 contd. Design generated run sequence and responses for Chapter 7 (Rotary Evaporation).